

University of Warwick institutional repository: <http://go.warwick.ac.uk/wrap>

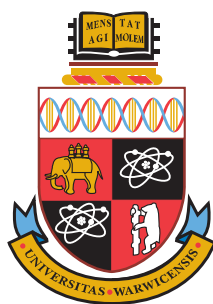
A Thesis Submitted for the Degree of PhD at the University of Warwick

<http://go.warwick.ac.uk/wrap/57456>

This thesis is made available online and is protected by original copyright.

Please scroll down to view the document itself.

Please refer to the repository record for this item for information to help you to cite it. Our policy information is available from the repository home page.



NEW APPROACHES TO THE STUDY OF BIOPHYSICOCHEMICAL PROCESSES

by

KATHERINE EMMA MEADOWS

Thesis

Submitted to the University of Warwick
for the degree of
Doctor of Philosophy

Supervisors: Prof. Patrick Unwin and Prof. Julie Macpherson

MOAC Doctoral Training Centre

May 2013



THE UNIVERSITY OF
WARWICK

CONTENTS

| | |
|---|------|
| LIST OF FIGURES | v |
| LIST OF TABLES | xiii |
| ABBREVIATIONS | xiv |
| ACKNOWLEDGEMENTS | xv |
| DECLARATION | xvi |
| ABSTRACT | xvii |
| CHAPTER 1: INTRODUCTION | 1 |
| 1.1 DETECTION OF BIOLOGICAL SPECIES | 1 |
| 1.2 DYNAMIC ELECTROCHEMISTRY | 2 |
| 1.3 ELECTRON TRANSFER PROCESSES | 2 |
| 1.4 MASS TRANSPORT | 4 |
| 1.4.1 Diffusion | 5 |
| 1.4.2 Migration | 6 |
| 1.4.3 Convection | 6 |
| 1.5 MICRO- AND NANOSCALE ELECTRODES | 7 |
| 1.5.1 Ultramicroelectrodes | 8 |
| 1.5.2 Scanning Electrochemical Microscopy | 9 |
| 1.5.3 Scanning Ion Conductance Microscopy | 12 |
| 1.5.4 Combined Techniques | 12 |
| 1.6 NON-ELECTROCHEMICAL TECHNIQUES | 13 |
| 1.6.1 Confocal Laser Scanning Microscopy | 13 |
| 1.6.2 Fluorescein | 15 |
| 1.7 BIOMEMBRANES | 16 |
| 1.7.1 Model Cell Membranes | 19 |
| 1.8 CARBON ELECTRODES | 20 |
| 1.8.1 Graphitic Carbon Electrodes | 20 |
| 1.8.2 Boron Doped Diamond | 21 |
| 1.8.3 Carbon Nanotubes | 24 |

| | | |
|--|--|-----------|
| 1.8.4 | Graphene | 28 |
| 1.9 | MODELLING | 31 |
| 1.10 | AIMS OF THIS THESIS | 34 |
| 1.11 | REFERENCES | 37 |
| CHAPTER 2: EXPERIMENTAL METHODS | | 52 |
| 2.1 | CHEMICALS | 52 |
| 2.2 | ELECTRODE MATERIALS | 54 |
| 2.2.1 | CNT Growth | 54 |
| 2.2.2 | Polycrystalline Boron Doped Diamond | 56 |
| 2.2.3 | Pt Ultramicroelectrode Characterisation | 57 |
| 2.3 | ELECTROCHEMICAL MEASUREMENTS | 58 |
| 2.4 | CHARACTERISATION TECHNIQUES | 59 |
| 2.4.1 | Atomic Force Microscopy | 59 |
| 2.4.2 | Raman Spectroscopy | 59 |
| 2.4.3 | Pressure/Area Isotherms | 59 |
| 2.5 | MICROSCOPY TECHNIQUES | 60 |
| 2.5.1 | Scanning Electrochemical Cell Microscopy (SECCM) | 60 |
| 2.5.2 | IC-SECM Measurements | 63 |
| 2.5.3 | Confocal Laser Scanning Microscopy | 63 |
| 2.6 | SURFACE MODIFICATION WITH ULTRATHIN FILMS | 64 |
| 2.7 | SIMULATION DETAILS AND ANALYSIS | 65 |
| 2.7.1 | Simulation Details | 65 |
| 2.7.2 | Building the Model | 65 |
| 2.7.3 | Data Analysis | 66 |
| 2.8 | REFERENCES | 70 |
| CHAPTER 3: TRACE VOLTAMMETRIC DETECTION OF SEROTONIN AT CARBON ELECTRODES | | 71 |
| 3.1 | INTRODUCTION | 71 |
| 3.2 | CHARACTERISATION OF CNTs | 74 |
| 3.3 | CYCLIC VOLTAMMETRY MEASUREMENTS | 76 |
| 3.3.1 | Background currents | 77 |
| 3.3.2 | CV responses for serotonin oxidation and limits of detection | 78 |

| | | |
|--|---|------------|
| 3.4 | ASSESSMENT OF ELECTRODE FOULING EFFECTS | 82 |
| 3.5 | CONCLUSIONS | 87 |
| 3.6 | REFERENCES | 89 |
| CHAPTER 4: SCANNING ELECTROCHEMICAL CELL MICROSCOPY OF SINGLE WALLED CARBON NANOTUBES: QUANTITATIVE ANALYSIS OF HETEROGENEOUS ELECTRON TRANSFER RATES | | 92 |
| 4.1 | INTRODUCTION | 93 |
| 4.2 | THEORY AND SIMULATIONS | 95 |
| 4.3 | SWNT GROWTH AND CHARACTERISATION | 99 |
| 4.3.1 | Silver Deposition Procedure | 99 |
| 4.3.2 | AFM Analysis | 101 |
| 4.3.3 | Electrical Characterisation | 101 |
| 4.4 | DETERMINATION OF FORMAL POTENTIALS | 104 |
| 4.5 | REDOX ACTIVITY OF SWNTs FOR THE OXIDATION OF FcTMA ⁺ . . | 104 |
| 4.6 | QUANTITATIVE ANALYSIS OF HET KINETICS | 110 |
| 4.7 | ELECTROCHEMICAL RESPONSE OF SWNTs TO COMPLEX REDOX MEDIATORS | 113 |
| 4.8 | CONCLUSIONS | 114 |
| 4.9 | REFERENCES | 116 |
| CHAPTER 5: INVESTIGATION OF HETEROGENEOUS ELECTRON TRANSFER KINETICS AT POLYCRYSTALLINE BORON DOPED DIAMOND ELECTRODES USING FINITE ELEMENT METHOD SIMULATIONS | | 120 |
| 5.1 | INTRODUCTION | 120 |
| 5.2 | THEORY AND SIMULATIONS | 122 |
| 5.3 | ANALYSIS OF THE ELECTROACTIVITY OF pBDD WITH DIFFERENT REDOX MEDIATORS | 128 |
| 5.3.1 | Characterisation of the pBDD Sample | 128 |
| 5.3.2 | IC-SECM Imaging | 130 |
| 5.3.3 | Kinetic Analysis | 131 |
| 5.4 | DETERMINATION OF THE LOCAL DENSITY OF STATES | 134 |
| 5.5 | CONCLUSIONS | 136 |
| 5.6 | REFERENCES | 138 |

| | |
|---|------------|
| CHAPTER 6: A NEW APPROACH FOR THE FABRICATION OF MICROSCALE LIPID BILAYERS AT GLASS PIPETTES: APPLICATIONS FOR PASSIVE PERMEATION VISUALISATION | 140 |
| 6.1 INTRODUCTION | 141 |
| 6.2 PRINCIPLES | 144 |
| 6.3 THEORY AND SIMULATIONS | 147 |
| 6.4 BILAYER CHARACTERISATION | 152 |
| 6.5 VISUALISATION OF WEAK ACID TRANSPORT | 154 |
| 6.6 QUANTITATIVE DETERMINATION OF PERMEATION COEFFICIENTS . . . | 156 |
| 6.7 EFFECTS OF POTENTIAL FIELD ON PERMEABILITY | 162 |
| 6.8 CONCLUSIONS | 163 |
| 6.9 REFERENCES | 165 |
| CHAPTER 7: INVESTIGATION OF THE LATERAL DIFFUSION OF PROTONS AT SURFACES USING CONFOCAL LASER SCANNING MICROSCOPY COUPLED WITH SECM AND FEM SIMULATIONS | 169 |
| 7.1 INTRODUCTION | 170 |
| 7.2 SECM-CLSM PRINCIPLES | 174 |
| 7.3 THEORY AND SIMULATIONS | 176 |
| 7.4 VISUALISATION OF PROTON INTERACTION WITH MODIFIED SUBSTRATES | 181 |
| 7.4.1 Case 1: Poly-L-lysine | 181 |
| 7.4.2 Case 2: Poly-L-glutamic Acid | 186 |
| 7.4.3 Case 3: Phosphatidylcholine Bilayer | 186 |
| 7.5 OPTIMISATION OF EXPERIMENTAL SETUP AND SIMULATION METHODS | 189 |
| 7.6 CONCLUSIONS | 191 |
| 7.7 REFERENCES | 193 |
| CHAPTER 8: CONCLUSIONS | 196 |
| APPENDIX | 200 |

LIST OF FIGURES

| | | |
|------------|---|----|
| FIGURE 1.1 | <i>Schematic for a general electrode reaction.</i> | 3 |
| FIGURE 1.2 | <i>(a) Planar diffusion of a species to a macroelectrode and (b) hemispherical diffusion exhibited at a microelectrode.</i> | 8 |
| FIGURE 1.3 | <i>Schematic of a typical SECM setup.</i> | 11 |
| FIGURE 1.4 | <i>Schematic of the principles of the confocal laser scanning microscope.</i> | 14 |
| FIGURE 1.5 | <i>Illustration of how a series of 2D images at different focal depths can be reconstructed to produce a 3D image</i> | 15 |
| FIGURE 1.6 | <i>The chemical structure of fluorescein with the three available protonation sites labelled.</i> | 16 |
| FIGURE 1.7 | <i>Structure of (a) a typical phospholipid molecule and (b) a phospholipid bilayer.</i> | 17 |
| FIGURE 1.8 | <i>FE-SEM image of polycrystalline BDD.</i> | 23 |
| FIGURE 1.9 | <i>Different morphologies of cCVD-grown SWNTs: (a) aligned SWNTs, (b) 2D networks, (c) 3D forests.</i> | 25 |
| FIGURE 2.1 | <i>CVD system for the growth of 2D CNT networks.</i> | 55 |
| FIGURE 2.2 | <i>(a) CVD system for the growth of flow aligned SWNTs. (b) Interior of the CVD reactor showing the alignment of the substrate.</i> | 57 |
| FIGURE 2.3 | <i>(a) SECCM setup for a typical experiment. (b) Illustration of the meniscus of the SECCM tip scanning over SWNTs.</i> | 62 |
| FIGURE 2.4 | <i>(a) Example geometry and mesh, and (b) normalised concentration profile for the simulation of a UME near a substrate.</i> | 68 |
| FIGURE 2.5 | <i>Example working curve relating k^0 to tip current.</i> | 69 |
| FIGURE 3.1 | <i>(a) AFM image, $2\ \mu\text{m} \times 2\ \mu\text{m}$, of a CNTN on quartz. (b) Micro-Raman spectrum of a CNT sample.</i> | 75 |

| | | |
|------------|---|----|
| FIGURE 3.2 | <i>Schematic diagram of the CNTN electrode setup for electrochemical measurements.</i> | 76 |
| FIGURE 3.3 | <i>CVs recorded at 100 mV s^{-1} in 0.1 M NaCl and 5 mM HEPES buffer showing the background response for the GC (dotted line), pBDD (dashed line), and CNTN (solid line) electrode.</i> | 77 |
| FIGURE 3.4 | <i>CVs recorded at 100 mV s^{-1} in 0.1 M NaCl and 5 mM HEPES buffer at (a) GC and 1 mM serotonin; (b) pBDD and $100 \text{ }\mu\text{M}$ serotonin and (c) CNTN and $10 \text{ }\mu\text{M}$ serotonin.</i> | 80 |
| FIGURE 3.5 | <i>(i) CVs of background current (dashed line) and serotonin oxidation (solid line) at GC, pBDD and CNTN electrodes at concentrations close to the detection sensitivity of the electrode; in particular (a) GC electrode ($10 \text{ }\mu\text{M}$); (b) pBDD ($1 \text{ }\mu\text{M}$); (c) CNTN (50 nM). (ii) Calibration plot for the three different electrodes showing the logarithm of the background corrected oxidation peak current versus logarithm of serotonin concentration. All the CVs were carried out at 100 mV s^{-1} and in 0.1 M NaCl and 5 mM HEPES buffer.</i> | 81 |
| FIGURE 3.6 | <i>Ten repetitive CVs carried out at the (ai) pBDD electrode and (bi) CNTN electrode, at 100 mV s^{-1} and in 0.1 M NaCl and 5 mM HEPES buffer for a serotonin concentration of $10 \text{ }\mu\text{M}$. The first scan is indicated by the red dashed line. The degree of fouling with subsequent scans is indicated by recording the background corrected peak current for serotonin oxidation as a function of CV scan number, as shown below in (aii) for pBDD and (bii) for CNTN.</i> | 83 |
| FIGURE 3.7 | <i>Repetitive CVs recorded at 100 mV s^{-1} in 0.1 M NaCl and 5 mM HEPES buffer for $10 \text{ }\mu\text{M}$ serotonin electrolysis at (a) a pBDD electrode and (c) a CNTN electrode using an extended cathodic window. The red dashed line indicates the first scan. (b) CV data from (a) plotted only in the anodic potential region to highlight minimised fouling of the electrode surface.</i> | 85 |
| FIGURE 4.1 | <i>3D FEM simulation domain showing the position and orientation of the SWNT with respect to the pipette.</i> | 96 |

| | | |
|-------------|--|-----|
| FIGURE 4.2 | <i>Working planes of AC and DC currents vs meniscus height and effective bias.</i> | 97 |
| FIGURE 4.3 | <i>(a) FEM simulation of the potential field due to the application of a bias between the two QRCEs. (b) Typical simulated concentration profile of FcTMA⁺ as it is consumed at the SWNT ($k^0 = 1 \text{ cm s}^{-1}$, $E = 0.5 \text{ V}$).</i> | 100 |
| FIGURE 4.4 | <i>(a) Schematic illustrating the Ag deposition procedure for marking SWNTs to allow visualisation under the optical microscope. (b) Optical microscopy image of Ag deposits on flow-aligned SWNTs.</i> | 101 |
| FIGURE 4.5 | <i>(a) Typical AFM image of an individual aligned SWNT. (b) Histogram of heights of three separate SWNTs.</i> | 102 |
| FIGURE 4.6 | <i>Typical current-voltage curve recorded on a metallic SWNT using a mercury hemisphere electrode.</i> | 103 |
| FIGURE 4.7 | <i>Cyclic voltammograms recorded on freshly cleaved HOPG at 100 mV s^{-1} with 0.5 V bias applied between the QRCEs for (a) the oxidation of 2 mM FcTMA^+ with 50 mM NaCl in PBS with a $2 \text{ }\mu\text{m}$ pipette and (b) the oxidation of 5 mM serotonin with 100 mM NaCl and 10 mM HEPES with a 400 nm pipette.</i> | 105 |
| FIGURE 4.8 | <i>Typical cyclic voltammogram recorded at an individual SWNT for the oxidation of 0.5 mM FcTMA^+ with 50 mM NaCl in PBS at 100 mV s^{-1}.</i> | 105 |
| FIGURE 4.9 | <i>(a) SECCM map for the oxidation of 0.5 mM FcTMA^+ at the SWNT surface ($\eta = 0.2 \text{ V}$) in the forward scan direction with corresponding trace and retrace line profiles for the region indicated. (b) Conductance current recorded between the two QRCEs in the forward scan direction. (c) AC component of the conductance current recorded between the two QRCEs in the forward scan direction.</i> | 106 |
| FIGURE 4.10 | <i>(a) SECCM map for the oxidation of 0.5 mM FcTMA^+ at the SWNT surface ($\eta = 0.05 \text{ V}$) in the forward direction with corresponding trace and retrace line scans for the region indicated. (b) Histogram of peak currents from each line of the trace and retrace SECCM images.</i> | 109 |

| | | |
|-------------|--|-----|
| FIGURE 4.11 | (a) Working curve of electrochemical current vs standard rate constant, k^0 , for the oxidation of FcTMA^+ with $\eta = 0.05$ V. (b) Histogram of k^0 values for an individual SWNT with $\eta = 0.05$ V. | 111 |
| FIGURE 4.12 | Comparison of experimental and simulated ($k^0 = 1.8 \text{ cm s}^{-1}$, $\eta = 0.2$ V) data for the electrochemical currents as the SECCM pipette is scanned laterally across the SWNT. . . . | 112 |
| FIGURE 4.13 | SECCM maps for the oxidation of (a) 2 mM and (b) 5 μM serotonin at the SWNT surface ($E = 0.55$ V) in the forward direction with corresponding trace and retrace line scans for the region indicated. | 114 |
| FIGURE 5.1 | 2D simulation domain (height, h , is 200 μm) for the SG-TC set-up (not to scale); d between the Pt UME and pBDD is typically 1.0 μm | 125 |
| FIGURE 5.2 | Example simulated steady-state diffusion-limited concentration profile of $\text{Ru}(\text{NH}_3)_6^{3+}$ (present in bulk solution at a bulk concentration of 5 mM) in the SG-TC mode with an overpotential, $\eta = -0.004$ V and $k^0 = 0.1 \text{ cm s}^{-1}$ at the pBDD surface. | 126 |
| FIGURE 5.3 | Contour plots (and concentration profiles) showing the flux to the tip electrode ($a = 1.0 \mu\text{m}$) from the substrate, $d = 1.0 \mu\text{m}$, at 5% intervals for k^0 values of (a) 0.1 cm s^{-1} and (b) 0.01 cm s^{-1} (for the case of $\text{Ru}(\text{NH}_3)_6^{3+}$ with $\eta = -0.004$ V). | 127 |
| FIGURE 5.4 | Plots of simulated Pt UME tip limiting current magnitude versus $\log(k^0)$ for: (a) collection of $\text{Ru}(\text{NH}_3)_6^{2+}$ (by oxidation), electrogenerated at the surface of the pBDD ($\eta = -0.004$ V); (b) collection of FcTMA^{2+} (by reduction) electrogenerated at the surface of the pBDD ($\eta = 0.045$ V). | 128 |

| | | |
|------------|---|-----|
| FIGURE 5.5 | of a $70\text{ }\mu\text{m} \times 70\text{ }\mu\text{m}$ region of pBDD obtained with (a) FE-SEM at 2 kV with an in-lens detector, (b) Raman microscopy, with each pixel displaying the integrated area beneath the peak centred at $\sim 1332\text{ cm}^{-1}$ as a function of laser spot position, (c) IC-SECM SG-TC mapping for the collection of $\text{Ru}(\text{NH}_3)_6^{2+}$, electrogenerated at the pBDD surface ($\eta = -0.004\text{ V}$). (d) shows the k^0 values determined from the tip currents in (c) with FEM simulations. | 129 |
| FIGURE 5.6 | Schematic of IC-SECM setup in substrate generation tip collection mode. | 131 |
| FIGURE 5.7 | Images of a $70\text{ }\mu\text{m} \times 70\text{ }\mu\text{m}$ region of pBDD obtained with (a) FE-SEM at 2 kV with an in-lens detector, (b) Raman microscopy, with each pixel displaying the integrated area beneath the peak centred at $\sim 1332\text{ cm}^{-1}$ as a function of laser spot position, (c) IC-SECM SG-TC mapping for the collection of FcTMA^{2+} , electrogenerated at the pBDD surface ($\eta = 0.045\text{ V}$). (d) shows the k^0 values determined from the tip currents in (c) with FEM simulations. | 132 |
| FIGURE 5.8 | IC-SECM HET images with values above the assigned threshold of k^0 identified as black dots for (a) the oxidation of FcTMA^+ and (b) the reduction of $\text{Ru}(\text{NH}_3)_6^{3+}$ | 133 |
| FIGURE 5.9 | Band structure for p-type semiconducting BDD, where E_{VB} is the valence band potential, E_{CB} is the conduction band potential and E_{A} is the acceptor band, arising due to boron doping. | 134 |
| FIGURE 6.1 | Schematic illustration of the bilayer formation process. . . . | 145 |
| FIGURE 6.2 | Pressure/area isotherm for the compression of a DPPC monolayer. | 146 |
| FIGURE 6.3 | (a) Simulation domain for permeation coefficient determination. (b) Series of simulated fluorescence profiles at different P values for the permeation of 100 mM propanoic acid. | 149 |

| | | |
|-------------|---|-----|
| FIGURE 6.4 | (a) Fluorescence intensity-distance plot normal to the end of the pipette extending into the bulk solution. The CLSM fluorescence profile and polynomial fit is shown for 100 mM propanoic acid. (b) Experimental (left) and simulated (right) pH profile for the permeation of 100 mM propanoic acid across the bilayer located at the end of the pipette. . . . | 152 |
| FIGURE 6.5 | (a) Schematic illustration of the experimental setup for CLSM measurements. (b) Typical i - V curves for a 8 μm diameter pipette before and after bilayer formation. | 153 |
| FIGURE 6.6 | CLSM fluorescence intensity images showing the permeation of (a) 10 mM butanoic acid and (b) 10 mM hexanoic acid across a bilayer formed on 8 μm tip diameter pipettes. . . . | 155 |
| FIGURE 6.7 | (a) CLSM image of a pipette containing only 0.1 M KCl at pH 4.2 after bilayer formation. (b) Fluorescence intensity profiles for the same pipette (black line) in comparison to that for 100 mM acetic acid at pH 4.2 (red line). | 157 |
| FIGURE 6.8 | Experimental and corresponding simulated fluorescence-distance plot for (a) 100 mM acetic acid, (b) 100 mM propanoic acid, (c) 10 mM butanoic acid and (d) 10 mM hexanoic acid. | 158 |
| FIGURE 6.9 | Plot of the permeation coefficient (P) of each weak acid across DPPC and soy PC bilayers vs. (a) acyl tail length and (b) water/octanol partition coefficient (K). | 159 |
| FIGURE 6.10 | CLSM fluorescence intensity images showing the permeation of 5 mM hexanoic acid at potentials of (a) 0 V, (b) 0.5 V and (c) 1 V vs. Ag/AgCl. | 162 |
| FIGURE 6.11 | CLSM fluorescence intensity images showing the permeation of 50 mM propanoic acid at potentials of (a) 0.1 V, (b) 0.5 V and (c) 1 V vs. Ag/AgCl. | 163 |
| FIGURE 7.1 | Illustration of the Grotthuss mechanism of proton transport through aqueous solution. | 172 |
| FIGURE 7.2 | Schematic of the experimental setup for CLSM studies of proton adsorption/diffusion (not to scale). | 176 |

| | | |
|-------------|---|-----|
| FIGURE 7.3 | <i>Calibration curve showing the change in normalised fluorescence intensity with pH.</i> | 177 |
| FIGURE 7.4 | <i>Simulated spatio-temporal plots of the half-maximum fluorescence intensity for an inert surface, with and without the inclusion of the water equilibrium.</i> | 178 |
| FIGURE 7.5 | <i>Chemical structure of (a) PLL and (b) PGA.</i> | 182 |
| FIGURE 7.6 | <i>Simulated pH profiles 3 s after initiation of a 1.5 nA anodic current for an inert substrate with (a) no proton adsorption at the UME glass surface and (b) an adsorption boundary condition applied ($pK_a = 8.3$, $N = 1 \times 10^{-9} \text{ mol cm}^{-2}$). . .</i> | 183 |
| FIGURE 7.7 | <i>Experimental and simulated spatio-temporal plots of the radial position of the half-maximum fluorescence intensity for different effective pK_a values on the UME glass surface ($N = 1 \times 10^{-9} \text{ mol cm}^{-2}$).</i> | 183 |
| FIGURE 7.8 | <i>Simulated pH profile 5 ms after the initiation of the 1.5 nA anodic current ($pK_a = 8.3$ on UME glass, $N = 1 \times 10^{-9} \text{ mol cm}^{-2}$).</i> | 184 |
| FIGURE 7.9 | <i>Experimental and simulated spatio-temporal plots for PLL-modified substrates at a range of different applied anodic currents ($pK_a = 8.3$ on UME glass, $N = 1 \times 10^{-9} \text{ mol cm}^{-2}$).</i> | 185 |
| FIGURE 7.10 | <i>Experimental and simulated spatio-temporal plots for PGA-modified substrates at a range of different applied anodic currents with substrate $pK_a = 7.3$ and $N = 5 \times 10^{-10} \text{ mol cm}^{-2}$.</i> | 187 |
| FIGURE 7.11 | <i>Simulated spatio-temporal plots for supported egg PC bilayers with a range of lateral diffusion coefficients (D_{surf}). The number of adsorption sites was set as $N = 2.5 \times 10^{-10} \text{ mol cm}^{-2}$ with the adsorption rate $k_a = 1 \text{ cm s}^{-1}$.</i> | 188 |
| FIGURE 7.12 | <i>Experimental and simulated spatio-temporal plots for supported egg PC bilayers at a range of different applied anodic currents ($D_{\text{surf}} = 5 \times 10^{-5} \text{ cm}^2 \text{ s}^{-1}$, $N = 2.5 \times 10^{-10} \text{ mol cm}^{-2}$ and $k_a = 1 \text{ cm s}^{-1}$).</i> | 189 |

| | | |
|-------------|--|-----|
| FIGURE 7.13 | <i>Plot of the time offset applied to the simulated data for each anodic current applied and substrate investigated.</i> | 190 |
| FIGURE 7.14 | <i>Simulated spatio-temporal plots for each substrate studied with an applied anodic current of 1.5 nA. For all cases, the UME glass pK_a was 8.3, with $N = 1 \times 10^{-9}$ mol cm^{-2}. For the PGA substrate, $pK_a = 7.3$ with $N = 5 \times 10^{-10}$ mol cm^{-2}, and for the egg PC bilayer, $D_{surf} = 5 \times 10^{-5}$ $cm^2 s^{-1}$ with $N = 2.5 \times 10^{-10}$ mol cm^{-2} and the adsorption constant, $k_a = 1$ $cm s^{-1}$.</i> | 191 |

LIST OF TABLES

| | | |
|-----------|--|-----|
| TABLE 2.1 | <i>List of chemicals used in this thesis.</i> | 53 |
| TABLE 2.2 | <i>Description of some of the common boundary conditions implemented in COMSOL.</i> | 67 |
| TABLE 4.1 | <i>Summary of the boundary conditions used for the simulation of the electrochemical current at the SWNT surface during SECCM imaging.</i> | 98 |
| TABLE 5.1 | <i>Summary of the boundary conditions used for the simulation of the Pt UME tip current in SG-TC mode.</i> | 124 |
| TABLE 6.1 | <i>Diffusion coefficient, D_{HX}, and pK_{a} values for each weak acid studied.</i> | 149 |
| TABLE 6.2 | <i>Summary of the boundary conditions used for the simulation of the permeation of a weak acid across a bilayer.</i> | 150 |
| TABLE 6.3 | <i>Permeation coefficients (P) from previous weak acid permeation studies (units $10^{-2} \text{ cm s}^{-1}$).</i> | 159 |

ABBREVIATIONS

| | |
|---------|--|
| AFM | atomic force microscopy |
| BLM | black lipid membrane |
| BDD | boron doped diamond |
| CLSM | confocal laser scanning microscopy |
| CNT | carbon nanotube |
| cCVD | catalytic chemical vapour deposition |
| CV | cyclic voltammetry |
| CVD | chemical vapour deposition |
| EM | electron microscopy |
| FDM | finite difference method |
| FE-SEM | field emission scanning electron microscopy |
| FEM | finite element method |
| FET | field effect transistor |
| FPGA | field programmable gate array |
| GC | glassy carbon |
| GNR | graphene nanoribbon |
| GO | graphite oxide |
| HET | heterogeneous electron transfer |
| HOPG | highly oriented pyrolytic graphite |
| IC-SECM | intermittent contact scanning electrochemical microscopy |
| LDOS | local density of states |
| MWNT | multi-walled carbon nanotubes |
| pBDD | polycrystalline boron doped diamond |
| QRCE | quasi-reference counter electrode |
| SECCM | scanning electrochemical cell microscopy |
| SECM | scanning electrochemical microscopy |
| SG-TC | substrate generation tip collection |
| SICM | scanning ion conductance microscopy |
| STM | scanning tunnelling microscopy |
| SWNT | single-walled carbon nanotube |
| UME | ultramicroelectrode |
| USL | unstirred layer |

ACKNOWLEDGEMENTS

First and foremost I would like to thank Prof. Pat Unwin and Prof. Julie Macpherson for the opportunity to work within the fantastic Electrochemistry and Interfaces group. Your constant enthusiasm and passion has been inspiring, and has helped me overcome the challenges along the way to make this project a success.

I am also extremely grateful to all of the members of the group I have collaborated with over the course of this project, in particular Dr Aleix Güell, whose expertise and guidance have helped me enormously. Thank you also, to the many other group members who have given up their time training and advising me. Your knowledge and patience have been invaluable in my transformation from mathematician to electrochemist, and I have made some fantastic friends along the way. A special thanks to Dr Hollie Patten, for being a great friend and for all your advice, both scientific and otherwise. I would also like to thank Prof. Alison Rodger and everyone at the MOAC DTC for your support behind the scenes, and to the rest of my cohort for helping me make it this far.

Finally, a huge thank you to Phil and my family. Phil, thank you for always being there for me, and for always being able to put a smile on my face. A special thanks to my mum and dad for your constant love and support. I am so grateful for everything you have done for me and without you I wouldn't be where I am today.

DECLARATION

The work contained within this thesis is my own except where acknowledged. The AFM and Raman characterisation of CNT samples in Chapters 3 and 4 was carried out by Dr Aleix Güell, who also prepared many of the SWNT samples for the work in Chapter 4. The IC-SECM imaging, FE-SEM imaging, Raman spectroscopy and capacitance measurements in Chapter 5 were performed by Dr Hollie Patten with the help of Dr Laura Hutton and James Iacobini. The threshold maps in this chapter were produced by Kim McKelvey. The CLSM experiments in Chapter 7 were carried out by Binoy Paulose Nadappuram and Tahani Bawazeer.

I can confirm that this thesis has not been submitted for any degree at another university.

Parts of this thesis have been published as detailed below:

H. V. Patten, K. E. Meadows, L. A. Hutton, J. G. Iacobini, D. Battistel, K. McKelvey, A. W. Colburn, M. E. Newton, J. V. Macpherson, and P. R. Unwin, *Electrochemical Mapping Reveals Direct Correlation between Heterogeneous Electron-Transfer Kinetics and Local Density of States in Diamond Electrodes*, *Angew. Chem. Int. Ed.*, **2012**, 51 (28), 7002-7006.

A. G. Güell, K. E. Meadows, P. R. Unwin, and J. V. Macpherson, *Trace voltammetric detection of serotonin at carbon electrodes: comparison of glassy carbon, boron doped diamond and carbon nanotube network electrodes*, *Phys. Chem. Chem. Phys.*, **2010**, 12, 10108-10114.

K. E. Meadows and P. R. Unwin, *A New Approach for the Fabrication of Microscale Lipid Bilayers at Glass Pipettes: Applications for Passive Permeation Visualization*, in preparation

K. E. Meadows, A. G. Güell, P. V. Dudin, N. Ebejer, J. V. Macpherson and P. R. Unwin, *Scanning Electrochemical Cell Microscopy of Single Walled Carbon Nanotubes: Quantitative Analysis of Heterogeneous Electron Transfer Rates*, in preparation

ABSTRACT

This thesis is concerned with the study of biophysicochemical processes using electrochemistry and related techniques. The first part of the thesis discusses the electrochemical detection of biological species, and characterisation of the electrode materials employed. A comparison of two novel forms of carbon electrode, namely carbon nanotubes and polycrystalline boron doped diamond (pBDD), with more conventional carbon electrode materials reveals their enhanced characteristics for bioelectrochemistry, with improved sensitivity and resistance to fouling. These materials are further characterised using novel high-resolution electrochemical imaging methods, to determine heterogeneous electron transfer rates for a number of different redox species. The kinetic rate constants are determined from measured electrochemical currents using finite element method (FEM) modelling, which proves to be a powerful technique for the quantitative analysis of intrinsic system parameters that cannot be studied directly. The electrochemical response of isolated regions of pristine SWNTs is investigated using scanning electrochemical cell microscopy, demonstrating high electrochemical activity at the nanotube sidewalls. A similar analysis of the different facets of pBDD is performed using intermittent contact scanning electrochemical microscopy coupled with FEM simulations, revealing that the electroactivity is strongly influenced by the local density of states of the material. New techniques are also presented for the investigation of transport processes at membrane interfaces. A new method of bilayer formation is developed, which overcomes many of the limitations of current techniques, and is used to investigate the permeation rates of a series of aliphatic carboxylic acids. Using confocal laser scanning microscopy (CLSM) with a pH-sensitive fluorophore, the pH change as a weak acid permeates across the bilayer can be visualised, and the permeation coefficient determined by comparison with FEM simulations. This reveals a trend of increasing permeability with lipophilicity. Finally, CLSM is used to study the lateral diffusion of protons at lipid bilayers and other surfaces. Protons are generated galvanostatically by a UME positioned close to the substrate, altering the local pH which can be visualised by means of a pH-sensitive fluorophore. The fluorescence profile is again compared to FEM simulations, allowing the lateral diffusion coefficient to be determined.

CHAPTER 1

INTRODUCTION

The aim of this thesis is the investigation of key biophysicochemical processes via the use of experimental procedures coupled with simulation methods. This chapter gives an overview of the motivation behind the study of the biophysical systems presented herein, some of the present electrochemical and related techniques used to investigate these processes, the type of electrode materials used along with their benefits and limitations, and the simulation methods used to extract quantitative data from the experimental data.

1.1 DETECTION OF BIOLOGICAL SPECIES

There is a huge range of possible analytical techniques available for sensing biomolecules including NMR, mass spectrometry, chromatographic methods and fluorescence techniques to name a few. However, one key technique missing from this list is electrochemistry. Electrochemistry is advantageous in many ways since it allows the rapid, quantitative and sensitive detection of many types of biomolecules, provided they are electroactive. Moreover, electrochemistry is inherently a flux-sensing technique and so opens up the possibility of quantitative dynamic analysis as outlined in this thesis. The major interest is to demonstrate how two broad classes of (bio)physicochemical processes, namely:

(i) the electrochemical detection of biomolecules and (ii) lateral and trans-membrane transport can be studied, analysed and understood using a framework of common principles and methods. As well as advancing these two areas, the work herein may provide a platform for the future application of the approaches described.

1.2 DYNAMIC ELECTROCHEMISTRY

Dynamic electrochemistry describes the process of charge transfer of an electroactive species at an electrode. The general scheme for such an electrode reaction is shown in Figure 1.1 where a species O is transported from the bulk solution to the electrode surface and undergoes electron transfer to produce species R . This process may also involve chemical reactions and adsorption or desorption processes, and the rate of each of the steps in the reaction controls the overall current flow at the electrode.

1.3 ELECTRON TRANSFER PROCESSES

For an electrode reaction where the rate of mass transport is considerably slower than electron transfer, the potential applied to the system can be related to the concentrations of the oxidised and reduced species at the electrode by the Nernst equation.¹

$$E = E^{\ominus} + \frac{RT}{nF} \ln \frac{(O)}{(R)} \quad (1.1)$$

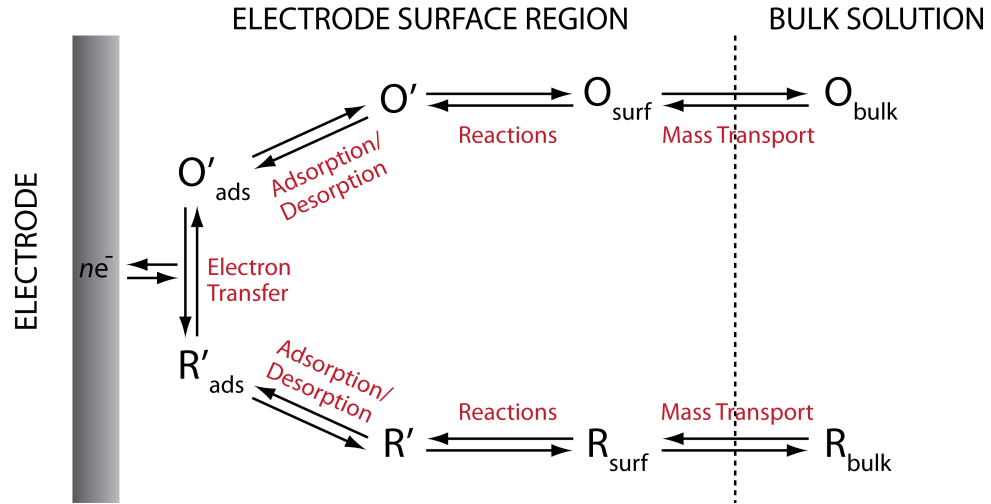


Figure 1.1: Schematic for a general electrode reaction.

where E is the electrode potential, E^\ominus is the standard electrode potential, R is the molar gas constant, T is the temperature, F is the Faraday constant, n is the number of electrons transferred, and O and R are the reduced and oxidised species which are in equilibrium as described by the equation



When mass transport is the kinetically limiting step in the reaction, the system is said to exhibit reversible or Nernstian kinetics as described above. However, when this is not the case, the kinetics of electron transfer must be considered. For this process, the following equations, derived by Butler and Volmer, are used to describe the electron transfer kinetics in terms of the standard rate constant k^0 .¹

$$k_{\text{f}} = k^0 \exp \left[-\alpha \frac{(E - E^{0'})F}{RT} \right] \quad (1.3)$$

$$k_{\text{b}} = k^0 \exp \left[(1 - \alpha) \frac{(E - E^{0'})F}{RT} \right] \quad (1.4)$$

where k_{f} and k_{b} are the forward and reverse rate constants for the equilibrium in equation 1.2, α is the electrochemical charge transfer coefficient and $E^{0'}$ is the electrode formal potential.

1.4 MASS TRANSPORT

For most metallic electrode systems, the transport of the electroactive species to the electrode interface is the kinetically limiting step and is described by the Nernst-Planck equation.²

$$J_i = -D_i \nabla C_i - \frac{z_i F}{RT} D_i C_i \nabla \phi + C_i \underline{v} \quad (1.5)$$

where J_i is the flux of species i to/from the electrode, D_i , C_i , and z_i are the diffusion coefficient, concentration and charge of species i , respectively, ϕ is the electrostatic potential, and \underline{v} is the velocity vector of the solution. This equation can be separated into terms which describe the diffusion, migration and convection of the species in solution, which will be introduced in more detail in this section.

1.4.1 DIFFUSION

As a reaction occurs at an electrode, the reactant is consumed leading to a concentration (strictly activity) gradient from the bulk solution to the electrode surface. This gradient causes the reactant to diffuse and the diffusive flux of this species can be described by Fick's law,²

$$J_{i,d} = -D_i \nabla C_i \quad (1.6)$$

which states that the flux of a molecule is dependent on its diffusion coefficient, D_i , and the concentration gradient. By combining this law with the law of conservation of mass

$$\nabla \cdot C_i = 0 \quad (1.7)$$

Fick's second law² is obtained which describes how the concentration of a species changes over time due to diffusion.

$$\frac{\partial C_i}{\partial t} = D_i \nabla^2 C_i \quad (1.8)$$

The Laplace operator (∇^2) is dependent on the geometry of the system and can take a number of different forms, of which, the 2D axisymmetric and 3D equations are of most relevance in this work. A 2D axisymmetric system can be used to describe diffusion to an ultramicroelectrode (UME) close to a surface (Chapters 5 and 7) whilst a 3D model is necessary to simulate the geometry of a dual-barrel (theta) pipet on a surface (Chapter 4).

1.4.2 MIGRATION

Migration describes the movement of charged species within a solution due to an external electric field ($\nabla\phi$). When a potential is applied in an electrochemical system, charged species are electrostatically attracted to or repelled from the electrode-solution interface, and/or electrolysis occurs, both of which give rise to a migrative flux, which is described by the following equation:

$$J_{i,m} = -\frac{z_i F}{RT} D_i C_i \nabla \phi \quad (1.9)$$

The magnitude of the term $\frac{z_i F}{RT} D_i$ is referred to as the mobility of the species and is denoted u_i . Migration can often be ignored in many electrochemical systems where there is an excess of inert supporting electrolyte compared to any charged analyte, which also serves to reduce the effects of ohmic drop by reducing the solution resistance.¹ However, in systems where the concentration of supporting electrolyte is relatively low, migration must be accounted for, particularly in nanoscale systems (Chapter 4).

1.4.3 CONVECTION

Whereas diffusion and migration describes the movement of species within the solution, convection describes the transport of species carried by the movement of the solution itself. There are two types of convection, *natural convection*, which arises due to thermal gradients or differences in density within the solution, and *forced convection*, where a mechanical force is introduced to the

system to dominate any contribution that may arise from natural convection.¹ The movement of solution due to an applied force can be achieved in a number of ways. This includes flow of the solution over an electrode, movement of the electrode within the solution, or stirring of the solution, which can all increase the rate of mass transport to the electrode. In each of these cases, the resulting movement of the solution is engineered to exhibit well-defined hydrodynamic behaviour so that it can be characterised easily. The general equation to describe the convective flux of a species is given by:

$$J_{i,c} = C_i \underline{\nu} \quad (1.10)$$

For systems where stirring is used to increase the rate of mass transport to an electrode, a stationary layer will exist close to the electrode, in which species can only move via diffusion (assuming migration effects are minimal). This layer is referred to as the unstirred layer (USL), and can play a significant role in the determination of transport rates.³ Failure to account for this accurately can lead to large measurement errors as will be discussed in Chapter 6. For such systems, Fick's second law is adapted to give the convective-diffusion equation:²

$$\frac{\partial C_i}{\partial t} = D_i \nabla^2 C_i - \underline{\nu} \cdot \nabla C_i \quad (1.11)$$

1.5 MICRO- AND NANOSCALE ELECTRODES

Simply adding a convective force may not be sufficient to enhance mass transport to an electrode to a level where electron transfer kinetics can be measured.

Interestingly, diffusion to the electrode can be increased by decreasing the size of the critical dimension of the electrode. On typical experimental timescales, the behaviour of an electrode with a critical dimension in the range of micrometres will deviate from that of electrodes with dimensions on the order of millimetres (macroelectrodes) due to a change in the rate of mass transport.⁴ For a macroelectrode, planar diffusion of the reactant occurs perpendicular to the electrode. In this diffusion regime, unreacted species cannot be delivered to the electrode surface rapidly enough to replace those being consumed and so a depletion layer propagates over time. However, for micrometer (or smaller) sized electrodes, the diffusion profile quickly becomes hemispherical (after imposing a surface reaction to induce diffusion) due to the increased contribution of the radial diffusion component (Figure 1.2).

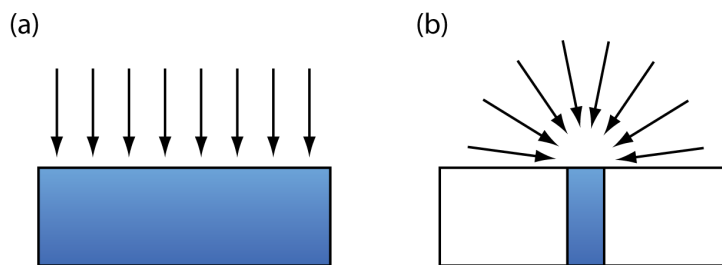


Figure 1.2: (a) Planar diffusion of a species to a macroelectrode and (b) hemispherical diffusion exhibited at a microelectrode.

1.5.1 ULTRAMICROELECTRODES

The most commonly used electrode of this type is the disc ultramicroelectrode (UME), which is fabricated by sealing a small metal wire or carbon fibre in a tapered glass capillary which is subsequently polished to give a well-defined

geometry.² Due to their small size, the currents typically measured at UMEs are on the order of nA or pA. These low currents significantly decrease the effects of “ohmic drop” in solution, the magnitude of which depends on the resistance of the solution and the current flowing.⁵ Other advantages of the small dimensions of UMEs include high current densities and signal-to-noise ratios due to the high mass transport. As instrumentation to measure low currents has improved, the use of UMEs has become more widespread for a variety of applications due to their advantageous properties.⁶⁻⁹

1.5.2 SCANNING ELECTROCHEMICAL MICROSCOPY

One of the most important applications of UMEs is in scanning electrochemical microscopy (SECM), where the physicochemical properties of a substrate can be mapped by moving a probe, such as a UME, above the surface.¹⁰ The probe is connected to a piezoelectric positioning system, which enables movement with nanoscale precision in the x , y and z directions as shown in Figure 1.3. The sample and probe are immersed in electrolyte solution containing a redox mediator. A potentiostat can be used to apply a potential to the UME, and if the substrate is conducting or semiconducting, this can be connected as a second working electrode using a bipotentiostat.¹¹ As the probe is moved towards the substrate, the tip current will start to deviate from the value in bulk solution. If the probe approaches an insulating substrate, the diffusion of species to the electrode becomes hindered and the current decreases, in a process known as negative feedback. Alternatively, if the substrate is conducting and held at an appropriate potential, the redox species consumed at the probe can be regenerated at the substrate. Therefore, as

the tip-substrate distance decreases, the rate of turnover increases, giving a higher current. This mode of operation, where the tip produces and then detects the species of interest, is known as *feedback mode*. SECM of conducting substrates can also be employed in *generation-collection* modes where the redox species is consumed at one of the electrodes and generated at the other. Substrate generation tip collection (SG-TC) is often used to study the electrochemical activity of the substrate for the generation of the redox species. However, when the substrate is heterogeneous, it can be difficult to determine whether the change in current is due to variations in surface activity or topography. To address this, a number of combined techniques have been developed, with the aim of decoupling the response due to electrochemical activity from the topography. These are discussed in section 1.5.4.

Whilst SECM is most commonly used to probe a solid substrate in solution,^{12–15} it should also be mentioned that liquid-liquid interfaces,^{16–19} liquid-gas interfaces,^{20,21} biological tissues^{22–24} and even single cells^{25,26} have all been imaged using this versatile technique.

The tip size is extremely important in SECM as this controls the resolution of the instrument. The reason for the increase in lateral resolution with decreasing tip size is twofold: firstly, the smaller the tip, the smaller the area of the sample probed at a given time, thereby reducing the contribution of signals from neighbouring areas. Secondly, the tip-substrate separation also has a large impact on resolution, with a remote tip leading to a loss in resolution as material is collected from larger regions of the surface. In a typical SECM setup, the tip is positioned at a distance of approximately one radius (of the active part of the electrode) away from the

surface, which means that by decreasing the size of the electrode, it is possible to scan much closer to the surface, as long as there is a mechanism to provide some distance regulation. Because of the importance of the size of the electrode, the trend over the last few decades has been to produce increasingly small electrodes to enhance the resolution of the instrument.^{27–29} Nanoelectrodes for SECM have been fabricated by electrochemically etching a metal wire and sealing in glass, which can produce electrodes with their critical dimension on the order of a few nanometres.^{30,31} The dimension of the metal wire can also be reduced by first sealing in a glass capillary and then pulling using a laser puller to give an extremely fine tip.³² Small scale electrodes are not only important in SECM however, and there are a variety of other techniques which rely on nanoscopic probes to optimise the resolution.

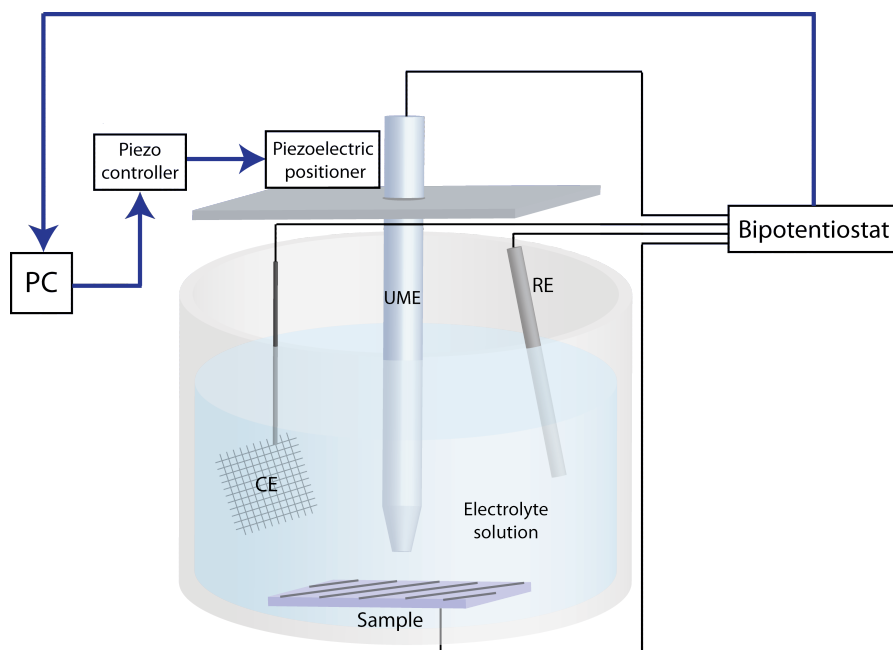


Figure 1.3: Schematic of a typical SECM setup.

1.5.3 SCANNING ION CONDUCTANCE MICROSCOPY

A solid electrode is not always needed to probe a physicochemical process at a surface. In scanning ion conductance microscopy (SICM),³³ the electrode is inserted into a micro- or nanopipet which is filled with an electrolyte solution, and the flux between this electrode and a second electrode in the surrounding solution is measured. In contrast to SECM, the flux measured is a migrative flux, not diffusive or convective since the electrolyte solution is electrochemically inert. As with SECM, there is a strong correlation between the measured flux and distance from the surface, and this can be used to maintain a constant height of the probe from the surface to extract topographical information. Again, the resolution of this technique is entirely dependent on the size of the probe, and since nanopipets are considerably easier to fabricate than nanoelectrodes, this technique has produced extremely high resolution images and has been particularly useful in the study of biological systems.^{34,35}

1.5.4 COMBINED TECHNIQUES

Whilst SECM is a powerful tool in itself, in combination with other techniques, significantly more information can be extracted. For example techniques such as shear force SECM,^{36,37} SECM-atomic force microscopy (AFM)^{38,39} or SECM-SICM^{40,41} can decouple the topography of a substrate from its activity which is not possible with SECM alone. SECM-AFM incorporates an electrode into the AFM tip so that the electrochemical response can be measured as the tip scans across the surface. Alternatively, the electrode can be used to instigate a topographical

change (for example the dissolution of a surface) which can then be mapped.⁴² SECM-SICM probes use dual channels with one open channel (SICM) and the other channel containing an electrode.^{40,41,43–45} Again, with one part of the probe measuring the topography, the response due to the electrochemical activity can easily be determined.

1.6 NON-ELECTROCHEMICAL TECHNIQUES

There are a huge variety of surface techniques for the study of biological systems including those discussed previously. There are, however, many non-electrochemical techniques which also provide valuable information, of which, one important class is fluorescence methods.

1.6.1 CONFOCAL LASER SCANNING MICROSCOPY

One powerful fluorescence-based technique for the study of biological samples is confocal laser scanning microscopy (CLSM), which makes use of a pinhole to improve the spatial resolution compared to a conventional wide-field fluorescence microscope (Figure 1.4).⁴⁶ The pinhole ensures only light originating from the focal plane reaches the detector, which not only eliminates out of focus light but also background light (since only a small area is illuminated at a time), improving signal-to-noise ratios. The sample is excited by focusing a laser beam at a particular excitation wavelength onto a specific area which causes the sample to fluoresce. The beam is focussed onto the sample by a dichroic mirror which reflects this shorter wavelength light, but allows the longer wavelength

emitted light to pass through, so that only light from the sample is collected at the detector.

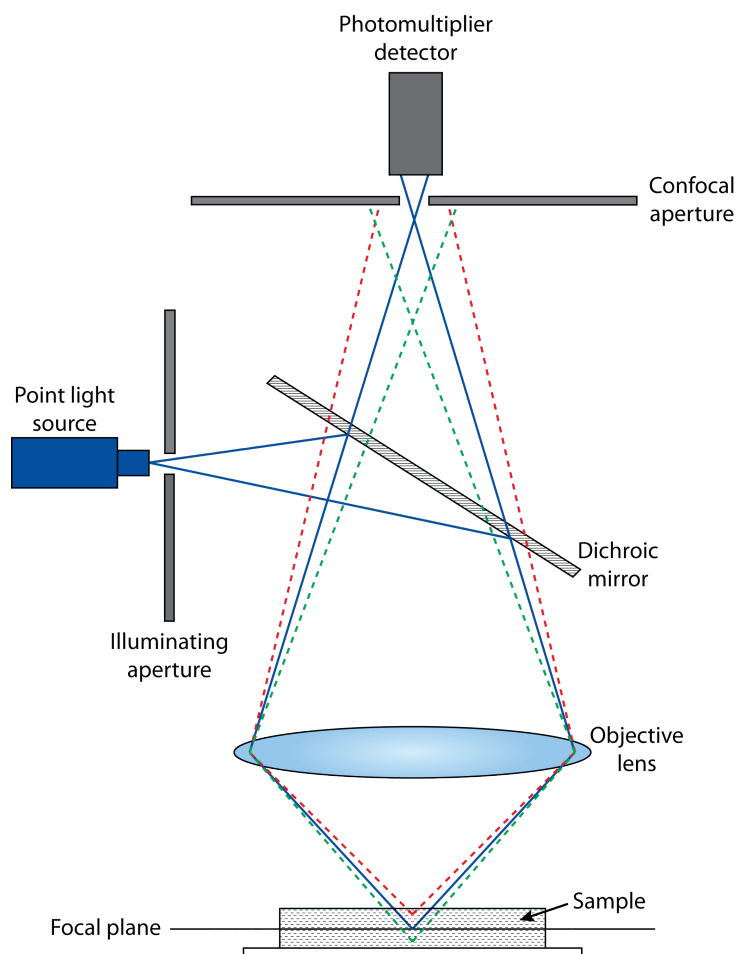


Figure 1.4: Schematic of the principles of the confocal laser scanning microscope. The pinholes reject any out of focus light originating from outside of the focal plane (represented here by the dashed red and green lines), reducing background noise.

The use of the pinholes, combined with point-illumination, greatly increases the resolution of the CLSM and provides another advantage in comparison to conventional microscopy techniques. Figure 1.5 shows that by focussing the laser beam on the sample at different focal depths, a series of images through the

sample can be collected and used to generate a 3D reconstruction, known as a z -stack.⁴⁷ This enables the interior of a sample to be examined non-destructively, which is particularly advantageous for biological samples.⁴⁸

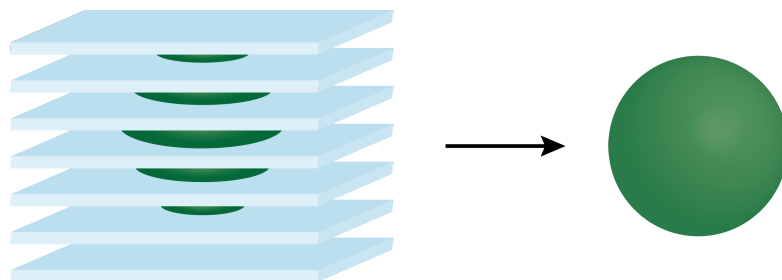


Figure 1.5: Illustration of how a series of 2D images at different focal depths can be reconstructed to produce a 3D image

1.6.2 FLUORESCEIN

For samples which are not naturally fluorescent, a fluorophore may be added to allow visualisation with CLSM. One of the most commonly used fluorophores is fluorescein, the structure of which is shown in Figure 1.6. Highlighted in this figure are the three sites which may be protonated (or not) depending on the pH of the solution. Fluorescein absorbs radiation at 496 nm and emits at 518 nm (giving a Stokes shift of 22 nm),⁴⁸ provided sites 2 (pK_a 4.4) and 3 (pK_a 2.1) remain deprotonated. At high pH, the molecule is negatively charged and highly fluorescent since the pK_a of site 1 is 6.5. As the pH decreases, sites 2 and 3 start to become protonated, increasing the proportion of neutral and positively charged molecules, giving a gradual decrease in fluorescence. This relationship between fluorescence and pH means that with the addition of even low concentrations of fluorescein, the local changes in pH of a system can be mapped⁴⁹ as will be

discussed in Chapters 6 and 7.

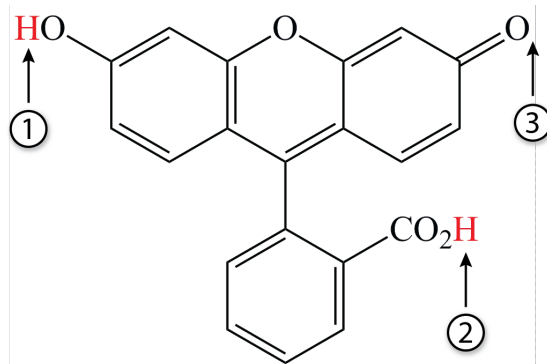


Figure 1.6: The chemical structure of fluorescein with the three available protonation sites labelled.

1.7 BIOMEMBRANES

Every cell is surrounded by a cell membrane, which separates the intra- and extracellular components, and acts as a selectively permeable barrier, which maintains homeostasis within the cell.⁵⁰ Certain species must be able to cross the membrane, for example, to replace molecules being consumed, or to leave the cell as waste products. The principal component of the cell membrane, which prevents molecules from passing freely in or out of the cell, is the phospholipid bilayer. The bilayer is made up of individual amphipathic phospholipid molecules, which spontaneously assemble into this organised structure in an aqueous environment. The structure of the individual phospholipid molecules and assembled bilayer structure are shown in Figure 1.7.

The interaction between the hydrophobic tails of the phospholipids in the interior of the bilayer gives rise to this permeability barrier, particularly to ionic species.

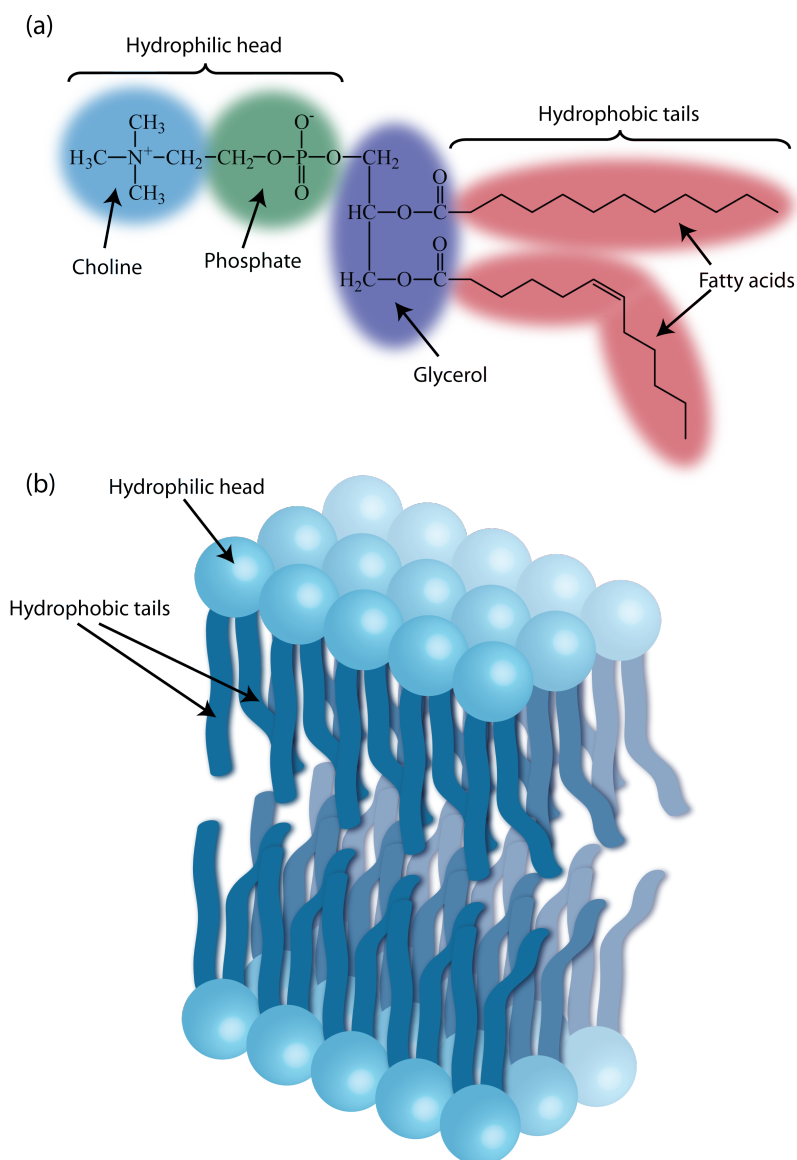


Figure 1.7: (a) Structure of a typical phospholipid molecule with the hydrophilic head and hydrophobic tail regions highlighted. When placed in aqueous solution, the phospholipid molecules spontaneously assemble into the bilayer structure illustrated in (b).

The chemical structure of the phospholipids can affect the structural properties of the bilayer. For example, if the tail groups are unsaturated, kinks will be present, which will prevent close packing of the phospholipids and will therefore

cause the bilayer to be less rigid. If cholesterol is present within the bilayer, this small molecule can occupy the irregular spaces between phospholipid molecules increasing the rigidity of the membrane. In a typical cell membrane, there are a number of types of different phospholipids and cholesterol present, however, these molecules are not evenly distributed, and “lipid rafts” exist, which contain a higher proportion of some lipids and cholesterol than the rest of the bilayer.⁵¹ The fluid mosaic model, proposed by Singer and Nicholson,⁵² describes how the bilayer can be considered as two-dimensional fluid, where the lipid molecules, along with the other components of the cell membrane, can diffuse laterally within the bilayer.

Whilst some small, uncharged molecules are able to diffuse through the bilayer, most molecules can only pass through with the aid of proteins, which are embedded within the bilayer. In some cases, a concentration gradient may exist between the interior and exterior of the cell, but due to the size or charge of the molecule, it still cannot diffuse through the bilayer. In this case, a protein channel is required, which provides an alternative pathway through which the molecule can cross the membrane. Sometimes, however it is necessary to move molecules against a concentration gradient, for example, K^+ and Na^+ ions are pumped across the membranes of neurons to create an imbalance of ions, which allows nerve impulses to propagate. These protein pumps require energy to move molecules across the cell membrane. Membrane proteins, however, are not only involved in the transport of molecules; they have a variety of other functions including signalling, cell-to-cell adhesion and surface recognition, and make up around 50% of the volume of the cell membrane.⁵¹

1.7.1 MODEL CELL MEMBRANES

The transport of molecules across the cell membrane is a fundamental and essential cellular process, and furthering our understanding has many important applications. However, due to the complexity of the cell membrane, isolating the effect of a particular component and how a specific molecule interacts with it is extremely difficult. For this reason, model cell membranes are often used, whereby just the lipid bilayer is present, and is made up of a well-defined composition of lipids.⁵³ Particular protein channels may be incorporated if desired to investigate ion transport,^{54,55} but simple lipid bilayers can be used in isolation to study the passive diffusion of small molecules directly across the membrane.^{56–58}

Typically two types of model cell membrane are often used: planar lipid bilayers, which are two-dimensional bilayer structures,^{59,60} or liposomes,^{61,62} which are spherical bilayer structures encapsulating a small volume of aqueous solution in their interior. Each structure has its advantages and disadvantages, but both have been widely used for a number of applications, including permeability measurements,^{63,64} investigation of membrane protein properties^{65,66} and the structural and mechanical properties of the bilayer,⁶⁷ and binding studies.⁶⁸ In Chapter 6 a novel method of planar lipid bilayer formation is presented, which overcomes some of the limitations of current techniques, and these bilayers are used to investigate rates of passive permeation of small molecules. Planar lipid bilayers prepared from liposomes have also been used in Chapter 7 to investigate the lateral diffusion of protons at the membrane surface.

1.8 CARBON ELECTRODES

Carbon electrodes have been widely used in electrochemistry for many years,^{69–72} due to their favourable properties compared to conventional noble metal electrodes. For example, they are typically inexpensive, have a wide potential window, and electrocatalyse many redox reactions.⁷³ However, for the work presented herein, their main advantage is their biocompatibility. Since the 1990s there has been considerable development of new carbon electrode materials including boron doped diamond, carbon nanotubes and graphene, which offer further benefits including resistance to fouling and improved limits of detection, as well as new applications in electronics and electrocatalysis.⁷⁴

1.8.1 GRAPHITIC CARBON ELECTRODES

Some of the most widely used carbon electrodes are those with an sp^2 hybridised carbon morphology, the simplest being a two-dimensional graphene sheet.⁷⁵ Whilst monolayer graphene has only recently come to prominence, graphitic materials have been widely used in electrochemistry for many years.^{69,70,76,77} Highly oriented pyrolytic graphite (HOPG) is the most ordered of these materials, with in-plane crystallite sizes of over $1\ \mu\text{m}^2$ corresponding to around 10^7 carbon atoms.⁷⁷ This ordered plane with the carbon atoms arranged in a hexagonal lattice is commonly referred to as the “basal plane”, whereas the irregularly structured surface perpendicular to the basal plane is known as the “edge plane”. The basal plane had typically been viewed as being relatively inactive compared to the edge plane,^{78–80} but recent work demonstrated that the

basal plane is in fact, much more active.^{81–84} It can, however, be influenced by the mode of preparation or reaction conditions, which can affect the reproducibility of surface activity measurements.⁸⁵

Carbon fibre electrodes are widely used in electrochemistry, particularly for applications where small electrodes are required such as *in vivo* measurements.^{86,87} They are typically synthesised from precursor polymers, and are aligned such that the graphitic plane is oriented along the length of the fibre.⁷⁴ Because of their small size (typically 5–50 μm), carbon fibre electrodes, have been the most commonly used for the *in vivo* detection of neurotransmitters within the brain,^{88–90} however, they are limited by their sensitivity and susceptibility to fouling.⁹¹

Another important graphitic carbon electrode material is glassy carbon (GC), which is produced via the heat treatment of polyacrylonitrile or other polymers. Typically the polymer is heated to 1000–3000 °C, so that only carbon atoms remain.⁹² Small graphitic planes are formed with lengths of only a few nm, since the C–C bonds do not break and therefore the formation of a full graphite structure is not possible. The structure is typically depicted as intertwined ribbons of graphitic carbon,⁹³ although full structural characterization is difficult due to its disordered nature.⁹⁴

1.8.2 BORON DOPED DIAMOND

Whilst the sp^3 hybridized bonding of carbon atoms produces one of the hardest naturally occurring materials, the low electrical conductivity of diamond means

it is not a particularly interesting electrode material. However, doping the carbon lattice with boron increases the conductivity, since boron is electron-deficient compared to carbon, producing a p-type semiconductor.⁹⁵ At boron concentrations of around 10^{20} atoms cm^{-3} , the diamond undergoes a transition from semiconducting to semimetallic, and as such, becomes useful for electrochemical applications.^{96,97} Boron doped diamond (BDD) is produced by chemical vapour deposition from methane and a boron containing source such as B_2H_6 .⁹⁸ This method produces polycrystalline BDD (pBDD) with grain sizes on the order of a few μm , although larger grains are possible (Figure 1.8). In Chapter 5, the impact of this structural heterogeneity is investigated in terms of the electrochemical activity, to assess the effect of the local dopant density on electron transfer kinetics.

BDD has many advantageous properties compared to other electrode materials, including a wide potential window,⁹⁹ low background currents,¹⁰⁰ and stability in extreme environments.^{97,101} However, for bioelectrochemistry, the principal advantage of BDD is its resistance to fouling due to its inert surface chemistry.¹⁰² This is particularly beneficial, for example, in the detection of neurotransmitters,^{103–106} which are often present in low concentrations and can quickly foul the electrode surface, making detection even more difficult. The advantageous properties of pBDD for the detection of neurotransmitters are investigated in Chapter 3 in comparison to other carbon electrodes, to assess the detection limit of each material and the extent to which fouling occurs.

The surface of BDD electrodes can be modified in a number of ways to improve their properties for different applications. For example, the surface of CVD grown

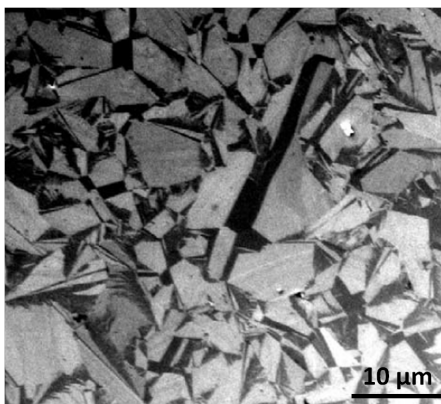


Figure 1.8: FE-SEM image of polycrystalline BDD.¹⁰⁷ The contrast between areas is a result of different boron concentrations in different grains, with lower doped grains lighter in colour.⁹⁶

BDD is usually hydrogen-terminated, making the surface hydrophobic, however, with anodic oxidation in an aqueous environment, the surface becomes oxygen-terminated, and becomes sensitive to the pH of the solution.⁹⁹ Other functional groups can be incorporated by electrochemical methods, which can infer selectively for particular molecules such as DNA or enzymes.¹⁰⁸

BDD is also used as a support for metallic nanoparticles with the aim of exploiting the much higher catalytic activity of nanoparticles compared to a bulk electrode.¹⁰⁹ For this application, the supporting electrode must not be electrochemically active at the potentials where the reaction of interest is taking place, and since diamond has an extremely wide potential window and low background currents, it is ideal for this purpose.⁹⁹ One common use of these modified BDD electrodes is with gold nanoparticles for the amperometric detection of oxygen, which is considerably more sensitive to dissolved oxygen than a bulk gold electrode.¹⁰⁹ Platinum-modified BDD electrodes have also received a significant amount of interest due to their potential applications in fuel cells.¹¹⁰

1.8.3 CARBON NANOTUBES

One further, important class of sp^2 hybridized carbon electrode materials are carbon nanotubes (CNTs), which can be categorized as single walled carbon nanotubes (SWNTs), the structure of which can be thought of as a “rolled up” graphene sheet, or multi walled carbon nanotubes (MWNTs) which consist of several concentric tubes oriented along the same axis.¹¹¹ One of the most common methods of CNT production is arc discharge, where a high potential is applied between two carbon electrodes, vaporizing the surface of one of the electrodes. This material is deposited at the other electrode and contains CNTs amongst other forms of sp^2 carbon.¹¹² The main disadvantage with this method, however, is the need for purification of the CNTs to remove other types of carbon including fullerenes, which are also produced.¹¹³ CNTs can also be produced via catalysed chemical vapour deposition (cCVD), where catalyst nanoparticles such as Fe or Ni are deposited onto a substrate, which is then heated to very high temperatures whilst a carbon feedstock is introduced.¹¹⁴

By controlling the density and arrangement of the nanoparticles, different CNT geometries can be produced, from aligned tubes,¹¹⁵ to random networks,¹¹⁶ to three-dimensional forests (Figure 1.9).¹¹⁷ With this method, the CNTs can be grown on an insulating substrate, to elucidate their electrochemical properties independent of that of the supporting material.¹¹⁸

Individual SWNTs can exhibit either metallic or semiconducting behaviour, depending on the orientation of the hexagonal lattice along the length of the tube,¹¹⁴ however due to the difficulty in isolating single nanotubes, very few

experiments have been carried out to investigate their electrochemical behaviour.^{119,120}

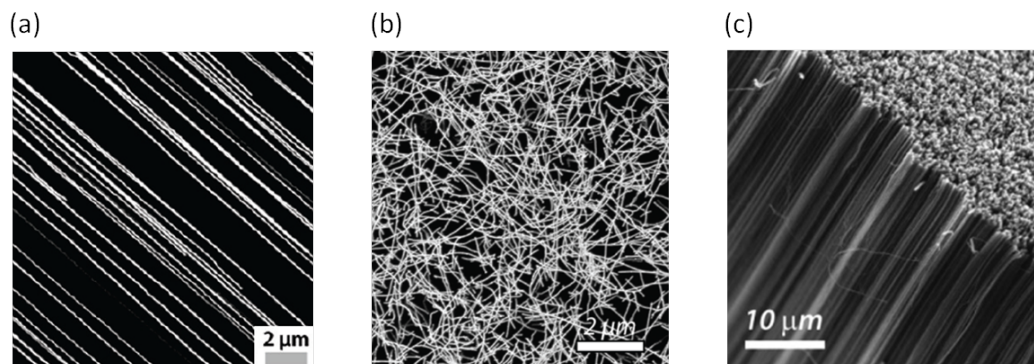


Figure 1.9: Different morphologies of cCVD-grown SWNTs: (a) aligned SWNTs, (b) 2D networks, (c) 3D forests.

CNTs have found a wide range of applications in electrochemistry, from the earliest studies by Britto *et al.*, where unpurified arc-produced CNTs were used to investigate dopamine oxidation.¹²¹ The authors reported the superior electrochemical behaviour of the CNT electrode compared to other carbon electrodes, with ideal reversible oxidation of dopamine observed. Other studies have used the same type of CNTs to investigate the voltammetric response of a number of electroactive species including $\text{Ru}(\text{NH}_3)_6^{3+/2+}$,¹²² ferrocyanide¹²³ and oxygen.¹²⁴ However, the relatively poor characterisation of the CNTs and the likely presence of impurities, means that direct comparisons between CNTs and other carbon electrodes cannot be made.

Other studies have focussed on using purified CNTs to modify other electrode surfaces. Liu *et al.* first demonstrated the possibility of modifying Pt or Au electrodes with purified SWNTs.¹²⁵ This technique was subsequently applied to produce modified glassy carbon electrodes, which exhibited an improved

voltammetric response to dopamine, epinephrine and ascorbic acid compared to that of a bare GC electrode.¹²⁶ Following these initial studies, there has been considerable interest in the use of CNT-modified electrodes to detect a variety of redox species in solution. The supporting electrode material is typically GC or basal plane graphite, onto which purified CNTs are randomly dispersed using a number of methods including drop casting,¹²⁷ abrasive attachment¹²⁸ or the application of CNT composites.¹²⁹ These modified electrodes have shown significant improvements in the detection of a number of biological species including NADH,¹²⁷ norepinephrine¹³⁰ and cytochrome *c*¹³¹ at low overpotentials and with increased sensitivity. The simultaneous detection of dopamine and ascorbic acid has also been reported,¹³² demonstrating the potential applications for these electrodes as sensors *in vivo*. However, once again, the CNTs used to modify the electrodes were subject to very little characterisation. Moreover, there would certainly be effects of purification and additional chemicals used to apply the CNTs to the supporting electrodes, making difficult to determine exactly how the CNTs influence the electrode behaviour. In Chapter 3, the electrochemical detection of serotonin is reported at pristine CNTs grown on insulating substrates, therefore eliminating any contribution to the electrochemical activity from the supporting material. The intrinsic electrochemical response of the CNTs is compared to other carbon electrodes, including pBDD, demonstrating the high sensitivity of the CNTs at low concentrations.

Over the last decade, much work has been done to examine the inherent activity of CNTs, to determine the reasons behind their apparently superior electrochemical properties. Most studies have used commercially available CNTs produced by arc-

discharge or similar methods, which require purification prior to use. Studies have shown that even after extensive purification, many metallic nanoparticles remain in or around the nanotubes, and it has been proposed that it is these metallic impurities which are responsible for the CNTs electroactivity towards a number of redox species.^{133–135}

Alongside the issue of metallic nanoparticle activity, there is a further debate as to the intrinsic CNT electroactivity in terms of its structure. There is a consensus amongst many working in the field, that the sidewalls of the CNTs are relatively inactive and that defects (such as open ends) are responsible for electron transfer.^{136,137} CNTs have often been compared to HOPG, with the sidewalls likened to the basal plane (which is assumed to be inactive), and the nanotube ends and other defects likened to the edge plane (which is assumed to be responsible for electron transfer).^{138,139} Under this assumption, studies have compared different arrangements and morphologies of CNTs, and, largely by CV measurement, have concluded that electrodes with more edge plane-like sites exhibit faster electron transfer rates.^{138,140,141} However, the unknown quality of the CNTs and sometimes poor characterization means that it is difficult to draw conclusions from these macroscale measurements. In addition, since the CNTs are attached to another electrode, the response of the nanotubes cannot be isolated from that of the supporting electrode. To counteract this, more work is being done on SWNTs which are grown directly onto insulating substrates, such as Si/SiO₂, via cCVD. Not only does cCVD produce SWNTs with fewer nanoparticles and less amorphous carbon,¹¹⁴ the configuration means that many high resolution techniques such as AFM, electron microscopy (EM), scanning tunnelling microscopy (STM) and Raman spectroscopy can be employed to

characterize the nanotubes extremely thoroughly.¹¹⁶ These isolated SWNTs show excellent electrochemical properties despite a low concentration of defects (typically one per every 100 nm - 4 μm ¹⁴²) for a range of different mediators.^{118,143,144} Using this method of growth, a number of studies have attempted to examine the activity of the sidewall compared to nanotube ends, by either isolating a portion of an individual nanotube,¹¹⁹ or probing the sidewalls and ends of a three-dimensional forest separately.^{145,146} Each of these studies has shown the sidewalls to be active and the most recent work from this group has shown the responses from sidewalls and ends is extremely consistent.¹⁴⁶ Chapter 4 builds on this work, examining the electrochemical response of defined regions of individual SWNTs to a range of redox mediators, allowing conclusions to be drawn about the activity of the sidewalls in isolation.

1.8.4 GRAPHENE

For completeness, graphene should also be mentioned, as this is closely related to the graphitic materials discussed above. Since the first reports of the preparation of individual graphene sheets in 2004,¹⁴⁷ there has been a surge of interest in the use of this material in a number of areas including electronics,¹⁴⁸ energy storage¹⁴⁹ and conversion,¹⁵⁰ and sensors,¹⁵¹ due to its superior properties including high surface area, high thermal and electrical conductivity, chemical inertness, and mechanical strength.¹⁵²

The first reports of the production of single layer graphene employed the technique of micromechanical exfoliation of HOPG.¹⁴⁷ This involves peeling away layers of the HOPG surface with scotch tape, which can then be transferred to an alternative

substrate. This simple procedure produces single or few-layer graphene with very few defects and as such, has proved an extremely popular technique for graphene research.^{153,154} The limitation of this technique is the difficulty in producing large quantities of graphene, and so alternative methods must be used if graphene is to be used for commercial applications. One potential method of large-scale graphene production is the thermal decomposition of SiC,¹⁵⁵ or SiC-coated surfaces, which can produce sheets of monolayer graphene with areas on the order of tens of μm .¹⁵⁶ However, the reproducibility of the graphene sheets must be improved, and the effects of the interface between the graphene and substrate must be better understood before this technique can be used industrially. Graphene has also been produced from natural graphite by intercalating small organic solvent¹⁵⁷ or acid molecules¹⁵⁸ between the layers, which allows the subsequent separation of the sheets, typically by rapid heating¹⁵⁹ or sonication.¹⁶⁰ Although this method can produce high quality graphene, often only monolayer fragments are obtained, limiting its applications. One way to overcome this problem is with the use of graphite oxide (GO), which can be exfoliated much more easily than graphite.¹⁶¹ However, the graphite oxide contains many functional groups such as hydroxyls and epoxides that make this material an insulator, and although these groups can be removed by reduction, the resulting material contains many defects, which affect its electronic properties.^{151,158}

One recent, novel method of producing graphene is via “unzipping” MWNTs. This can be achieved by the intercalation of molecules within the CNTs, rupturing the nanotube walls,¹⁶² chemical unzipping, whereby the CNT is “cut” along its length by an oxidising agent,¹⁶³ or physical methods, such as plasma etching.¹⁶⁴ These techniques produce extremely narrow graphene sheets

(typically tens of nm in width), termed graphene nanoribbons (GNRs), which have great potential applications in field effect transistors (FET).¹⁶⁵ Since graphene is a zero-gap semiconductor, it would not normally be a suitable material for FET, where non-zero band gap semiconductors are required. However, due to the electronic band structure of graphene, where the conduction and valence bands meet at only a finite number of points, quasi-one dimensional GNRs can exhibit non-zero band gaps if they are sufficiently narrow that their electronic structure does not include any points of intersection.¹⁶⁶

One final promising method for the production of large-scale graphene sheets is CVD of hydrocarbons onto metal substrates such as Ni^{167,168} or Cu.¹⁶⁹ Graphene sheets on the order of cm^2 have been reported with few defects, which can be transferred to an insulating substrate for a variety of applications.¹⁷⁰ In addition, the growth conditions can easily be modified to optimize the size, quality and number of layers of graphene produced.¹⁷¹ Aside from the use of GNR in FET mentioned earlier, graphene has a range of potential applications. Due to the extremely high theoretical surface area of graphene, it is a particularly attractive material for energy storage.¹⁷² Graphene has been used instead of graphite as an anode material in Li-ion batteries,¹⁷³ and in ultracapacitors¹⁷⁴ to improve performance. Graphene sensors for small molecules such as NO_2 , NH_3 , H_2O and CO have proved to be extremely sensitive even down to single-molecule level.¹⁷⁵ Graphene is an ideal sensor material since its whole area is available for the adsorption of these molecules, and its high conductivity means that even a small number of conformational changes due to adsorption affect its resistance.¹⁷⁵ In addition to being an excellent electrode material, graphene is also highly transparent, which makes it a promising candidate for use in liquid crystal

displays, touch screens and solar cells.¹⁷¹ Furthermore, unlike indium tin oxide (ITO), which is currently widely used, graphene is flexible and has a much higher mechanical strength.¹⁶⁵ Finally, as an electrochemical sensor, graphene has the same advantages as carbon nanotubes, but unlike many CNT electrodes, there is no issue with metallic impurities.¹⁷² As a biosensor, graphene electrodes are able to detect dopamine and serotonin in the presence of ascorbic acid,¹⁷⁶ and have been fabricated into novel glucose detectors.¹⁷⁷

1.9 MODELLING

In order to analyse and interpret the results from an electrochemical experiment, a model is often required, to give information on transport processes or reaction kinetics. Whilst sometimes the design of the experimental setup is such that an analytical solution can easily be derived, more often, the geometry may be too complex or there may be multiple processes occurring, which necessitates the use of a numerical simulation to solve the problem. The two principal methods that are commonly used for these types of problem are the finite difference method (FDM) and finite element method (FEM). The FDM generates a solution by discretizing the problem into a series of grid points, with the approximate solution at one point used to generate a solution at the next. Whilst this method is not particularly computationally expensive, the main limitation is the need to represent the geometry of the system as a series of horizontal and vertical lines, which limits the accuracy when dealing with complex geometries such as curved surfaces. One particular version of the FDM, the alternating direction implicit (ADI) method, is commonly used to solve the diffusion equation in two or more

dimensions, and hence is a widely used method in UME and SECM studies.^{14,178–181}

For systems with more complex experimental geometries, the FDM is not a practical option and an alternative method must be found. One option is the finite element method, which uses triangular elements to more accurately map the system geometry. The mathematics of FEM is considerable more complex than FDM, and instead of approximating the differential equations at each point, approximates the solution itself. The triangular mesh can be adapted to give greater resolution in areas where a particular property changes rapidly, for example, the concentration of the electroactive species close to the electrode. By refining the mesh in this region but not elsewhere, the accuracy of the solution is improved, without greatly increasing the computational time. With the wider availability of powerful computational packages, FEM simulations are now much more commonly used for the qualitative analysis of many electrochemical systems.^{182–185}

COMSOL Multiphysics is one such FEM package, which is now widely used for the quantitative analysis of a variety of electrochemical techniques. With this package, complex three-dimensional geometries can be handled, and system equilibria and reactions can be incorporated to accurately model experimental systems. Since the early work of Kwak and Bard¹⁸⁶ who used the finite element method to model SECM approach curves to conducting and insulating substrates, models have become increasingly more complex with the aid of software packages such as COMSOL. For example, Lefrou used a series of simulations performed in COMSOL, to derive an analytical expression for SECM

steady-state positive feedback currents at a series of different tip-substrate separations and UME geometries.¹⁸⁷ Whilst these studies have used the FEM to derive expressions for observed electrochemical currents, more recent work has used simulations to extract information about the electrochemical system which cannot be measured directly. Reaction mechanisms have been proposed based on the results of COMSOL simulations of SECM and linear voltammetry experiments,¹⁸⁸ and determination of reaction kinetics has been the focus of many studies.^{189,190}

Other electrochemical imaging methods have also had their potential applications broadened by the use of COMSOL. The effect of tip geometry on SICM currents measured in different scanning regimes has been investigated, allowing optimisation of the SICM probe for enhanced resolution,¹⁹¹ and in more recent work, SICM coupled with FEM simulations has been used to determine the stiffness of living cells with sub-micrometre resolution, to provide information on the mechanism of cell migration.¹⁹² Recent, novel electrochemical imaging techniques have used COMSOL simulations extensively to maximise the information that can be extracted. Intermittent contact SECM has been used to quantify the flow of material through porous membranes,¹⁹³ and scanning electrochemical cell microscopy has been used to determine heterogeneous electron transfer (HET) rates at a variety of different electrode materials.^{194,195}

In this work, FEM simulations have been used to provide an insight into the reaction kinetics of different systems, and have allowed for the quantitative analysis of system properties that would otherwise only be qualitative. In Chapters 4 and

5, FEM simulations are used to determine the HET kinetics at different electrode materials by analysing the measured electrochemical currents. In Chapters 6 and 7, fluorescence data is interpreted via COMSOL to determine the transport rates of molecules at biological interfaces.

1.10 AIMS OF THIS THESIS

The aim of this thesis is to explore a number of biophysicochemical processes using electrochemistry and related techniques. A number of novel electrochemical probes are investigated for biological applications, and by coupling the results of these experiments with FEM simulations, quantitative kinetic data can be extracted for systems that have previously been difficult to study. Two broad classes of processes are investigated. Firstly, electrochemical processes at novel forms of carbon electrodes, with a view to elucidating key properties, ultimately for the study of biomolecules such as neurotransmitters (Chapters 3-5). Secondly, membrane processes, specifically proton translocation (by weak acids) across membranes, and lateral proton transport along biomembranes (Chapters 6 and 7).

In Chapter 3, the electrochemistry of two novel carbon electrode materials, namely SWNTs and pBDD, is compared to that of commonly used glassy carbon, to determine their suitability for the detection of neurotransmitters at low concentration. The detection limit of each electrode material is assessed, along with the resistance to fouling from oxidation products. These two properties are extremely important in the design of electrodes for *in vivo* sensing,

where concentrations of neurotransmitters are low, and fouling must be minimised to ensure consistent results. Chapter 4 continues to explore the electrochemical response of individual SWNTs to serotonin, as well as simpler redox mediators, with scanning electrochemical cell microscopy. Using this novel electrochemical imaging technique, the question of whether or not SWNT sidewalls are electrochemically active can be addressed, since the activity of a specific region of an SWNT can be probed, independent of the rest of the nanotube. Coupling these results with FEM simulations, allows the rates of heterogeneous electron transfer at the SWNTs to be extracted for different redox mediators. The high mass transport rates in the SECCM setup allow extremely fast HET rates to be measured, which would not be possible with conventional electrochemical techniques.

Intermittent contact scanning electrochemical microscopy (IC-SECM) is another novel, high resolution electrochemical imaging technique, which allows the kinetics of different substrates to be probed. In Chapter 5, IC-SECM is used to investigate the electrochemical response of different regions of pBDD, correlating physical heterogeneities with different electrochemical currents. With the aid of FEM simulations, HET rate constants can be extracted for individual regions, allowing conclusions to be drawn about the origin of these variations.

Switching to biomembranes, Chapter 6 makes use of the high mass transport properties of the probes used in SECCM, to investigate the permeation of weak acid molecules across lipid bilayers. The transport of these species across bilayers formed at the end of theta capillaries, can be observed with the confocal microscope, and permeation rates can be quantified using FEM simulations. The

permeation rates of a series of weak acid molecules are investigated, in order to determine the effect of different properties of the permeant on its rate of transport, with implications for pharmaceutical molecules, whose efficacy depends on their ability to permeate across the cell membrane. The lateral movement of molecules, in particular protons, along cell and organelle membranes is also of considerable interest, as this is a key process in energy production within the cell. In Chapter 7, the lateral diffusion of protons along lipid bilayers is investigated using CLSM, along with the interaction with other biological substrates. A FEM model is designed to quantify the interaction of protons with each of these surfaces, and to extract lateral diffusion coefficients for the transport of protons along the membrane.

From this work, a number of conclusions can be drawn about key biophysicochemical processes, and the electrode materials and techniques used to study them. The impact of these findings and potential areas for future study are summarised in Chapter 8.

1.11 REFERENCES

- [1] Fisher, A. C. *Electrode Dynamics*; Oxford University Press, 1996.
- [2] Bard, A. J.; Faulkner, L. R. *Electrochemical Methods: Fundamentals and Applications*, 2nd ed.; John Wiley & Sons Inc.: New York, 2001.
- [3] Korjamo, T.; Heikkinen, A. T.; Monkkonen, J. *Journal of Pharmaceutical Sciences* **2009**, *98*, 4469–4479.
- [4] Brett, C. M. A.; Brett, A. M. O. *Electrochemistry: Principles, Methods and Applications*; Oxford University Press, 1993.
- [5] Forster, R. J.; Keyes, T. E. In *Handbook of Electrochemistry*; Zoski, C. G., Ed.; Elsevier, 2007.
- [6] Heinze, J. *Angewandte Chemie International Edition* **1993**, *32*, 1268–1288.
- [7] Xie, X.; Stueben, D.; Berner, Z. *Analytical Letters* **2005**, *38*, 2281–2300.
- [8] Orozco, J.; Fernández-Sánchez, C.; Jiménez-Jorquera, C. *Sensors* **2010**, *10*, 475–490.
- [9] Walsh, D. A.; Lovelock, K. R. J.; Licence, P. *Chemical Society Reviews* **2010**, *39*, 4185–4194.
- [10] Wipf, D. O. In *Scanning Electrochemical Microscopy*; Bard, A. J., Mirkin, M. V., Eds.; Marcel Dekker, 2001.
- [11] Wipf, D. O.; Bard, A. J. *Journal of The Electrochemical Society* **1991**, *138*, L4–L6.
- [12] Wipf, D. O.; Bard, A. J. *Journal of The Electrochemical Society* **1991**, *138*, 469–474.
- [13] Mandler, D.; Bard, A. J. *Journal of The Electrochemical Society* **1990**, *137*,

2468–2472.

- [14] Unwin, P. R.; Bard, A. J. *The Journal of Physical Chemistry* **1991**, *95*, 7814–7824.
- [15] Kwak, J.; Lee, C.; Bard, A. J. *Journal of The Electrochemical Society* **1990**, *137*, 1481–1484.
- [16] Shao, Y.; Mirkin, M. V. *Journal of Electroanalytical Chemistry* **1997**, *439*, 137–143.
- [17] Wei, C.; Bard, A. J.; Mirkin, M. V. *The Journal of Physical Chemistry* **1995**, *99*, 16033–16042.
- [18] Solomon, T.; Bard, A. J. *The Journal of Physical Chemistry* **1995**, *99*, 17487–17489.
- [19] Barker, A. L.; Macpherson, J. V.; Slevin, C. J.; Unwin, P. R. *The Journal of Physical Chemistry B* **1998**, *102*, 1586–1598.
- [20] Slevin, C. J.; Macpherson, J. V.; Unwin, P. R. *The Journal of Physical Chemistry B* **1997**, *101*, 10851–10859.
- [21] Slevin, C. J.; Ryley, S.; Walton, D. J.; Unwin, P. R. *Langmuir* **1998**, *14*, 5331–5334.
- [22] Scott, E. R.; White, H. S.; Phipps, J. B. *Analytical Chemistry* **1993**, *65*, 1537–1545.
- [23] Macpherson, J. V.; Beeston, M. A.; Unwin, P. R.; Hughes, N. P.; Littlewood, D. *Langmuir* **1995**, *11*, 3959–3963.
- [24] Nugues, S.; Denuault, G. *Journal of Electroanalytical Chemistry* **1996**, *408*, 125–140.
- [25] Yasukawa, T.; Kaya, T.; Matsue, T. *Electroanalysis* **2000**, *12*, 653–659.
- [26] Amemiya, S.; Guo, J.; Xiong, H.; Gross, D. *Analytical and Bioanalytical*

- Chemistry* **2006**, *386*, 458–471.
- [27] Arrigan, D. W. M. *Analyst* **2004**, *129*, 1157–1165.
- [28] Katemann, B. B.; Schulte, A.; Schuhmann, W. *Electroanalysis* **2004**, *16*, 60–65.
- [29] Etienne, M.; Anderson, E. C.; Evans, S. R.; Schuhmann, W.; Fritsch, I. *Analytical Chemistry* **2006**, *78*, 7317–7324.
- [30] Penner, R. M.; Heben, M. J.; Longin, T. L.; Lewis, N. S. *Science* **1990**, *250*, 1118–1121.
- [31] Watkins, J. J.; Chen, J.; White, H. S.; Abruna, H. D.; Maisonhaute, E.; Amatore, C. *Analytical Chemistry* **2003**, *75*, 3962–3971.
- [32] Katemann, B. B.; Schuhmann, W. *Electroanalysis* **2002**, *14*, 22–28.
- [33] Hansma, P. K.; Drake, B.; Marti, O.; Gould, S. A. C.; Prater, C. B. *Science* **1989**, *243*, 641–643.
- [34] Korchev, Y.; Bashford, C.; Milovanovic, M.; Vodyanoy, I.; Lab, M. *Biophysical Journal* **1997**, *73*, 653–658.
- [35] Shevchuk, A. I.; Frolenkov, G. I.; Sanchez, D.; James, P. S.; Freedman, N.; Lab, M. J.; Jones, R.; Klenerman, D.; Korchev, Y. E. *Angewandte Chemie International Edition* **2006**, *45*, 2212–2216.
- [36] James, P. I.; Garfias-Mesias, L. F.; Moyer, P. J.; Smyrl, W. H. *Journal of The Electrochemical Society* **1998**, *145*, L64–L66.
- [37] Buchler, M.; Kelley, S. C.; Smyrl, W. H. *Electrochemical and Solid-State Letters* **2000**, *3*, 35–38.
- [38] Gardner, C. E.; Unwin, P. R.; Macpherson, J. V. *Electrochemistry Communications* **2005**, *7*, 612–618.
- [39] Macpherson, J. V.; Jones, C. E.; Barker, A. L.; Unwin, P. R. *Analytical*

- Chemistry* **2002**, *74*, 1841–1848.
- [40] Comstock, D. J.; Elam, J. W.; Pellin, M. J.; Hersam, M. C. *Analytical Chemistry* **2010**, *82*, 1270–1276.
- [41] Takahashi, Y.; Shevchuk, A. I.; Novak, P.; Zhang, Y.; Ebejer, N.; Macpherson, J. V.; Unwin, P. R.; Pollard, A. J.; Roy, D.; Clifford, C. A.; Shiku, H.; Matsue, T.; Klenerman, D.; Korchev, Y. E. *Angewandte Chemie International Edition* **2011**, *50*, 9638–9642.
- [42] Macpherson, J. V.; Unwin, P. R.; Hillier, A. C.; Bard, A. J. *Journal of the American Chemical Society* **1996**, *118*, 6445–6452.
- [43] Takahashi, Y.; Shevchuk, A. I.; Novak, P.; Murakami, Y.; Shiku, H.; Korchev, Y. E.; Matsue, T. *Journal of the American Chemical Society* **2010**, *132*, 10118–10126.
- [44] Morris, C. A.; Chen, C.-C.; Baker, L. A. *Analyst* **2012**, *137*, 2933–2938.
- [45] Matsue, T. *Analytical Sciences* **2013**, *29*, 171–179.
- [46] Cox, G. *Materials Today* **2002**, *5*, 34–41.
- [47] Conchello, J.-A.; Lichtman, J. W. *Nature Methods* **2005**, *2*, 920–931.
- [48] Sheppard, C. J. R.; Shotton, D. M. *Confocal Laser Scanning Microscopy*; BIOS Scientific Publishers Ltd., 1997.
- [49] Cannan, S.; Macklam, I. D.; Unwin, P. R. *Electrochemistry Communications* **2002**, *4*, 886–892.
- [50] Vance, D. E.; Vance, J. E. *Biochemistry of Lipids, Lipoproteins and Membranes*, 5th ed.; Elsevier: San Diego, 2008.
- [51] Cooper, G. M. *The Cell: A Molecular Approach*; ASM Press, 2000.
- [52] Singer, S. J.; Nicolson, G. L. *Science* **1972**, *175*, 720–731.
- [53] Montal, M.; Mueller, P. *Proceedings of the National Academy of Sciences*

- 1972**, *69*, 3561–3566.
- [54] Hanke, W.; Methfessel, C.; Wilmsen, U.; Boheim, G. *Bioelectrochemistry and Bioenergetics* **1984**, *12*, 329–339.
- [55] White, R. J.; Ervin, E. N.; Yang, T.; Chen, X.; Daniel, S.; Cremer, P. S.; White, H. S. *Journal of the American Chemical Society* **2007**, *129*, 11766–11775.
- [56] Walter, A.; Gutknecht, J. *Journal of Membrane Biology* **1986**, *90*, 207–217.
- [57] Orbach, E.; Finkelstein, A. *The Journal of General Physiology* **1980**, *75*, 427–436.
- [58] Wolosin, J.; Ginsburg, H. *Biochimica et Biophysica Acta (BBA) - Biomembranes* **1975**, *389*, 20–33.
- [59] Mueller, P.; Rudin, D. O.; Tien, H. T.; Wescott, W. C. *The Journal of Physical Chemistry* **1963**, *67*, 534–535.
- [60] Hirano-Iwata, A.; Niwano, M.; Sugawara, M. *Trends in Analytical Chemistry* **2008**, *27*, 512–520.
- [61] Moscho, A.; Orwar, O.; Chiu, D. T.; Modi, B. P.; Zare, R. N. *Proceedings of the National Academy of Sciences* **1996**, *93*, 11443–11447.
- [62] Angelova, M. I.; Dimiter, S. D. *Faraday Discussions of the Chemical Society* **1986**, *81*, 303–311.
- [63] Kansy, M.; Senner, F.; Gubernator, K. *Journal of Medicinal Chemistry* **1998**, *41*, 1007–1010.
- [64] Sugano, K.; Nabuchi, Y.; Machida, M.; Aso, Y. *International Journal of Pharmaceutics* **2003**, *257*, 245–251.
- [65] Naumann, R.; Baumgart, T.; Grber, P.; Jonczyk, A.; Offenhusser, A.; Knoll, W. *Biosensors and Bioelectronics* **2002**, *17*, 25–34.

- [66] Giess, F.; Friedrich, M. G.; Heberle, J.; Naumann, R. L.; Knoll, W. *Biophysical Journal* **2004**, *87*, 3213–3220.
- [67] Nagle, J. F.; Tristram-Nagle, S. *Biochimica et Biophysica Acta (BBA) - Reviews on Biomembranes* **2000**, *1469*, 159–195.
- [68] Doyle, E. L.; Hunter, C. A.; Phillips, H. C.; Webb, S. J.; Williams, N. H. *Journal of the American Chemical Society* **2003**, *125*, 4593–4599.
- [69] Olson, C.; Adams, R. N. *Analytica Chimica Acta* **1960**, *22*, 582–589.
- [70] Adams, R. N. *Review of Polarography* **1963**, *11*, 71–78.
- [71] Jacobs, E. S. *Analytical Chemistry* **1963**, *35*, 2112–2115.
- [72] Zittel, H. E.; Miller, F. J. *Analytical Chemistry* **1965**, *37*, 200–203.
- [73] Kinoshita, K. *Carbon: Electrochemical and Physicochemical Properties*; Wiley & Sons, 1988.
- [74] McCreery, R. L. *Chemical Reviews* **2008**, *108*, 2646–2687.
- [75] Geim, A. K.; Novoselov, K. S. *Nature Materials* **2007**, *6*, 183–191.
- [76] Olson, C.; Adams, R. N. *Analytica Chimica Acta* **1963**, *29*, 358–363.
- [77] McCreery, R. L. In *Electroanalytical Chemistry*; Bard, A. J., Ed.; Dekker, 1991; Vol. 17.
- [78] Bowling, R. J.; Packard, R. T.; McCreery, R. L. *Journal of the American Chemical Society* **1989**, *111*, 1217–1223.
- [79] Davies, T. J.; Hyde, M. E.; Compton, R. G. *Angewandte Chemie* **2005**, *117*, 5251–5256.
- [80] Ji, X.; Banks, C. E.; Crossley, A.; Compton, R. G. *ChemPhysChem* **2006**, *7*, 1337–1344.
- [81] Edwards, M. A.; Bertoncello, P.; Unwin, P. R. *The Journal of Physical Chemistry C* **2009**, *113*, 9218–9223.

- [82] Lai, S. C. S.; Patel, A. N.; McKelvey, K.; Unwin, P. R. *Angewandte Chemie International Edition* **2012**, *51*, 5405–5408.
- [83] Patel, A. N.; Collignon, M. G.; OConnell, M. A.; Hung, W. O. Y.; McKelvey, K.; Macpherson, J. V.; Unwin, P. R. *Journal of the American Chemical Society* **2012**, *134*, 20117–20130.
- [84] Patel, A. N.; McKelvey, K.; Unwin, P. R. *Journal of the American Chemical Society* **2012**, *134*, 20246–20249.
- [85] Lhenry, S.; Leroux, Y. R.; Hapiot, P. *Analytical Chemistry* **2012**, *84*, 7518–7524.
- [86] Zhang, B.; Heien, M. L. A. V.; Santillo, M. F.; Mellander, L.; Ewing, A. G. *Analytical Chemistry* **2011**, *83*, 571–577.
- [87] Swamy, B. E. K.; Venton, B. J. *Analyst* **2007**, *132*, 876–884.
- [88] Phillips, P. E. M.; Stuber, G. D.; Heien, M. L. A. V.; Wightman, R. M.; Carelli, R. M. *Nature* **2003**, *422*, 614–618.
- [89] Yavich, L.; Jäkälä, P.; Tanila, H. *Journal of Neurochemistry* **2005**, *95*, 641–650.
- [90] Perez, X. A.; Andrews, A. M. *Analytical Chemistry* **2005**, *77*, 818–826.
- [91] Singh, Y. S.; Sawarynski, L. E.; Dabiri, P. D.; Choi, W. R.; Andrews, A. M. *Analytical Chemistry* **2011**, *83*, 6658–6666.
- [92] Harris, P. J. F. *Critical Reviews in Solid State and Materials Sciences* **2005**, *30*, 235–253.
- [93] Jenkins, G. M.; Kawamura, K. *Nature* **1971**, *231*, 175–176.
- [94] McDermott, M. T.; McDermott, C. A.; McCreery, R. L. *Analytical Chemistry* **1993**, *65*, 937–944.
- [95] Pleskov, Y. V. *Russian Journal of Electrochemistry* **2002**, *38*, 1275–1291.

- [96] Wilson, N. R.; Clewes, S. L.; Newton, M. E.; Unwin, P. R.; Macpherson, J. V. *The Journal of Physical Chemistry B* **2006**, *110*, 5639–5646.
- [97] Compton, R. G.; Foord, J. S.; Marken, F. *Electroanalysis* **2003**, *15*, 1349–1363.
- [98] Xu, J.; Granger, M. C.; Chen, Q.; Strojek, J. W.; Lister, T. E.; Swain, G. M. *Analytical Chemistry* **1997**, *69*, 591A–597A.
- [99] Kraft, A. *International Journal of Electrochemical Science* **2007**, *2*, 355–385.
- [100] Yano, T.; Tryk, D. A.; Hashimoto, K.; Fujishima, A. *Journal of The Electrochemical Society* **1998**, *145*, 1870–1876.
- [101] Montilla, F.; Michaud, P.; Morallón, E.; Vázquez, J.; Comninellis, C. *Electrochimica Acta* **2002**, *47*, 3509–3513.
- [102] Xu, J.; Chen, Q.; Swain, G. M. *Analytical Chemistry* **1998**, *70*, 3146–3154.
- [103] Güell, A. G.; Meadows, K. E.; Unwin, P. R.; Macpherson, J. V. *Physical Chemistry Chemical Physics* **2010**, *12*, 10108–10114.
- [104] Dong, H.; Wang, S.; Liu, A.; Galligan, J. J.; Swain, G. M. *Journal of Electroanalytical Chemistry* **2009**, *632*, 20–29.
- [105] Kato, T.; Fierro, S.; Watanabe, T.; Yoshimi, K.; Einaga, Y. *Chemistry Letters* **2012**, *41*, 224–226.
- [106] Sarada, B. V.; Rao, T. N.; Tryk, D. A.; Fujishima, A. *Chemistry Letters* **1999**, *28*, 1213–1214.
- [107] Marken, F.; Paddon, C. A.; Asogan, D. *Electrochemistry Communications* **2002**, *4*, 62–66.
- [108] Kondo, T.; Honda, K.; Tryk, D. A.; Fujishima, A. *Journal of The Electrochemical Society* **2005**, *152*, E18–E23.
- [109] Siné, G.; Duo, I.; Roustom, B.; Foti, G.; Comninellis, C. *Journal of Applied*

- Electrochemistry* **2006**, *36*, 847–862.
- [110] Bennett, J. A.; Show, Y.; Wang, S.; Swain, G. M. *Journal of The Electrochemical Society* **2005**, *152*, E184–E192.
- [111] Dumitrescu, I.; Unwin, P. R.; Macpherson, J. V. *Chemical Communications* **2009**, 6886–6901.
- [112] Ebbesen, T. W.; Ajayan, P. M. *Nature* **1992**, *358*, 220–222.
- [113] Hiura, H.; Ebbesen, T. W.; Tanigaki, K. *Advanced Materials* **1995**, *7*, 275–276.
- [114] Dai, H. *Surface Science* **2002**, *500*, 218–241.
- [115] Rutkowska, A.; Walker, D.; Gorfman, S.; Thomas, P. A.; Macpherson, J. V. *The Journal of Physical Chemistry C* **2009**, *113*, 17087–17096.
- [116] Edgeworth, J. P.; Wilson, N. R.; Macpherson, J. V. *Small* **2007**, *3*, 860–870.
- [117] Burt, D. P.; Whyte, W. M.; Weaver, J. M. R.; Glidle, A.; Edgeworth, J. P.; Macpherson, J. V.; Dobson, P. S. *The Journal of Physical Chemistry C* **2009**, *113*, 15133–15139.
- [118] Dumitrescu, I.; Unwin, P. R.; Wilson, N. R.; Macpherson, J. V. *Analytical Chemistry* **2008**, *80*, 3598–3605.
- [119] Heller, I.; Kong, J.; Heering, H. A.; Williams, K. A.; Lemay, S. G.; Dekker, C. *Nano Letters* **2005**, *5*, 137–142.
- [120] Dudin, P. V.; Snowden, M. E.; Macpherson, J. V.; Unwin, P. R. *ACS Nano* **2011**, *5*, 10017–10025.
- [121] Britto, P.; Santhanam, K.; Ajayan, P. *Bioelectrochemistry and Bioenergetics* **1996**, *41*, 121–125.
- [122] Campbell, J. K.; Sun, L.; Crooks, R. M. *Journal of the American Chemical Society* **1999**, *121*, 3779–3780.

- [123] Nugent, J. M.; Santhanam, K. S. V.; Rubio, A.; Ajayan, P. M. *Nano Letters* **2001**, *1*, 87–91.
- [124] Britto, P. J.; Santhanam, K. S. V.; Rubio, A.; Alonso, J. A.; Ajayan, P. M. *Advanced Materials* **1999**, *11*, 154–157.
- [125] Liu, C.-y.; Bard, A. J.; Wudl, F.; Weitz, I.; Heath, J. R. *Electrochemical and Solid-State Letters* **1999**, *2*, 577–578.
- [126] Luo, H.; Shi, Z.; Li, N.; Gu, Z.; Zhuang, Q. *Analytical Chemistry* **2001**, *73*, 915–920.
- [127] Musameh, M.; Wang, J.; Merkoci, A.; Lin, Y. *Electrochemistry Communications* **2002**, *4*, 743–746.
- [128] Moore, R. R.; Banks, C. E.; Compton, R. G. *Analytical Chemistry* **2004**, *76*, 2677–2682.
- [129] Wang, J.; Musameh, M. *Analytical Chemistry* **2003**, *75*, 2075–2079.
- [130] Wang, J.; Li, M.; Shi, Z.; Li, N.; Gu, Z. *Electroanalysis* **2002**, *14*, 225–230.
- [131] Wang, J.; Li, M.; Shi, Z.; Li, N.; Gu, Z. *Analytical Chemistry* **2002**, *74*, 1993–1997.
- [132] Wang, Z.; Liu, J.; Liang, Q.; Wang, Y.; Luo, G. *Analyst* **2002**, *127*, 653–658.
- [133] Dai, X.; Wildgoose, G. G.; Compton, R. G. *Analyst* **2006**, *131*, 901–906.
- [134] Pumera, M.; Iwai, H. *The Journal of Physical Chemistry C* **2009**, *113*, 4401–4405.
- [135] Banks, C. E.; Crossley, A.; Salter, C.; Wilkins, S. J.; Compton, R. G. *Angewandte Chemie International Edition* **2006**, *45*, 2533–2537.
- [136] Banks, C. E.; Davies, T. J.; Wildgoose, G. G.; Compton, R. G. *Chemical Communications* **2005**, 829–841.
- [137] Chou, A.; Bocking, T.; Singh, N. K.; Gooding, J. J. *Chemical*

- Communications* **2005**, 842–844.
- [138] Banks, C. E.; Moore, R. R.; Davies, T. J.; Compton, R. G. *Chemical Communications* **2004**, 1804–1805.
- [139] Holloway, A. F.; Toghill, K.; Wildgoose, G. G.; Compton, R. G.; Ward, M. A. H.; Tobias, G.; Llewellyn, S. A.; Ballesteros, B.; Green, M. L. H.; Crossley, A. *The Journal of Physical Chemistry C* **2008**, *112*, 10389–10397.
- [140] Li, J.; Cassell, A.; Delzeit, L.; Han, J.; Meyyappan, M. *The Journal of Physical Chemistry B* **2002**, *106*, 9299–9305.
- [141] Liu, J.; Chou, A.; Rahmat, W.; Paddon-Row, M.; Gooding, J. *Electroanalysis* **2005**, *17*, 38–46.
- [142] Fan, Y.; Goldsmith, B. R.; Collins, P. G. *Nature Materials* **2005**, *4*, 906–911.
- [143] Dumitrescu, I.; Edgeworth, J. P.; Unwin, P. R.; Macpherson, J. V. *Advanced Materials* **2009**, *21*, 3105–3109.
- [144] Bertoncello, P.; Edgeworth, J. P.; Macpherson, J. V.; Unwin, P. R. *Journal of the American Chemical Society* **2007**, *129*, 10982–10983.
- [145] Gong, K.; Chakrabarti, S.; Dai, L. *Angewandte Chemie International Edition* **2008**, *47*, 5446–5450.
- [146] Miller, T. S.; Ebejer, N.; Güell, A. G.; Macpherson, J. V.; Unwin, P. R. *Chemical Communications* **2012**, *48*, 7435–7437.
- [147] Novoselov, K. S.; Geim, A. K.; Morozov, S. V.; Jiang, D.; Zhang, Y.; Dubonos, S. V.; Grigorieva, I. V.; Firsov, A. A. *Science* **2004**, *306*, 666–669.
- [148] Berger, C.; Song, Z.; Li, T.; Li, X.; Ogbazghi, A. Y.; Feng, R.; Dai, Z.; Marchenkov, A. N.; Conrad, E. H.; First, P. N.; de Heer, W. A. *The Journal of Physical Chemistry B* **2004**, *108*, 19912–19916.
- [149] Wang, D.; Choi, D.; Li, J.; Yang, Z.; Nie, Z.; Kou, R.; Hu, D.; Wang, C.;

- Saraf, L. V.; Zhang, J.; Aksay, I. A.; Liu, J. *ACS Nano* **2009**, *3*, 907–914.
- [150] Wang, X.; Zhi, L.; Tsao, N.; Tomovi, e.; Li, J.; Mllen, K. *Angewandte Chemie International Edition* **2008**, *47*, 2990–2992.
- [151] Shao, Y.; Wang, J.; Wu, H.; Liu, J.; Aksay, I.; Lin, Y. *Electroanalysis* **2010**, *22*, 1027–1036.
- [152] Rao, C. N. R.; Biswas, K.; Subrahmanyam, K. S.; Govindaraj, A. *Journal of Materials Chemistry* **2009**, *19*, 2457–2469.
- [153] Huc, V.; Bendiab, N.; Rosman, N.; Ebbesen, T.; Delacour, C.; Bouchiat, V. *Nanotechnology* **2008**, *19*, 455601.
- [154] Gass, M. H.; Bangert, U.; Bleloch, A. L.; Wang, P.; Nair, R. R.; Geim, A. K. *Nature Nanotechnology* **2008**, *3*, 676–681.
- [155] Rollings, E.; Gweon, G.-H.; Zhou, S.; Mun, B.; McChesney, J.; Hussain, B.; Fedorov, A.; First, P.; de Heer, W.; Lanzara, A. *Journal of Physics and Chemistry of Solids* **2006**, *67*, 2172–2177.
- [156] Emtsev, K. V.; Bostwick, A.; Horn, K.; Jobst, J.; Kellogg, G. L.; Ley, L.; McChesney, J. L.; Ohta, T.; Reshanov, S. A.; Rhrl, J.; Rotenberg, E.; Schmid, A. K.; Waldmann, D.; Weber, H. B.; Seyller, T. *Nature Materials* **2009**, *8*, 203–207.
- [157] Hernandez, Y. et al. *Nature Nanotechnology* **2008**, *3*, 563–568.
- [158] Li, X.; Zhang, G.; Bai, X.; Sun, X.; Wang, X.; Wang, E.; Dai, H. *Nature Nanotechnology* **2008**, *3*, 538–542.
- [159] Yu, A.; Ramesh, P.; Itkis, M. E.; Bekyarova, E.; Haddon, R. C. *The Journal of Physical Chemistry C* **2007**, *111*, 7565–7569.
- [160] Lotya, M.; Hernandez, Y.; King, P. J.; Smith, R. J.; Nicolosi, V.; Karlsson, L. S.; Blighe, F. M.; De, S.; Wang, Z.; McGovern, I. T.;

- Duesberg, G. S.; Coleman, J. N. *Journal of the American Chemical Society* **2009**, *131*, 3611–3620.
- [161] Park, S.; Ruoff, R. S. *Nature Nanotechnology* **2009**, *4*, 217–224.
- [162] Cano-Márquez, A. G.; Rodríguez-Macías, F. J.; Campos-Delgado, J.; Espinosa-González, C. G.; Tristan-Lopez, F.; Ramírez-González, D.; Cullen, D. A.; Smith, D. J.; Terrones, M.; Vega-Cantú, Y. I. *Nano Letters* **2009**, *9*, 1527–1533.
- [163] Kosynkin, D. V.; Higginbotham, A. L.; Sinitskii, A.; Lomeda, J. R.; Dimiev, A.; Price, B. K.; Tour, J. M. *Nature* **2009**, *458*, 872–876.
- [164] Jiao, L.; Zhang, L.; Wang, X.; Diankov, G.; Dai, H. *Nature* **2009**, *458*, 877–880.
- [165] Choi, W.; Lahiri, I.; Seelaboyina, R.; Kang, Y. S. *Critical Reviews in Solid State and Materials Sciences* **2010**, *35*, 52–71.
- [166] Barone, V.; Hod, O.; Scuseria, G. E. *Nano Letters* **2006**, *6*, 2748–2754.
- [167] Obraztsov, A.; Obraztsova, E.; Tyurnina, A.; Zolotukhin, A. *Carbon* **2007**, *45*, 2017–2021.
- [168] Chae, S. J.; Güneş, F.; Kim, K. K.; Kim, E. S.; Han, G. H.; Kim, S. M.; Shin, H.-J.; Yoon, S.-M.; Choi, J.-Y.; Park, M. H.; Yang, C. W.; Pribat, D.; Lee, Y. H. *Advanced Materials* **2009**, *21*, 2328–2333.
- [169] Li, X.; Cai, W.; An, J.; Kim, S.; Nah, J.; Yang, D.; Piner, R.; Velamakanni, A.; Jung, I.; Tutuc, E.; Banerjee, S. K.; Colombo, L.; Ruoff, R. S. *Science* **2009**, *324*, 1312–1314.
- [170] Reina, A.; Jia, X.; Ho, J.; Nezich, D.; Son, H.; Bulovic, V.; Dresselhaus, M. S.; Kong, J. *Nano Letters* **2009**, *9*, 30–35.
- [171] Kim, K. S.; Zhao, Y.; Jang, H.; Lee, S. Y.; Kim, J. M.; Kim, K. S.; Ahn, J.-

- H.; Kim, P.; Choi, J.-Y.; Hong, B. H. *Nature* **2009**, *457*, 706–710.
- [172] Pumera, M. *The Chemical Record* **2009**, *9*, 211–223.
- [173] Yoo, E.; Kim, J.; Hosono, E.; Zhou, H.-s.; Kudo, T.; Honma, I. *Nano Letters* **2008**, *8*, 2277–2282.
- [174] Stoller, M. D.; Park, S.; Zhu, Y.; An, J.; Ruoff, R. S. *Nano Letters* **2008**, *8*, 3498–3502.
- [175] Schedin, F.; Geim, A. K.; Morozov, S. V.; Hill, E. W.; Blake, P.; Katsnelson, M. I.; Novoselov, K. S. *Nature Materials* **2007**, *6*, 652–655.
- [176] Alwarappan, S.; Erdem, A.; Liu, C.; Li, C.-Z. *The Journal of Physical Chemistry C* **2009**, *113*, 8853–8857.
- [177] Shan, C.; Yang, H.; Song, J.; Han, D.; Ivaska, A.; Niu, L. *Analytical Chemistry* **2009**, *81*, 2378–2382.
- [178] Macpherson, J. V.; Unwin, P. R. *The Journal of Physical Chemistry* **1995**, *99*, 14824–14831.
- [179] Bard, A. J.; Mirkin, M. V.; Unwin, P. R.; Wipf, D. O. *The Journal of Physical Chemistry* **1992**, *96*, 1861–1868.
- [180] Macpherson, J. V.; Unwin, P. R. *The Journal of Physical Chemistry* **1995**, *99*, 3338–3351.
- [181] Demaille, C.; Unwin, P. R.; Bard, A. J. *The Journal of Physical Chemistry* **1996**, *100*, 14137–14143.
- [182] Liljeroth, P.; Johans, C.; Slevin, C. J.; Quinn, B. M.; Kontturi, K. *Analytical Chemistry* **2002**, *74*, 1972–1978.
- [183] O’Mullane, A. P.; Macpherson, J. V.; Unwin, P. R.; Cervera-Montesinos, J.; Manzanares, J. A.; Frehill, F.; Vos, J. G. *The Journal of Physical Chemistry B* **2004**, *108*, 7219–7227.

- [184] Snowden, M. E.; Güell, A. G.; Lai, S. C. S.; McKelvey, K.; Ebejer, N.; O’Connell, M. A.; Colburn, A. W.; Unwin, P. R. *Analytical Chemistry* **2012**, *84*, 2483–2491.
- [185] Patten, H. V.; Meadows, K. E.; Hutton, L. A.; Iacobini, J. G.; Battistel, D.; McKelvey, K.; Colburn, A. W.; Newton, M. E.; Macpherson, J. V.; Unwin, P. R. *Angewandte Chemie International Edition* **2012**, *51*, 7002–7006.
- [186] Kwak, J.; Bard, A. J. *Analytical Chemistry* **1989**, *61*, 1221–1227.
- [187] Lefrou, C. *Journal of Electroanalytical Chemistry* **2006**, *592*, 103–112.
- [188] Sanchez-Sanchez, C. M.; Rodriguez-Lopez, J.; Bard, A. J. *Analytical Chemistry* **2008**, *80*, 3254–3260.
- [189] Calhoun, R. L.; Bard, A. J. *Journal of The Electrochemical Society* **2012**, *159*, F42–F47.
- [190] Zhou, Q.; Wang, Y.; Tallman, D. E.; Jensen, M. B. *Journal of The Electrochemical Society* **2012**, *159*, H644–H649.
- [191] Edwards, M. A.; Williams, C. G.; Whitworth, A. L.; Unwin, P. R. *Analytical Chemistry* **2009**, *81*, 4482–4492.
- [192] Rheinlaender, J.; Schaffer, T. E. *Soft Matter* **2013**, *9*, 3230–3236.
- [193] McKelvey, K.; Snowden, M. E.; Peruffo, M.; Unwin, P. R. *Analytical Chemistry* **2011**, *83*, 6447–6454.
- [194] Güell, A. G.; Ebejer, N.; Snowden, M. E.; Macpherson, J. V.; Unwin, P. R. *Journal of the American Chemical Society* **2012**, *134*, 7258–7261.
- [195] Güell, A. G.; Ebejer, N.; Snowden, M. E.; McKelvey, K.; Macpherson, J. V.; Unwin, P. R. *Proceedings of the National Academy of Sciences* **2012**, *109*, 11487–11492.

CHAPTER 2

EXPERIMENTAL METHODS

This chapter describes the materials and methods used throughout this thesis. Details are given about the different electrode materials used, including methods of preparation and characterisation. The instrumentation used for different microscopic techniques is discussed, including a detailed description of the scanning electrochemical cell microscope, which has only recently been developed. Finally, the process of designing and implementing a finite element simulation is presented, and methods for data analysis are discussed.

2.1 CHEMICALS

All solutions were prepared with 18.2 M Ω Milli-Q reagent water (Millipore Corp.). Details of all chemicals used in this thesis are given in Table 2.1. Solution pH values were measured with a pH meter (UltraBASIC pH meter, Denver Instruments) and all experiments were performed at room temperature (~ 22 °C)

Table 2.1: List of chemicals used in this thesis.

| Chemical | Purity | Supplier |
|---|----------------------------------|------------------------|
| Ferritin (horse spleen) | 50 - 150 mg/ml in 150 mM NaCl | Sigma-Aldrich |
| Ethanol | > 99.99% | Fisher Scientific Ltd. |
| Sodium chloride (NaCl) | > 99.9% | Fisher Scientific Ltd. |
| Potassium nitrate (KNO ₃) | > 99.99% | Fisher Scientific Ltd. |
| Potassium chloride (KCl) | > 99.99% | Sigma-Aldrich |
| Phosphate buffer solution, pH 7.2 | | Fluka |
| Serotonin hydrochloride | > 98% | Sigma-Aldrich |
| Ruthenium (III) hexaamine (Ru(NH ₃) ₆ ³⁺) | > 99% | Strem Chemicals Ltd. |
| Ferrocenylmethyltrimethylammonium (FcTMA ⁺) | | Prepared in-house |
| Sodium acetate | > 99% | Sigma-Aldrich |
| Sodium propionate | > 99% | Sigma-Aldrich |
| Sodium butyrate | > 98.5% | Sigma-Aldrich |
| Sodium hexanoate | > 99% | Sigma-Aldrich |
| HEPES | > 99% | Fluka |
| Fluorescein sodium salt | | Sigma-Aldrich |
| Dichlorodimethylsilane | > 99% | Fluka |
| Silver nitrate (AgNO ₃) | | BDH |
| Mercury (I) nitrate dihydrate (Hg ₂ (NO ₃) ₂ ·2H ₂ O) | > 97% | Sigma-Aldrich |
| Nitric acid (HNO ₃) | Laboratory reagent grade | Fisher Scientific Ltd. |
| Poly-L-lysine | > 99% | Sigma-Aldrich |
| Poly-L-glutamic acid | > 99% | Sigma-Aldrich |
| 1,2-dipalmitoyl- <i>sn</i> -glycero-3- phosphocholine (DPPC) | > 99% | Avanti Polar Lipids |
| Soy phosphatidylcholine (PC) | > 95% | Avanti Polar Lipids |
| Egg phosphatidylcholine (PC) | > 99% | Avanti Polar Lipids |
| 1,2-dioctadecanoyl- <i>sn</i> -glycero- 3-phospho-(1'- <i>rac</i> -glycerol) (DSPG) | > 99% | Avanti Polar Lipids |
| Chloroform | > 99.8% | Sigma-Aldrich |

2.2 ELECTRODE MATERIALS

2.2.1 CNT GROWTH

All CNTs were grown via catalytic chemical vapour deposition (cCVD) on insulating substrates to which catalytic, metal nanoparticles had been applied. Growth took place in a CVD reactor, through which a mixture of gases flowed during the growth process. Ethanol was used as the carbon feedstock, which was submersed in an ice bath to maintain its temperature at 0 °C. Argon was bubbled through the ethanol before flowing into the tube furnace, to transport the carbon source to the substrate. For the different morphologies of SWNTs grown, different substrates, catalysts and growth conditions were used, which are detailed in the following sections.

2D CNT NETWORKS

Quartz wafers (Hoffman Materials Inc., 500 mm thick with double side polish) were cut into 1.5×1.5 cm squares and Co catalyst was deposited by sputtering (Quorum Technologies SC7640 sputter coater) from a target consisting of Co foil attached to an aluminium target holder using conductive carbon cement. The quartz samples were sputtered for 20 s with 10 mA plasma current and 1 kV voltage. The substrates were heated in a CVD oven, shown in Figure 2.1, consisting of a 1 inch diameter quartz tube (Enterprise Q ltd.) in a tube furnace (Lindberg/Blue M, Thermo-Fisher Scientific, US), to 850 °C from room temperature in 20 min under a flow of 150 standard cubic centimetres per minute

(sccm) H_2 . The temperature was allowed to stabilise at $850\text{ }^\circ\text{C}$ for 5 min before growth was initiated. The carbon feedstock (ethanol) was then introduced via a flow of Ar (850 sccm), which was maintained for 10 min. After the growth phase, the argon flow was terminated and the substrates were allowed to cool under the flow of hydrogen. Previous work has shown that growth using this method produces little amorphous carbon.^{1,2} To provide a macroscopic electrical contact to the CNTs, an Au band (70 nm, with a 2 nm Cr adhesive layer) was thermally evaporated (Moorfield Minibox evaporator) onto the CNT samples. For electrochemical measurements, a sharp tip probe (xyz 300TR Quarter Research) was employed to make electrical connection to the gold band.

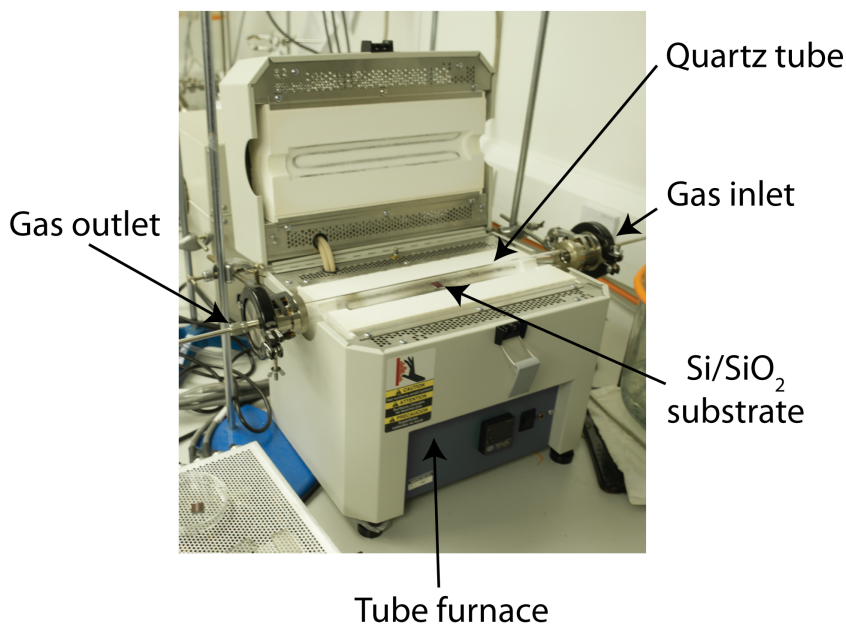


Figure 2.1: CVD system for the growth of 2D CNT networks.

FLOW ALIGNED SWNTs

SWNTs were grown on silicon/silicon oxide substrates (IDB Technologies Ltd., n-type Si, 525 μm thick with 300 nm thermally grown SiO_2) cut into 1 cm \times 1 cm squares. Each substrate was partially immersed in an aqueous solution of horse spleen ferritin, diluted from the original concentration in a ratio of 1:200, to give a band of Fe catalyst nanoparticles along one side of the substrate. The substrates were ashed in an oxygen plasma for 2 minutes (K1050X plasma system, Emitech, UK; O_2 pressure 6×10^{-1} mbar) to break down the protein shell of the ferritin molecules, exposing the catalytic iron nanoparticles stored within.³ The samples were then placed in the cold wall CVD reactor with the area of catalyst nanoparticles in line with the direction of flow (Figure 2.2). The samples were heated to 950 $^\circ\text{C}$ under a flow of 150 sccm H_2 and 250 sccm Ar in 5 minutes. Ethanol was then introduced to the system via a flow of 250 sccm Ar with 150 sccm H_2 , which was maintained for 5 minutes. After this period, the flow of ethanol and H_2 was terminated and the system was left to cool under a flow of 1000 sccm Ar. A macroscopic electrical contact to the SWNT network was provided by an evaporated Pd band (60-90 nm, with a 2 nm Cr adhesive layer).

2.2.2 POLYCRYSTALLINE BORON DOPED DIAMOND

For all the work in this thesis, high quality pBDD with a $\sim\text{nm}$ smooth surface (Element Six Ltd., Ascot, UK) was used. For the cyclic voltammetry measurements in Chapter 3, the pBDD was laser cut into 1 mm column and acid cleaned, resulting in an oxygen terminated surface. An electrical contact was

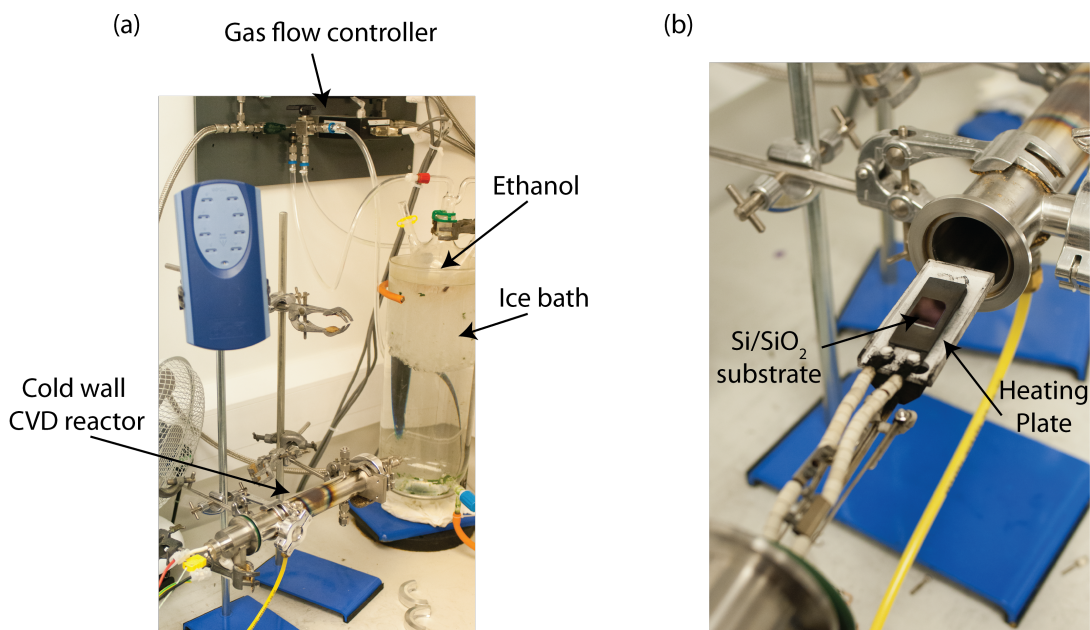


Figure 2.2: CVD system for the growth of flow aligned SWNTs. (b) Interior of the CVD reactor showing the alignment of the substrate.

made and the pBDD was sealed into a glass capillary, producing a disk electrode.⁴ In Chapter 5, a 2 mm column of pBDD with an average dopant concentration of $\sim 5 \times 10^{20}$ atoms cm^{-3} was laser cut, and electrically connected and isolated using procedures described previously.⁵

2.2.3 Pt ULTRAMICROELECTRODE CHARACTERISATION

For intermittent contact SECM (IC-SECM) measurements (Chapter 5), 2 μm Pt UMEs were fabricated in house from Wollaston wire as described elsewhere,⁶ and the size of the electrode determined from equation 2.1 by recording the limiting current (i_{lim}) for the reduction of $\text{Ru}(\text{NH}_3)_6^{3+}$ or oxidation of FcTMA^+ in solution using diffusion coefficients, D , of $8.8 \times 10^{-6} \text{ cm}^2 \text{ s}^{-1}$ and $6.0 \times 10^{-6} \text{ cm}^2 \text{ s}^{-1}$

respectively.

$$i_{\text{lim}} = (4x)naFDc \quad (2.1)$$

Here x is a function of the RG (ratio of glass to Pt radius) of the UME ($x = 1.02$ when $\text{RG} = 10$),⁷ n is the number of electrons involved in the redox reaction (1 for both cases), a is the radius of the electrode and c is the concentration of the redox species.

2.3 ELECTROCHEMICAL MEASUREMENTS

Electrochemical measurements were performed using a potentiostat (CH760A, CH Instruments) in a three electrode setup, unless otherwise stated. For the cyclic voltammetry measurements in Chapter 3, the GC and pBDD working electrodes were polished with alumina paste (0.05 μm) and washed with Milli-Q water between measurements to avoid contamination. The CNTN electrode was washed with Milli-Q water and dried in a nitrogen stream after each measurement.

In Chapters 4 and 6, purpose-built, high sensitivity current to voltage converters were used for current measurements, with data acquisition performed using an FPGA card (7852R, National Instruments) with a LabVIEW 9.0 interface.

2.4 CHARACTERISATION TECHNIQUES

2.4.1 ATOMIC FORCE MICROSCOPY

CNT characterisation was performed by atomic force microscopy (AFM) using a Veeco Enviroscope with Nanoscope IV controller in tapping mode. Measurements were performed in air using Si tips (RFESP-type, Veeco Probes). CNT heights were determined from image analysis using Gwyddion V2.0, a scanning probe microscopy data analysis software.

2.4.2 RAMAN SPECTROSCOPY

Further characterisation of the CNTs and pBDD samples was carried out using Micro-Raman spectroscopy. A Micro-Raman RenishawInVia Microscope with incorporated Leica microscope was employed using an Ar⁺ laser at excitation wavelength 514.5 nm. For quantitative analysis of the pBDD spectra, the area beneath the peak centred at $\sim 1332\text{ cm}^{-1}$ was integrated and plotted as a function of the position of the laser. Spectra were recorded at intervals of $1.2\text{ }\mu\text{m}$ over the wavenumber range $900\text{--}1800\text{ cm}^{-1}$.

2.4.3 PRESSURE/AREA ISOTHERMS

Pressure/area isotherms were recorded using a Langmuir trough (Nima Technology, Model 611D), with surface pressures measured using a Wilhemy balance. Before any monolayer compression measurements were made, the

Langmuir trough was thoroughly cleaned with chloroform, and a pressure/area isotherm was run on Milli-Q water to check for the presence of any surface contamination. After cleaning, 50 μ l of 0.5 mg/ml DPPC in chloroform was deposited onto the 0.1 M KCl subphase, and the solvent allowed to evaporate before compression was initiated.

2.5 MICROSCOPY TECHNIQUES

2.5.1 SCANNING ELECTROCHEMICAL CELL MICROSCOPY (SECCM)

TIP FABRICATION

SECCM tips were pulled from borosilicate theta capillaries (TG 150-10, Harvard Part No. 30-0114) using a Sutter P-2000 laser puller to give pipets with approximately 400 nm diameter tip openings, measured accurately by field emission-scanning electron microscopy (FE-SEM; Zeiss SUPRA 55-VP). In order to confine the size of the meniscus to the pipet tip, each pipet was silanized by submerging the end in dimethyldichlorosilane whilst flowing through argon at high pressure to avoid silanization of the inside of the pipet. Each barrel was filled with electrolyte solution containing the redox species of interest, and a chloridized silver wire, acting as a QRCE, was inserted into each barrel. Full details of the composition of the solutions used can be found in Chapter 4.

INSTRUMENTATION

The home-built SECCM setup consisted of a one-axis piezoelectric positioner (P-753.31C, Physik Instrumente), onto which the tip was mounted, and a second, two-axis piezoelectric stage (P-622.1CD, Physik Instrumente) positioned below, on which the sample was positioned (Figure 2.3(a)). A sinusoidal oscillation in the z -direction was applied to the tip by means of an AC signal generated by a lock-in amplifier (SR830, Stanford Research systems), and applied to the one-axis piezoelectric positioner via a home-built signal adder. Home-built, high sensitivity current to voltage converters were used to measure currents between the barrels and at the substrate. Tip and substrate positioning and data acquisition were performed using an FPGA card (7852R, National Instruments) with a LabVIEW 9.0 interface.

IMAGING PROCEDURE

For SECCM scans, a potential bias of 0.5 V was typically applied between the two QRCEs inducing an ion current between the barrels. The tip was oscillated in the z -direction at 230 Hz with a peak to peak amplitude of 50 nm. As the meniscus was brought into contact with the sample, an AC component of the conductance current was induced, due to the periodic deformation of the meniscus with the tip oscillation.⁸ The AC component was detected through the lock-in amplifier and used as a set point for imaging, to maintain a constant distance between the end of the tip and the substrate.

The substrate was connected as the working electrode, and the amperometric

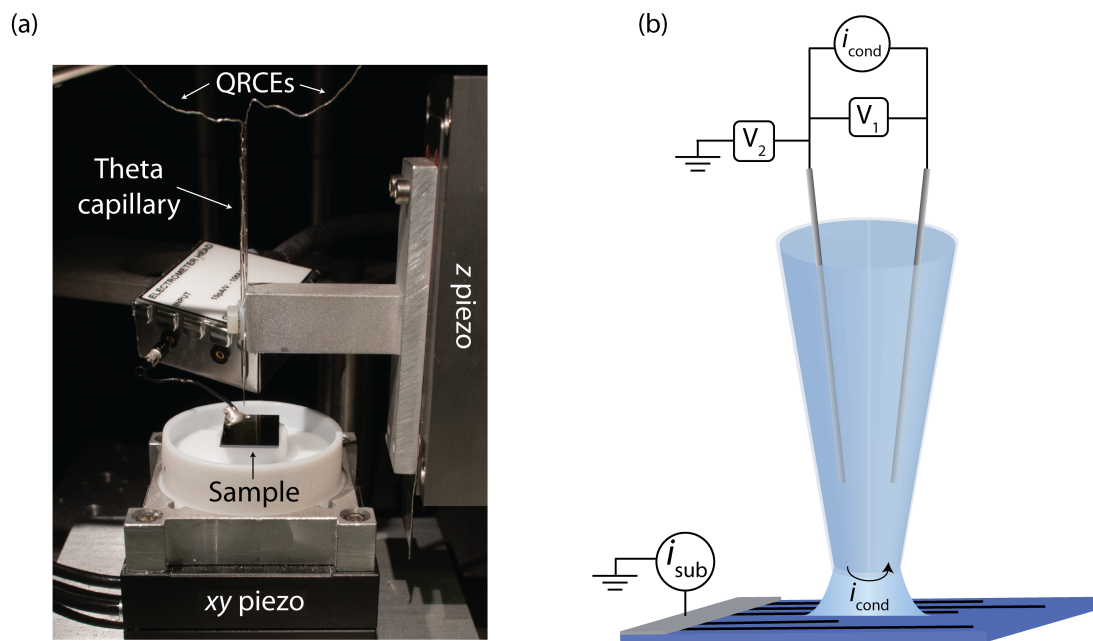


Figure 2.3: (a) SECCM setup for a typical experiment. (b) Illustration of the meniscus of the SECCM tip scanning over SWNTs. The applied potentials and measured currents are also depicted.

current was recorded by grounding the substrate and varying the potentials of the two QRCEs whilst maintaining a constant bias between them. The potential experienced by the substrate is approximately the midpoint of the potential of the two QRCEs. Figure 2.3(b) illustrates this electrical circuit, which is completed when the tip makes contact with the substrate. In each SECCM scan, the tip was scanned across the sample at a rate of 300 nm s^{-1} and data were collected at 488 Hz giving a spatial resolution between data points of around 0.6 nm. A vast amount of information can be extracted from the electrochemical and conductance currents in the SECCM setup which is discussed in Chapter 4.

2.5.2 IC-SECM MEASUREMENTS

High resolution electrochemical images of a pBDD substrate were recorded using IC-SECM in Chapter 4. Positioning of the UME was controlled by a two-axis piezoelectric positioner (PIHera P-625.2CD, Physik Instrumente) in the x, y -direction and a one-axis piezoelectric positioner (PIHera P-621.ZCD, Physik Instrumente) in the z -direction, through a data acquisition card (NI PCIe-6259, National Instruments) from a PC with a LabVIEW 9.0 interface. A sinusoidal oscillation with a frequency of 80 Hz was generated by a sine wave generator (Digimess TG100, Digimes), which was applied to the piezoelectric positioner controller via a home-built signal adder. The UME was approached towards the surface until intermittent contact was detected. This was determined by observing a damping of the oscillation of the piezoelectric positioner and was used as a feedback parameter during the scan to maintain a constant tip-substrate separation. In substrate generation tip collection mode, the substrate and UME were both connected as working electrodes, biased at appropriate potentials to generate and collect the redox species respectively. Once tip-substrate contact had been detected, the UME was scanned across the surface as in conventional SECM.

2.5.3 CONFOCAL LASER SCANNING MICROSCOPY

CLSM experiments were performed using a Leica TCS SP5 X confocal system on a Leica DMI6000 inverted microscope. An Ar laser at 488 nm was used to excite the fluorescein in solution and the resulting emission was collected between 500

and 540 nm. Samples were mounted on an aluminium sample holder (fabricated in house) and the entire assembly was housed in a Faraday cage mounted on the CLSM stage.

For visualisation of weak acid permeation (Chapter 6), the line scan frequency was 1400 Hz. To produce a 3D fluorescence profile, a series of $x-y$ slices were collected at 1 μm intervals in the z -direction. In Chapter 7, line scans at a distance of 10 μm from the substrate were captured with a scan speed of 8000 Hz and $16 \times$ line averaging, giving a data acquisition rate of one image every 2 ms, in order to track the change in fluorescence over time.

2.6 SURFACE MODIFICATION WITH ULTRATHIN FILMS

For the lateral proton diffusion studies in Chapter 7, glass surfaces were modified with a number of different coatings. Poly-L-lysine (PLL) was deposited by drop coating a solution of 1 mg/ml PLL onto glass coverslips. After 20 minutes, the excess PLL was removed by washing with Milli-Q water and drying in an air flow. This produced a uniformly positively charged surface. To produce negatively charged substrates, poly-L-glutamic acid (1 mg/ml) was deposited by the same method onto samples with an existing PLL coating.

Supported lipid bilayers were produced by incubating glass coverslips with small unilamellar vesicle (SUV) solutions. To prepare the SUVs, egg PC and DSPG lipid were dissolved in chloroform in the desired ratios to a final concentration of 1

mg/ml. The solution was dried in a nitrogen stream and desiccated for 4 hours to remove all of the chloroform solvent. The lipids were resuspended in the aqueous solution (0.1 M KNO_3 and 8 μM fluorescein) and sonicated for 2 minutes. This solution was then frozen and thawed five times using dry ice and warm water, before repeatedly extruding through 100 nm polycarbonate membranes using the LiposoFast apparatus.

2.7 SIMULATION DETAILS AND ANALYSIS

2.7.1 SIMULATION DETAILS

All simulations were performed with COMSOL Multiphysics (v3.5a for the simulations in Chapter 5, v4.2a for Chapter 6, and v4.3 for Chapters 4 and 7) (COMSOL AB, Sweden). Analysis of the data was performed in Matlab 2010a (Mathworks Inc., Cambridge). The specific details of each simulation are given in Chapters 4-7, however, the section below details the general method of simulating an electrochemical process. For each simulation in this thesis, the Nernst-Planck equation is solved,⁹ however, for the processes being modelled, the convective term is not included, and migration is only accounted for in Chapter 4.

2.7.2 BUILDING THE MODEL

When modelling any system, the geometry of the domain of interest must first be defined. It is not necessary to simulate the entire experimental setup, as often this would be computationally inefficient, but a large enough region must be simulated

to prevent the edges of the simulation domain influencing the interior. A mesh is then defined, in which a numerical approximation to the mass transport equations is sought for each element during the simulation. To ensure the solution is accurate, the mesh must be fine enough to allow for sharp changes in the concentration of a particular species. The resolution of the mesh can be defined differently on each boundary to minimise the overall number of elements required as is shown in Figure 2.4(a).

Once the geometry and mesh have been defined, boundary conditions are implemented around the edges of the simulation domain. Some of the most common boundary conditions are listed in Table 2.2, along with a short description of when they are implemented.

Finally, initial conditions are defined for the concentration of each species and any applied potentials. Reactions, including equilibria can be defined, and the properties of each species, such as diffusion and mobility coefficients must be entered. The system can then be solved for the time-dependent or steady-state case, by finding a consistent solution to the Nernst-Planck equation for each mesh element. Figure 2.4(b) shows a normalised concentration profile produced by solving the Nernst-Planck equation subject to boundary conditions indicated.

2.7.3 DATA ANALYSIS

Using simulations it is possible to determine an unknown parameter in the experimental system based on the results observed. For example, in Chapters 4

Table 2.2: Description of some of the common boundary conditions implemented in the modelling programmes described herein.

| Boundary Type | Equation | Description |
|----------------|--|---|
| Axial symmetry | $0 = \nabla c \cdot \underline{n}$ | For axisymmetric models, this condition is implemented on the boundary around which the domain is rotated |
| No Flux | $0 = \nabla c \cdot \underline{n}$ | There is no net change in concentration across the boundary, i.e. it is inert |
| Concentration | $c = x$ (e.g. c^* , 0) | The concentration is set to a particular value. Most commonly this is a bulk value, where, in the experimental setup there is no change in the variable beyond this point |
| Flux | $D \frac{\partial c}{\partial z} = f(c)$ | This describes the flux of a particular species across a boundary, for example, the oxidised or reduced form of a redox species as it loses or gains an electron at the electrode surface, or a species permeating across a bilayer |
| Potential | $V = V^*$ | Applies an electric potential to the boundary |

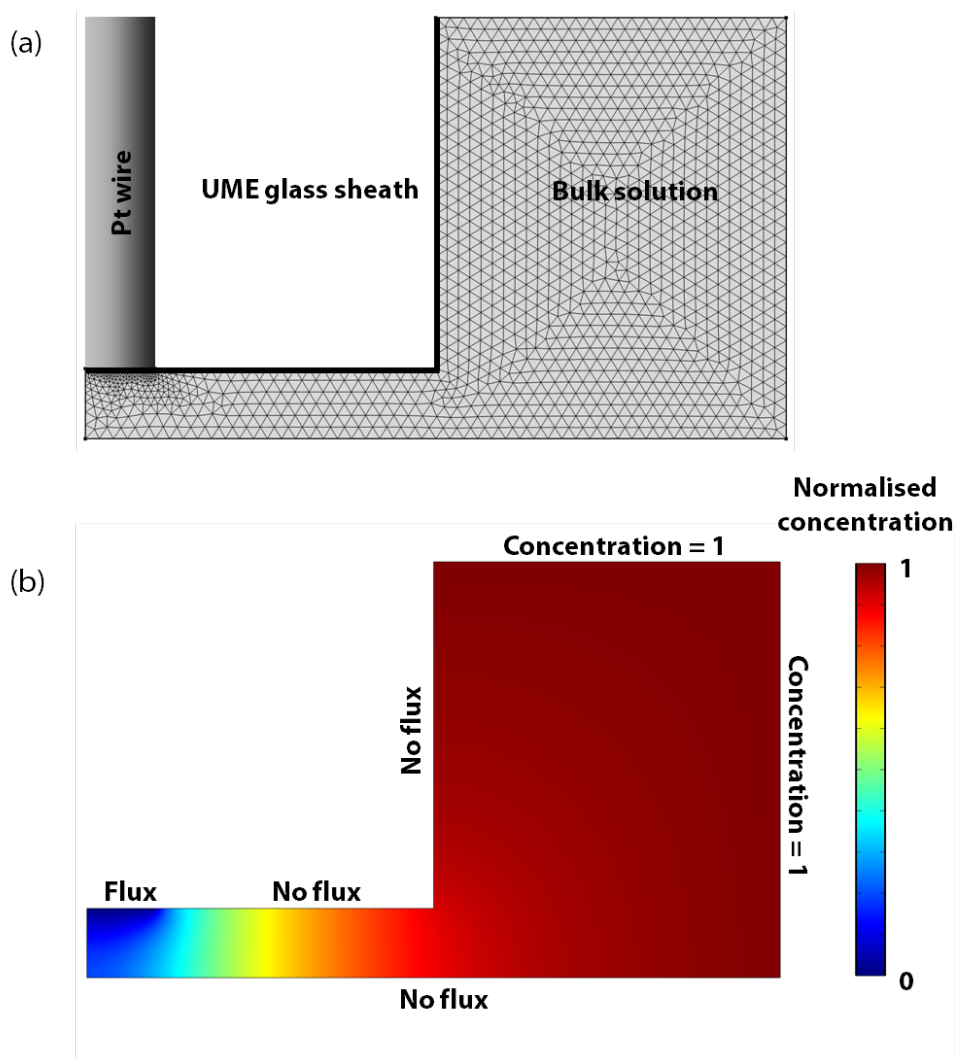


Figure 2.4: (a) Example geometry and mesh, and (b) normalised concentration profile for the simulation of a UME near an inert substrate.

and 5, simulations are used to extract the standard rate constant k^0 of the electrode material based on the observed currents. To achieve this, the simulation is run for a series of different k^0 values, which are then plotted against the simulated current to produce a working curve (Figure 2.5).¹⁰ Thus, by inputting the experimental current, a k^0 value can be obtained. If there are two

unknowns and two pieces of experimental data to match, a working plane can be generated, as is used in Chapter 4.

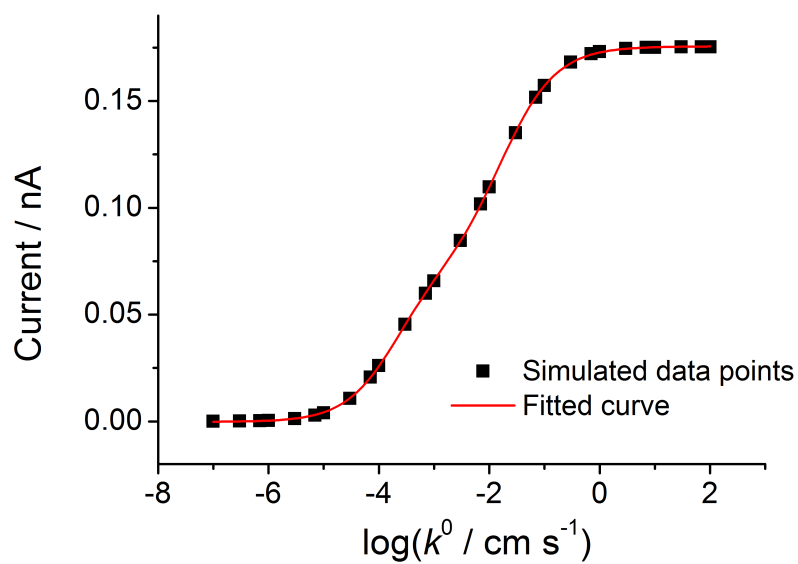


Figure 2.5: Example working curve relating k^0 to tip current.

2.8 REFERENCES

- [1] Dumitrescu, I.; Dudin, P. V.; Edgeworth, J. P.; Macpherson, J. V.; Unwin, P. R. *The Journal of Physical Chemistry C* **2010**, *114*, 2633–2639.
- [2] Dumitrescu, I.; Edgeworth, J. P.; Unwin, P. R.; Macpherson, J. V. *Advanced Materials* **2009**, *21*, 3105–3109.
- [3] Clegg, G.; Fitton, J.; Harrison, P.; Treffry, A. *Progress in Biophysics and Molecular Biology* **1981**, *36*, 53–86.
- [4] Hutton, L.; Newton, M. E.; Unwin, P. R.; Macpherson, J. V. *Analytical Chemistry* **2009**, *81*, 1023–1032.
- [5] Hutton, L. A.; Newton, M. E.; Unwin, P. R.; Macpherson, J. V. *Analytical Chemistry* **2011**, *83*, 735–745.
- [6] Baer, C. D.; Stone, N. J.; Sweigart, D. A. *Analytical Chemistry* **1988**, *60*, 188–191.
- [7] Amemiya, S.; Nioradze, N.; Santhosh, P.; Deible, M. J. *Analytical Chemistry* **2011**, *83*, 5928–5935.
- [8] Ebejer, N.; Schnippering, M.; Colburn, A. W.; Edwards, M. A.; Unwin, P. R. *Analytical Chemistry* **2010**, *82*, 9141–9145.
- [9] Bard, A. J.; Faulkner, L. R. *Electrochemical Methods: Fundamentals and Applications*, 2nd ed.; John Wiley & Sons Inc.: New York, 2001.
- [10] Güell, A. G.; Ebejer, N.; Snowden, M. E.; Macpherson, J. V.; Unwin, P. R. *Journal of the American Chemical Society* **2012**, *134*, 7258–7261.

CHAPTER 3

TRACE VOLTAMMETRIC DETECTION OF SEROTONIN AT CARBON ELECTRODES

In this chapter, three different carbon electrodes are investigated as possible voltammetric sensors for the detection of serotonin. The electrochemical response of the commonly used glassy carbon (GC) electrode is compared to newer carbon materials, namely polycrystalline boron doped diamond (pBDD) and “pristine” carbon nanotube networks (CNTN). Cyclic voltammetry (CV) measurements on each of these electrodes demonstrate the significantly lower background currents of the pBDD and CNTN electrodes, leading to much lower limits of detection. The CNTN electrode exhibits an exceptional detection limit for serotonin of 10 nM, two orders of magnitude lower than GC. The susceptibility of the electrodes to fouling is also investigated, indicating that the pBDD electrode is much more resistant to fouling than the CNTN electrode, and that fouling can be significantly reduced by careful selection of the CV potential limits for the pBDD case.

3.1 INTRODUCTION

Carbon-based electrodes are widely used in voltammetric analysis for many reasons including low cost, ready availability, chemical stability, wide potential window and electrocatalytic activity for certain redox reactions. These electrodes are also biocompatible,^{1,2} making them more suitable, compared to metal electrodes, for

the study of biologically relevant redox systems and *in vivo* analysis. Of the carbon-based electrodes in use, glassy carbon (GC), polycrystalline boron doped diamond (pBDD) and carbon nanotubes (CNTs) are a group of electrode materials that present a wide range of characteristics that are interesting to compare. In essence, GC is a widely used and well-established material in electrochemistry, while CNT and pBDD electrodes, as newer materials, offer potential improvements in stability and improved sensitivity and detection limits.^{3,4}

As some neurotransmitters are voltammetrically active, electrochemistry represents a powerful technique that can be employed in the detection of these molecules.⁵⁻⁷ This chapter focuses on serotonin (5-hydroxytryptamine), a neurotransmitter which plays a role in a great number of essential biological processes.⁸ For example, it regulates mood and sleep, and serotonin receptors in the brain are now a target for many drugs designed to treat psychiatric disorders, such as depression.⁷ Serotonin also plays an important role in the gut, where it regulates intestinal movements and appetite.⁶

Two of the key issues in serotonin detection are achieving better detection limits and reduction of electrode fouling. Serotonin itself may adsorb on electrodes⁹ and, when oxidised,^{9,10} reactive species form^{10,11} which are also thought to adsorb strongly, impeding subsequent electron transfer.^{7,9} GC and carbon fibre electrodes have found common use in the electrochemical detection of serotonin,^{6,12,13} however, they both suffer from fouling during voltammetric analysis and a limited detection sensitivity.⁷

To enhance detection limits and minimise the effect of fouling, alternative carbon based electrodes have been considered. Notably, pBDD electrodes not only

exhibit a very wide potential window and resistance to corrosion,^{14–17} but also show reduced background currents and fouling compared to GC electrodes.⁶ The latter has often been attributed to the H-surface termination of as-grown pBDD electrodes.^{15,18} pBDD electrodes have thus been used in the detection of serotonin,^{6,14,19} and other neurotransmitters,^{20,21} showing a superior performance in terms of detection sensitivity, stability and resistance to fouling, compared to GC electrodes.^{15,22}

With their very high aspect ratio, good conductivity and low capacitance (when used in the pristine state),^{3,23} CNTs constitute a particularly interesting new electrode material. There has been an explosion of interest in CNTs for many different electrochemical applications, with reports of enhanced attributes and characteristics.³ Treating a surface with CNTs has also been proposed as a method to reduce fouling by biomolecule adsorption/decomposition.^{24–27} For serotonin detection, CNT-coated carbon fibre electrodes were found to result in higher signal/noise (S/N) ratios and reduced fouling compared to the bare electrode.⁷

Voltammetric studies with CNTs have tended to use harsh chemical (acid) treatments to purify the CNTs (which also results in chemical functionalisation) before deposition on an electrode surface. However, more recently, catalysed chemical vapour deposition (cCVD) has been used to produce “pristine” multiply interconnected networks of CNTs, directly on an insulating surface, which are clean and thus require no purification.²⁸ This approach not only allows the direct assessment of the electrochemical response of the CNTs, without any contribution from a substrate electrode, but the pristine nature and low surface

coverage of the CNTs results in low electrode capacitance, enabling unprecedented electrochemical detection limits using simple cyclic voltammetry (CV) analysis alone,^{29,30} although fast scan CV measurements using carbon fibre electrodes have yielded similarly low detection limits.^{31,32}

Herein, we use cCVD to produce CNT network (CNTN) electrodes and compare the sensitivity and fouling of these electrodes to both GC and pBDD electrodes for the detection of serotonin in aqueous buffered media. Compared to GC both the pBDD and CNTN electrodes show significantly better detection limits for serotonin, with the very low background currents of the CNTs enabling the detection of serotonin concentrations two orders of magnitude lower than for GC (limit of detection ~ 10 nM using CV) and more than one order of magnitude lower than pBDD. The pBDD electrodes show reduced fouling effects, compared to the CNTN electrodes, which can almost be eradicated by employment of appropriate CV cycling protocols. As the pBDD electrodes employed here are oxygen-functionalised, the data suggest that H-termination is not a prerequisite for achieving reduced fouling (surface adsorption) at pBDD electrodes.

3.2 CHARACTERISATION OF CNTs

Figure 3.1(a) shows a typical $2\ \mu\text{m} \times 2\ \mu\text{m}$ tapping mode AFM image of a cCVD grown CNT sample. The sample can be seen to comprise of a network of CNTs with each nanotube randomly oriented, making numerous contacts with neighbours. The Raman spectrum (Figure 3.1(b)) shows both the tangential modes derived from the in-plane Raman vibrations in graphite (G-band, $1500\text{-}1600\ \text{cm}^{-1}$) and

the disorder modes (D-band, 1300-1400 cm^{-1}). The shape and position of the G-band positively identifies the sample as containing single walled carbon nanotubes (SWNTs), in accordance with previous work.²⁷ While most of the SWNT heights are in the range 1-5 nm, larger height features are apparent (10-20 nm), indicating SWNTs that have bundled together or small diameter multi-walled CNTs. The cross-section taken from the AFM (Figure 3.1(a)) also indicates that the sample contains a few overlapping layers of CNTs. However this architecture is still very open (it does not have a high surface area) giving small background currents due to the low capacitance, as reported previously for similar samples.²⁷

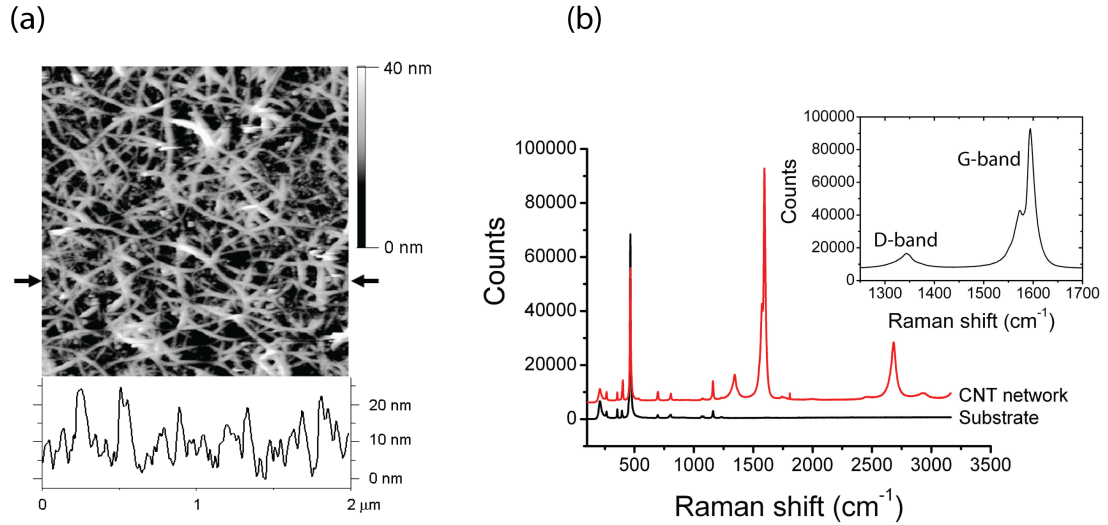


Figure 3.1: (a) AFM image, 2 $\mu\text{m} \times 2 \mu\text{m}$, of a CNTN on quartz. The arrows indicate where the line for the cross-section has been taken (shown below). (b) Micro-Raman spectrum of a CNT sample.

3.3 CYCLIC VOLTAMMETRY MEASUREMENTS

Figure 3.2 shows the three electrode setup used for cyclic voltammogram (CV) measurements at the CNTN electrode. A droplet of solution ($\sim 10 \mu\text{L}$, 3 mm diameter) was placed on the CNTN electrode close to the gold contact, and an Ag/AgCl wire reference electrode and Pt wire counter electrode were positioned within the droplet to complete the circuit. For the GC and pBDD disk electrodes, a saturated calomel electrode (SCE) reference electrode was used with Pt gauze as a counter electrode.

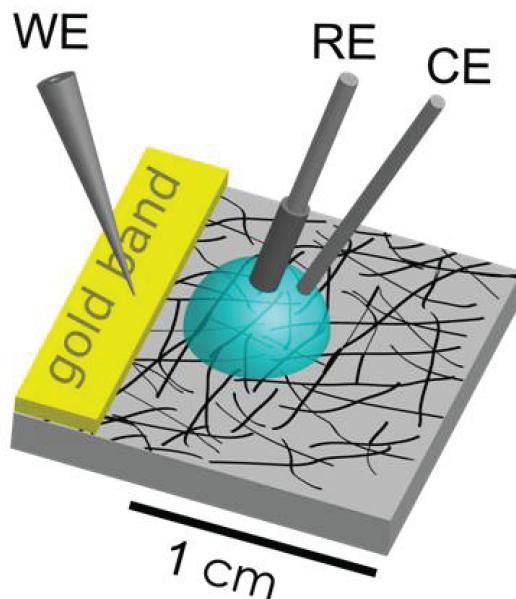


Figure 3.2: Schematic diagram of the CNTN electrode setup for electrochemical measurements.

3.3.1 BACKGROUND CURRENTS

CVs were recorded in the supporting electrolyte (0.1 M NaCl with 5 mM HEPES as a buffer) to determine the background currents for each type of carbon electrode. Figure 3.3 shows CVs recorded at 100 mV s^{-1} over the potential window appropriate for the electrochemical detection of serotonin (0.0 V to 0.7 V) with GC (dotted line), pBDD (dashed line) and CNTN (solid line). The currents have been normalised by the geometric area of each electrode and are shown as current density to allow comparison between the three electrodes, and the potential scales have been corrected to the SCE reference electrode.

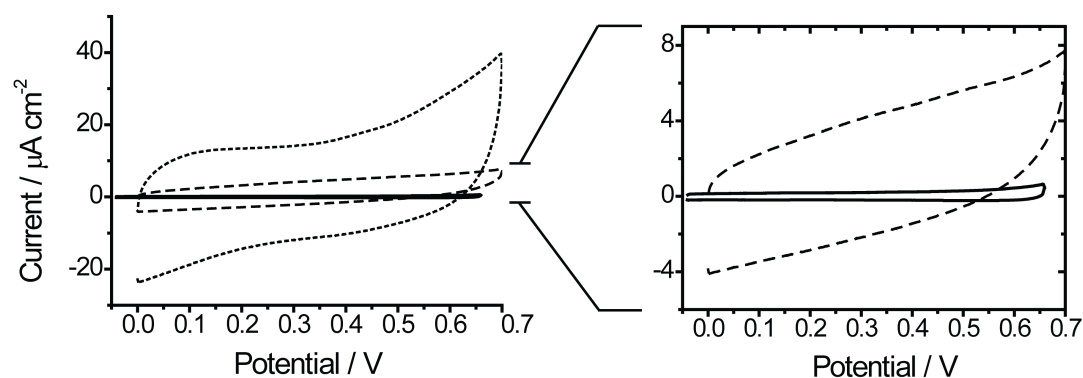


Figure 3.3: Left hand side: CVs recorded at 100 mV s^{-1} in 0.1 M NaCl and 5 mM HEPES buffer showing the background response for the GC (dotted line), pBDD (dashed line), and CNTN (solid line) electrode. The currents have been normalised by electrode area to facilitate comparison of the CV response. Right hand side: The current scale has been magnified in order to distinguish the low capacitive current of the CNTN electrode.

Clearly the CNTN electrode exhibits, by far, the lowest background currents. To quantify, for each electrode the background currents were measured at the

oxidation peak potential of serotonin (*vide infra*), to give $0.23 \mu\text{A cm}^{-2}$ at 0.38 V for the CNTN, $5.8 \mu\text{A cm}^{-2}$ at 0.53 V for pBDD and $18 \mu\text{A cm}^{-2}$ at 0.43 V for GC. From these values and taking into account the potential scan rate, ν , capacitances per unit area, C, can be calculated using $i_C = \nu C$,³³ where i_C is the capacitive current density contribution, to give $2.3 \mu\text{F cm}^{-2}$ (CNTN); $58 \mu\text{F cm}^{-2}$ (pBDD) and $180 \mu\text{F cm}^{-2}$ (GC). Thus, the CNTN electrode exhibits background contributions 25 times lower than the pBDD electrode and *ca.* 80 times lower than the GC electrode. As background current is a major factor in determining detection limits in CV, it is evident that it should be possible to detect much lower concentrations using the pBDD and CNTN electrodes than the GC electrode.

3.3.2 CV RESPONSES FOR SEROTONIN OXIDATION AND LIMITS OF DETECTION

CVs were recorded initially using relatively high serotonin concentrations (taking into account the detection sensitivity of each electrode, *vide infra*) to investigate the electro-oxidation characteristics of serotonin in 0.1 M NaCl and 5 mM HEPES buffer, for the three different types of carbon electrode. Figure 3.4 shows CVs recorded at a scan rate of 100 mV s^{-1} for the (a) GC electrode at 1 mM serotonin; (b) pBDD electrode at 100 μM serotonin and (c) CNTN electrode at 10 μM serotonin. For all three electrodes, in the potential range investigated, one peak is clearly observed, attributed to the oxidation of serotonin to p-quinone-o-imine.^{9,10} The process is clearly irreversible on this timescale, consistent with expectations that the oxidation product is unstable and

undergoes further chemical reaction.^{9,15} The electron transfer characteristics appear most sluggish on the pBDD electrode, as has also been observed by others,^{14,34} and is fastest on the CNTN electrode.

To investigate concentration detection limits, CVs were recorded at a scan rate of 100 mV s^{-1} for different serotonin concentrations, with the concentration range investigated dependent on the detection sensitivity of the electrode. For the CNTN electrode, the same electrode was used for a series of concentrations but the CVs were recorded from lowest (50 nM) to highest concentration (1 μM) to minimise fouling effects. The data was validated by recording one CV only on a fresh CNTN sample for the highest concentration employed and comparing the CV response. Figure 3.5 shows CVs (black solid line) recorded at 100 mV s^{-1} , for (ai) GC at 10 μM serotonin; (bi) pBDD at 1 μM serotonin and (ci) CNTN at 50 nM serotonin. These concentrations are towards the detection limit of each particular electrode. Also shown is the CV response recorded under the same potential scan conditions but in the background electrolyte solution only (dashed black line).

The background corrected peak current^{10,35} was measured and plotted against serotonin concentration, as a log-log plot to emphasis the full concentration range explored, (Fig. 4(aii)-(cii)), for all three electrodes. A clear linear trend is observed for all three cases, with gradients close to one, confirming a linear correlation of the peak current on concentration. For the electrodes, the limit of detection (defined by the $3S_b/m$ criteria, where m is the slope of the linear current signal-concentration calibration plot and S_b is the relative standard deviation of the amperometric signal of the blank for $n = 5$)¹³ is $\sim 2 \mu\text{M}$ for GC, $\sim 500 \text{ nM}$ for pBDD and $\sim 10 \text{ nM}$ for CNTN. To our knowledge, serotonin concentration detection limits of this

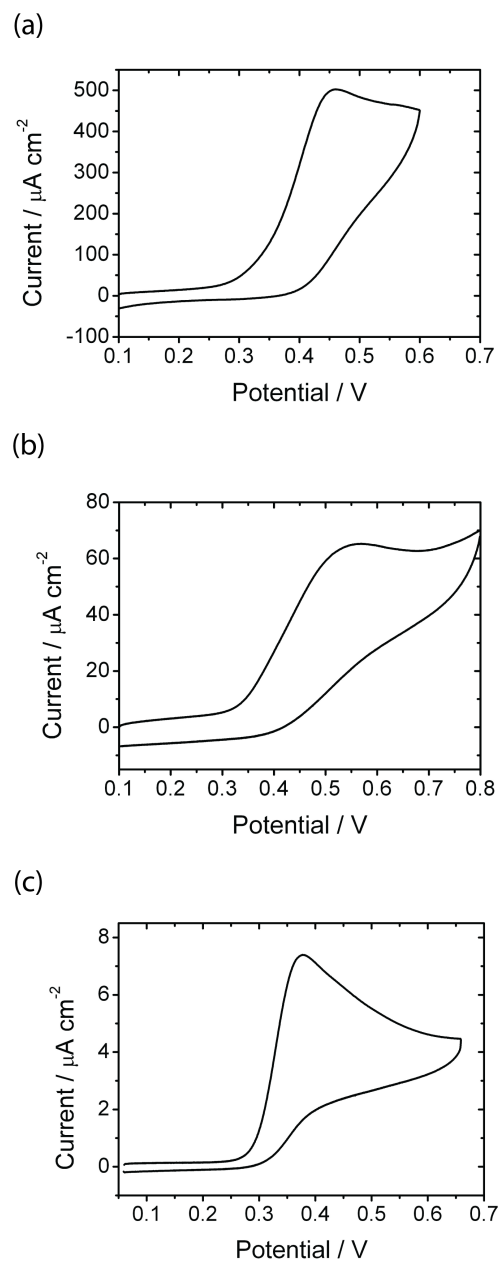


Figure 3.4: CVs recorded at 100 mV s^{-1} in 0.1 M NaCl and 5 mM HEPES buffer at (a) GC and 1 mM serotonin; (b) pBDD and 100 μM serotonin and (c) CNTN and 10 μM serotonin. The currents have been normalised with respect to electrode area.

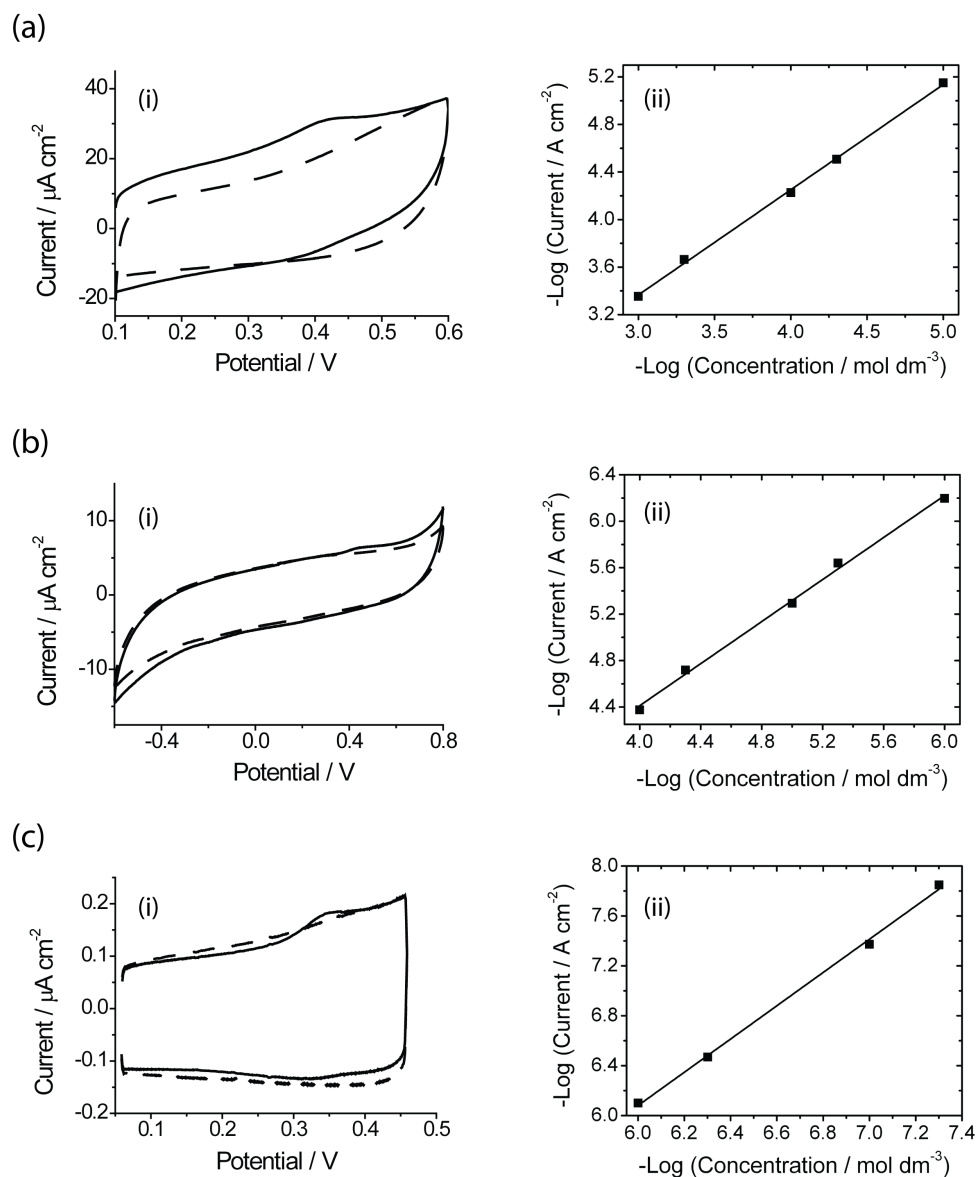


Figure 3.5: (i) CVs of background current (dashed line) and serotonin oxidation (solid line) at GC, pBDD and CNTN electrodes at concentrations close to the detection sensitivity of the electrode; in particular (a) GC electrode [10 μM]; (b) pBDD [1 μM]; (c) CNTN [50 nM]. (ii) Calibration plot for the three different electrodes showing the logarithm of the background corrected oxidation peak current versus logarithm of serotonin concentration. All the CVs were carried out at 100 mV s^{-1} and in 0.1 M NaCl and 5mM HEPES buffer.

order (CNTN electrode) with simple CV have never been reported at any kind of electrode.

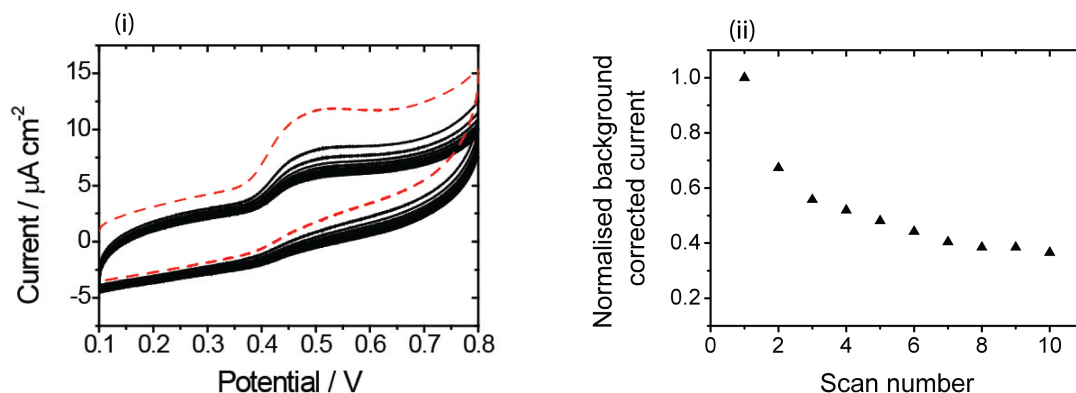
3.4 ASSESSMENT OF ELECTRODE FOULING EFFECTS

One of the major issues with the detection of neurotransmitters such as serotonin is fouling of the electrode surface.¹¹ Oxidation of serotonin produces hydroxylated products, dimers and other species that are thought to adsorb irreversibly onto electrodes^{7,9,11} (in addition to the reactant serotonin itself adsorbing) creating an “insulating” layer which blocks the electrode area and/or retards electron transfer. This problem is considered to be exacerbated the higher the serotonin concentration in solution.^{12,36} An investigation was thus carried out into electrode fouling on pBDD and CNTN electrodes as these were found to be the most promising for the sensitive detection of serotonin.

To assess the extent of electrode fouling, ten consecutive CVs, at a potential scan rate of 100 mV s^{-1} , were recorded for the pBDD and CNTN electrodes for $10 \text{ }\mu\text{M}$ concentration serotonin, for which both electrodes showed measurable oxidation peaks in supporting electrolyte. Representative CVs are shown in Figure 3.6. The background corrected peak current density was monitored as a function of CV cycle number and normalised with respect to the first CV recorded. These data are shown in graphical form below the respective CVs for (a) pBDD and (b) the CNTN electrode. The red dashed line indicates the first CV scan. For the pBDD electrode, CVs were recorded with the electrode placed in $5000 \text{ }\mu\text{L}$ of solution,

whilst for the CNTN electrode, solution was confined to a droplet of volume 10 μL .

(a)



(b)

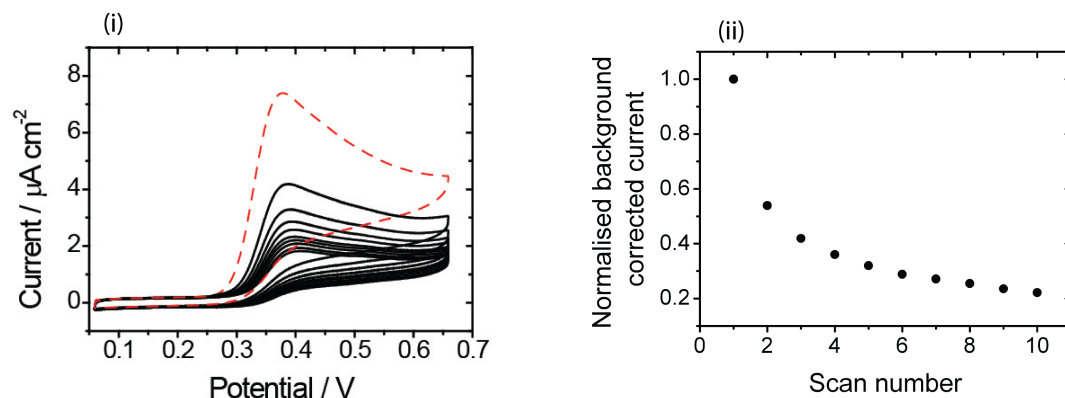


Figure 3.6: Ten repetitive CVs carried out at the (ai) pBDD electrode and (bi) CNTN electrode, at 100 mV s^{-1} and in 0.1 M NaCl and 5 mM HEPES buffer for a serotonin concentration of $10 \mu\text{M}$. The first scan is indicated by the red dashed line. The degree of fouling with subsequent scans is indicated by recording the background corrected peak current for serotonin oxidation as a function of CV scan number, as shown below in (aii) for pBDD and (bii) for CNTN.

It can be seen that the response of both electrodes deteriorates as the number of CV cycles increases, but the CNTN electrode appears to foul quicker. After ten CV

scans the background corrected peak current at the CNTN electrode decreased from the initial value by $\sim 90\%$ compared to $\sim 65\%$ for the pBDD electrode. To check that volume effects (*e.g.* product build-up) were not important some experiments were also recorded with a $10\ \mu\text{L}$ droplet, placed on the surface of the pBDD electrode, to mimic the experimental set-up for the CNTN electrode. Similar data were obtained irrespective of the solution volume.

Previous studies have shown that pBDD electrodes show reduced fouling compared to other carbon electrodes, an effect which had been attributed to the pBDD being used as-grown, *i.e.* H-terminated.^{14,18} However, our work (*vide infra*) suggests that H-termination may not be essential and is in agreement with the preliminary reports by Fujishima *et al.*¹⁵ who showed that electrochemically oxidising an H-terminated surface (hydrophobic) to create a more O-terminated one (hydrophilic), did not change the size of the peak current or peak potential for serotonin oxidation.

Figure 3.7 shows repetitive CVs recorded for the electrolysis of $10\ \mu\text{M}$ serotonin at a pBDD electrode recorded at $100\ \text{mV s}^{-1}$ by scanning from 0.0 to +0.8 V, back to -0.6 V and forward again. In the first CV scan (red dashed line), a redox couple response is just observable in the negative potential window, with current peaks seen at -0.2 and 0.0 V. This is most likely due to a redox-active quinone species which is an oxidation product of serotonin electrolysis.^{11,15} Interestingly the return peak at 0 V is significantly smaller than the peak at -0.2 V, a result which was also observed by Fujishima *et al.* on an electrochemically oxidised pBDD surface.¹⁵ In our studies the surface was made O-terminated by a strong acid clean at elevated temperatures prior to electrode fabrication.¹⁷

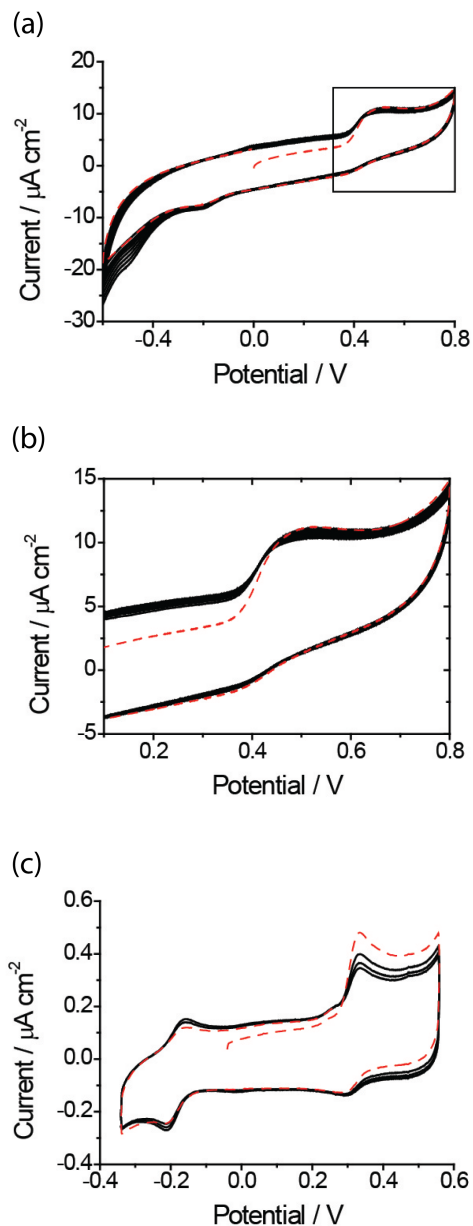


Figure 3.7: Repetitive CVs recorded at 100 mV s^{-1} in 0.1 M NaCl and 5 mM HEPES buffer for $10 \mu\text{M}$ serotonin electrolysis at (a) a pBDD electrode and (c) a CNTN electrode using an extended cathodic window, compared to Figure 3.4-3.6. The red dashed line indicates the first scan. (b) CV data from (a) plotted only in the anodic potential region to highlight minimised fouling of the electrode surface.

After repeated CV scans encompassing the extended cathodic potential limit it can be seen that the serotonin oxidation peak current density does not decrease appreciably compared to the case where the CV is only scanned in the positive potential window (Figure 3.7(a)). This is emphasised in Figure 3.7(b). Interestingly, Fujishima *et al.* showed that for an as-grown H-terminated pBDD surface, potential cycling over a similar potential range (same concentration and scan rate), did not minimise electrode fouling in the same way as seen here.¹⁵ Thus deliberate O-termination coupled with appropriate potential cycling appears to be beneficial for the clear voltammetric detection of serotonin at pBDD.

Figure 3.7(c) shows repetitive CVs recorded for the CNTN electrode for 500 nM serotonin at a potential scan speed of 100 mV s^{-1} but scanning out to -0.35 V. The peak for serotonin oxidation is again very clear, and in particular, the peaks attributed to the reduction and subsequent oxidation of the quinone/hydroquinone redox couple are very evident, at -0.21 and -0.16 V, respectively. Scanning further, to -0.6 V (as for Figure 3.7(a)), showed no change in the current density peak responses or peak potentials observed.

The three key differences between Figure 3.7(a) and (c) are: (1) the peak current density for serotonin oxidation decays at a greater rate with repeat cycling for the CNTN electrode than pBDD, (2) as the background currents are lower at the CNTN electrode the redox current density peaks for the serotonin oxidation by-product are clearly resolvable against the background (even when using a lower concentration of serotonin). There is also no significant difference in the magnitude of the reduction and oxidation current density peaks, which are (3)

much more closely spaced than on pBDD (indicating much faster electron transfer kinetics).

It should be noted that the CNTs used herein, prepared by cCVD and used as grown, are hydrophobic. Thus it would appear that surface wettability, which in the case of pBDD is controlled by surface termination, in conjunction with potential cycling plays a role in controlling the degree of surface blocking by adsorption processes. Additionally, we cannot rule out the effect of the more complex surface architecture of the CNTN electrode on surface adsorption, which could also contribute to fouling.

3.5 CONCLUSIONS

An assessment has been made of three different carbon-based electrodes, GC, pBDD and CNTNs, for the determination and quantification of a key neurotransmitter, serotonin (5-hydroxytryptamine). The pBDD electrode was \sim nm smooth and oxygen terminated (hydrophilic), whilst the CNTN was cleanly grown by cCVD (hydrophobic) on an insulating substrate and electrically contacted. A major outcome of the work was that using CV analysis, the CNTN electrodes were found to exhibit background currents *ca.* two orders of magnitude smaller than the GC electrode and *ca.* twenty times smaller than pBDD, as a consequence of their “pristine” low capacitance state and low surface coverage. This led to serotonin detection limits, using simple CV analysis, of 2 μ M for GC, 500 nM for pBDD and 10 nM for the CNT network electrode.

Surface blocking effects were investigated for the two most sensitive electrodes,

i.e. pBDD and the CNTN. From observation of the current decay during repeated CV scans, pBDD was found to be less sensitive to fouling than the CNTN electrode. Fouling was primarily attributed to electrolysis products formed during serotonin oxidation. By scanning to suitable negative potentials a redox active by-product could be electrochemically detected; a response significantly clearer with the CNTN electrode due to the reduced background currents. Fouling of the pBDD electrode was significantly reduced by CV cycling to cathodic potentials, however, the effect was less pronounced for the CNTN electrode, most probably due to differences in surface wettability and the complex surface architecture of the electrode.

3.6 REFERENCES

- [1] Jacobs, C. B.; Peairs, M. J.; Venton, B. J. *Analytica Chimica Acta* **2010**, *662*, 105–127.
- [2] McCreery, R. L. *Chemical Reviews* **2008**, *108*, 2646–2687.
- [3] Dumitrescu, I.; Unwin, P. R.; Macpherson, J. V. *Chemical Communications* **2009**, 6886–6901.
- [4] Compton, R. G.; Foord, J. S.; Marken, F. *Electroanalysis* **2003**, *15*, 1349–1363.
- [5] Yao, H.; Li, S.; Tang, Y.; Chen, Y.; Chen, Y.; Lin, X. *Electrochimica Acta* **2009**, *54*, 4607–4612.
- [6] Sarada, B. V.; Rao, T. N.; Tryk, D. A.; Fujishima, A. *Chemistry Letters* **1999**, *28*, 1213–1214.
- [7] Swamy, B. E. K.; Venton, B. J. *Analyst* **2007**, *132*, 876–884.
- [8] Cooper, J. R.; Bloom, F. E.; Ruth, R. H. *The Biochemical Basis of Neuropharmacology*; Oxford University Press, 2003.
- [9] Jackson, B. P.; Dietz, S. M.; Wightman, R. M. *Analytical Chemistry* **1995**, *67*, 1115–1120.
- [10] Wrona, M. Z.; Lemordant, D.; Lin, L.; Blank, C. L.; Dryhurst, G. *Journal of Medicinal Chemistry* **1986**, *29*, 499–505.
- [11] Wrona, M. Z.; Dryhurst, G. *The Journal of Organic Chemistry* **1989**, *54*, 2718–2721.
- [12] Anastassiou, C. A.; Patel, B. A.; Arundell, M.; Yeoman, M. S.; Parker, K. H.; O'Hare, D. *Analytical Chemistry* **2006**, *78*, 6990–6998.

- [13] Njagi, J.; Ball, M.; Best, M.; Wallace, K. N.; Andreescu, S. *Analytical Chemistry* **2010**, *82*, 1822–1830.
- [14] Patel, B. A.; Bian, X.; Quaiserova-Mocko, V.; Galligan, J. J.; Swain, G. M. *Analyst* **2007**, *132*, 41–47.
- [15] Sarada, B. V.; Rao, T. N.; Tryk, D. A.; Fujishima, A. *Analytical Chemistry* **2000**, *72*, 1632–1638.
- [16] Pleskov, Y. V. *Russian Journal of Electrochemistry* **2002**, *38*, 1275–1291.
- [17] Hutton, L.; Newton, M. E.; Unwin, P. R.; Macpherson, J. V. *Analytical Chemistry* **2009**, *81*, 1023–1032.
- [18] Xu, J.; Chen, Q.; Swain, G. M. *Analytical Chemistry* **1998**, *70*, 3146–3154.
- [19] Patel, B. A. *Analyst* **2008**, *133*, 516–524.
- [20] Muna, G. W.; Quaiserova-Mocko, V.; Swain, G. M. *Analytical Chemistry* **2005**, *77*, 6542–6548.
- [21] Park, J.; Show, Y.; Quaiserova, V.; Galligan, J. J.; Fink, G. D.; Swain, G. M. *Journal of Electroanalytical Chemistry* **2005**, *583*, 56–68.
- [22] Popa, E.; Notsu, H.; Miwa, T.; Tryk, D. A.; Fujishima, A. *Electrochemical and Solid-State Letters* **1999**, *2*, 49–51.
- [23] Dumitrescu, I.; Unwin, P. R.; Wilson, N. R.; Macpherson, J. V. *Analytical Chemistry* **2008**, *80*, 3598–3605.
- [24] Lin, Y.; Yantasee, W.; Wang, J. *Frontiers in Bioscience* **2005**, *10*, 492–505.
- [25] Wang, J.; Li, M.; Shi, Z.; Li, N.; Gu, Z. *Electrochimica Acta* **2001**, *47*, 651–657.
- [26] Musameh, M.; Wang, J.; Merkoci, A.; Lin, Y. *Electrochemistry Communications* **2002**, *4*, 743–746.
- [27] Dumitrescu, I.; Edgeworth, J. P.; Unwin, P. R.; Macpherson, J. V. *Advanced*

- Materials* **2009**, *21*, 3105–3109.
- [28] Edgeworth, J. P.; Wilson, N. R.; Macpherson, J. V. *Small* **2007**, *3*, 860–870.
- [29] Dumitrescu, I.; Unwin, P. R.; Macpherson, J. V. *Electrochemistry Communications* **2009**, *11*, 2081–2084.
- [30] Bertoncello, P.; Edgeworth, J. P.; Macpherson, J. V.; Unwin, P. R. *Journal of the American Chemical Society* **2007**, *129*, 10982–10983.
- [31] Hashemi, P.; Dankoski, E. C.; Petrovic, J.; Keithley, R. B.; Wightman, R. M. *Analytical Chemistry* **2009**, *81*, 9462–9471.
- [32] Hashemi, P.; Dankoski, E. C.; Lama, R.; Wood, K. M.; Takmakov, P.; Wightman, R. M. *Proceedings of the National Academy of Sciences* **2012**, *109*, 11510–11515.
- [33] Bard, A. J.; Faulkner, L. R. *Electrochemical Methods: Fundamentals and Applications*; Wiley, New York, 1980; pp 316–369.
- [34] Cvacka, J.; Quaiserova, V.; Park, J.; Show, Y.; Muck, A.; Swain, G. M. *Analytical Chemistry* **2003**, *75*, 2678–2687.
- [35] Wang, Z.-H.; Liang, Q.-L.; Wang, Y.-M.; Luo, G.-A. *Journal of Electroanalytical Chemistry* **2003**, *540*, 129–134.
- [36] Manica, D. P.; Mitsumori, Y.; Ewing, A. G. *Analytical Chemistry* **2003**, *75*, 4572–4577.

CHAPTER 4

SCANNING ELECTROCHEMICAL CELL MICROSCOPY OF SINGLE WALLED CARBON NANOTUBES: QUANTITATIVE ANALYSIS OF HETEROGENEOUS ELECTRON TRANSFER RATES

This chapter reports the use of a novel, high resolution electrochemical imaging technique to investigate the electron transfer characteristics of individual single-walled carbon nanotubes (SWNTs). Scanning electrochemical cell microscopy (SECCM) employs a dual channel probe as a mobile electrochemical cell, enabling the electrochemical response of isolated regions of an individual SWNT to be examined. Two different redox mediators (ferrocenylmethyltrimethylammonium and serotonin) are studied herein. These studies demonstrate high electrochemical activity along the length of the SWNT. A finite element method simulation is developed to analyse the data, revealing fast rates of heterogeneous electron transfer (HET) for the oxidation of ferrocenylmethyltrimethylammonium, with values for the standard rate constant, k^0 , equal to $2.5 \pm 1.2 \text{ cm s}^{-1}$. High electrochemical activity is even observed for complex redox processes such as the oxidation of serotonin. In this case, serotonin oxidation products cause fouling of the SWNTs, however, at low concentrations, fouling is minimised and reproducible currents are observed for the trace and retrace scans over the same area.

4.1 INTRODUCTION

The exceptional electronic, structural and mechanical properties of carbon nanotubes (CNTs)¹ have led to their use in a variety of applications, including electronics,² electrocatalysis,³ sensing^{4,5} and energy storage.⁶ Their low cost, high conductivity, and chemical and mechanical stability¹ make them extremely attractive for electrochemical applications, and the ability to functionalise CNTs with simple chemical groups broadens their potential uses.⁷ Furthermore, their nanometre size greatly enhances the rate of mass transport in an electrochemical setup, enabling the study of extremely fast kinetic processes such as those presented herein.⁸ CNTs are commonly produced in bulk, via arc discharge or similar methods,⁹ however, with newer techniques such as catalytic chemical vapour deposition (cCVD),¹⁰ CNTs can be grown in a number of different geometries, including individual aligned nanotubes,⁸ 2D networks¹¹ and 3D forests,¹² further increasing their versatility.

As a result of their numerous electrochemical applications, there has been considerable interest in understanding heterogeneous electron transfer (HET) at CNTs,^{13–16} however there are a number of challenges associated with probing this process, and consequently there is still some uncertainty about the kinetics of electron transfer on CNTs. Many studies have used a coating of nanotubes applied to an electroactive substrate (for example, by drop casting), to determine the effect of the nanotubes on the electrochemical response.^{17,18} However, since the support is itself electroactive, it is difficult to distinguish the electrochemical activities of the two materials individually. Due to the difficulty in isolating the

electrochemical response of the CNTs, the activity of other sp^2 carbon materials such as highly oriented pyrolytic graphite (HOPG) have been compared to that of the CNTs, and these results have led to the conclusion that edge-plane-like defects and open nanotube ends are responsible for the electroactivity of the CNTs, with the sidewalls relatively (or completely) inactive.^{14,17,18}

Alternative methodologies have been employed to study the electroactivity of CNTs in isolation. Pristine single-walled carbon nanotubes (SWNTs) have been grown on insulating substrates via CVD,^{19,20} to ensure the electrochemical response can be decoupled from that of the supporting material.²¹ Studies on individual SWNTs,⁸ 2D networks^{16,22} and 3D forests²³ with a range of redox mediators, have shown fast HET kinetics, indicating that the sidewalls are highly active, however, most studies present data averaged over many SWNTs, and very few electrochemical studies have been carried out on individual SWNTs.

Recently, the Warwick group has reported the use of scanning electrochemical cell microscopy (SECCM) as an electrochemical imaging technique to investigate the kinetics of HET on a variety of substrates, with very high spatial resolution.^{24–26} Using this high resolution technique, it is possible to probe the HET kinetics along the length of individual SWNTs to assess the electroactivity of the sidewalls. SECCM employs a theta pipette, which contains two barrels separated by a glass septum, each filled with the redox species of interest in the supporting electrolyte, and a quasi-reference counter electrode (QRCE). When the meniscus protruding from the end of the pipette is in contact with the substrate, it forms a mobile electrochemical cell which can be scanned across the sample. In this study, the individual SWNTs are connected as a working electrode in the system by means

of an evaporated palladium contact, so that their electrochemical response can be recorded. With the mobile electrochemical cell setup of SECCM, only a small section of the SWNT is probed at a time, before moving to a new area. This is particularly advantageous in the investigation of the electrochemical response of complex mediators such as serotonin, which can foul electrode materials during electrochemical oxidation as discussed in Chapter 3.^{27–29}

To fully characterise the HET kinetics of individual nanotubes, flow-aligned SWNTs were grown via CVD onto insulating substrates (SiO_2). The density of nanotubes was optimised to ensure SWNTs were adequately spaced for easy imaging of each nanotube individually. Previous work has demonstrated that SWNTs grown in this way contain very few defects,¹¹ and therefore this configuration is optimal for exploring the intrinsic HET rates along the sidewalls of CNTs. SECCM was used to investigate the electrochemical response of defined regions of the pristine SWNTs to different redox mediators, enabling rates of HET at the sidewalls to be assessed in isolation. To quantitatively analyse this response, a finite element method (FEM) model was developed, allowing the measured electrochemical currents to be converted into HET kinetic rate constants.

4.2 THEORY AND SIMULATIONS

To quantitatively analyse the electrochemical response of the SWNTs, FEM simulations were performed, to correlate the observed electrochemical response with HET rate constants for the SWNTs. The geometry of the pipette was

approximated by a circular based cone of radius 200 nm, determined from scanning electron microscopy images of the pipettes used, and the SWNT was represented as a rectangle of width w with the length defined by the edges of the meniscus. The SWNT was oriented parallel to the septum of the pipette, to match the configuration of the experimental setup as can be seen in Figure 4.1. To improve computational efficiency, half of the pipette was modelled by symmetry, with the plane of symmetry perpendicular to the pipette septum.

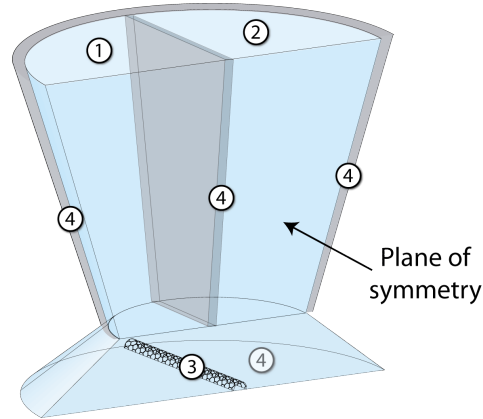


Figure 4.1: 3D FEM simulation domain showing the position and orientation of the SWNT with respect to the pipette.

Furthermore, the focus of the simulations was only the terminus of the pipette and meniscus. Consequently, the potential applied to planes 1 and 2 in the simulation domain was smaller than at the electrodes in the experiments. To match the simulated results to the ion current measured experimentally, simulations were carried out at a range of effective potential bias values and meniscus heights (which cannot be measured experimentally), generating working planes for the AC and

DC currents, such as those shown in Figure 4.2.

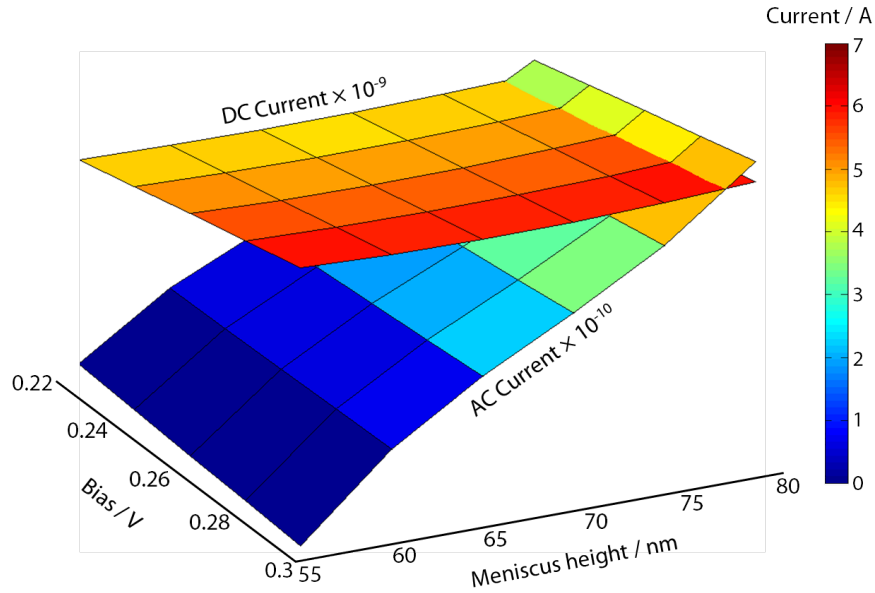


Figure 4.2: Working planes of AC and DC currents *vs* meniscus height and effective bias.

The experimental AC and DC values were matched to the working planes to obtain values for the meniscus height and effective bias, which were then used as inputs for the subsequent modelling. Typical values of 60-90 nm meniscus height and 0.2-0.3 V bias were found, with parameters calculated for each different SECCM image acquired.

The initial calibration step was performed in the absence of a working electrode reaction by solving the steady-state Nernst-Planck equation subject to the boundary conditions listed in Table 4.1:

$$\nabla (-D_i C_i - z_i u_i F c_i \nabla V) = 0 \quad (4.1)$$

with

$$\sum_i z_i c_i = 0 \quad (4.2)$$

where D_i , c_i , z_i and u_i are the diffusion coefficient, concentration, charge and mobility of species, i , respectively. F is the Faraday constant and V is the electric field due to the potential bias applied between the two QRCEs.

Table 4.1: Summary of the boundary conditions used for the simulation of the electrochemical current at the SWNT surface during SECCM imaging.

| Label in Figure 4.1 | Boundary | Boundary Type | Equation |
|------------------------|---|----------------------------|--|
| 1 | Pipette barrel 1 | Potential Concentration | $V = \text{Bias}$ $c_i = c^*$ |
| 2 | Pipette barrel 2 | Potential Concentration | $V = 0$ $c_i = c^*$ |
| 3 | SWNT surface | Flux | $D \frac{\partial c}{\partial z} = k_f(c^* - c) - k_b c$ |
| 4 | Pipette septum, pipette walls and substrate | No Flux | $D \frac{\partial c_i}{\partial z} = 0$ |

The potential field was determined using ion mobilities and diffusion coefficients obtained from the literature for 0.5 mM ferrocenylmethyltrimethylammonium (FcTMA^+) as the PF_6^- salt, with 50 mM NaCl in 50 mM phosphate buffer solution (PBS) at pH 7.2. This potential field was then implemented in the second step of the simulation, in which the current response of the SWNT was determined using Butler-Volmer kinetics (see section 1.3), reasonably assuming a

transfer coefficient $\alpha = 0.5$ for this fast process. Simulations were run at a range of k^0 values to find the rate constant corresponding to the observed current as detailed in section 2.7.3. Since the solution contained an excess of supporting electrolyte compared to the electroactive species, the changes in migration current due to the redox reactions were assumed to be negligible, and therefore not included so as to increase computational efficiency.

Figure 4.3(a) shows a typical potential field calculated in the first step of the simulation. As can be seen, the potential difference at the SWNT/solution interface is well approximated by the difference between the potentials of the two QRCEs, as noted in section 2.5.1. Figure 4.3(b) shows a typical FcTMA^+ concentration profile as it is oxidised at the SWNT surface in step 2 of the calculation (with $k^0 = 1 \text{ cm s}^{-1}$ and applied potential, $E = 0.5 \text{ V}$), with a low concentration at the SWNT surface as it is consumed. The effect of the potential field on the concentration profile is evident, as the charged species migrate towards the oppositely charged QRCE.

4.3 SWNT GROWTH AND CHARACTERISATION

4.3.1 SILVER DEPOSITION PROCEDURE

Flow aligned SWNTs were grown onto inert Si/SiO₂ wafers as described in section 2.2.1. After growth, a macroscopic electrical connection to the SWNTs was made via the evaporation of a palladium contact (60-90 nm) with a chromium adhesive layer (2 nm). Since the SWNTs cannot be visualised with optical microscopy, a

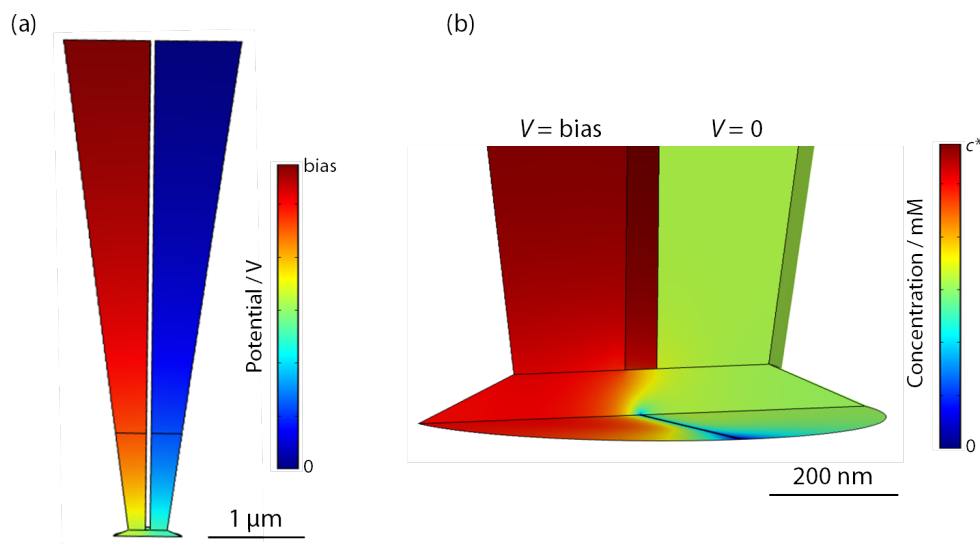


Figure 4.3: (a) FEM simulation of the potential field due to the application of a bias between the two QRCEs. (b) Typical simulated concentration profile of FcTMA^+ as it is consumed at the SWNT ($k^0 = 1 \text{ cm s}^{-1}$, $E = 0.5 \text{ V}$).

procedure to mark the nanotubes was developed to enable location of the SWNTs in the SECCM setup. A tapered single channel pipette (tip diameter $\sim 100 \mu\text{m}$) was filled with 10 mM silver nitrate and 50 mM potassium nitrate, and silver wire was inserted. This was connected as a QRCE, with the sample connected as the working electrode (at ground), and a potential of -0.3 V applied to the QRCE. The amperometric response of the SWNT electrode was recorded as the capillary was brought into contact with the sample and then scanned laterally across the surface using a micropositioner (Figure 4.4(a)). As the capillary passed over an SWNT, a change in current was observed due to silver deposition, and these deposits could be visualised under the optical microscope, identifying the position of each SWNT (Figure 4.4(b)).

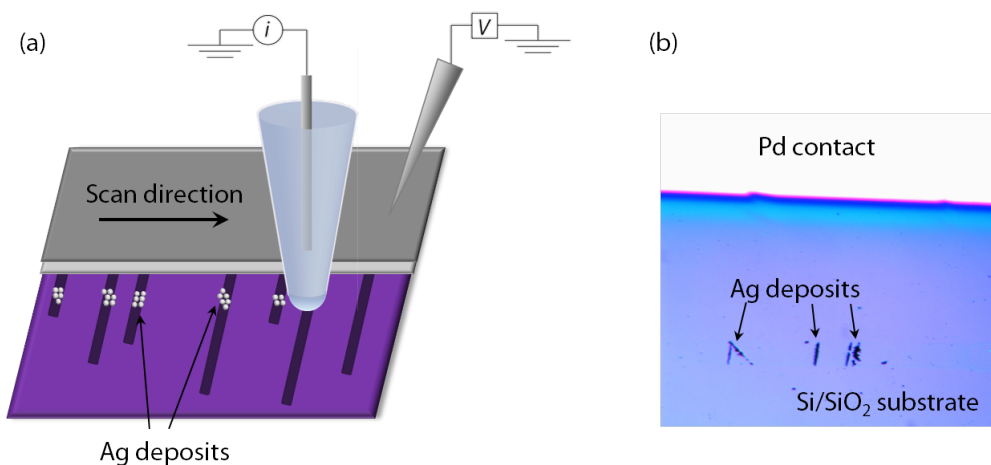


Figure 4.4: (a) Schematic illustrating the Ag deposition procedure for marking SWNTs to allow visualisation under the optical microscope. (b) Optical microscopy image of Ag deposits on flow-aligned SWNTs.

4.3.2 AFM ANALYSIS

The SWNTs were characterised with tapping mode AFM prior to use and were found to have an average height of 1-3 nm consistent with previously reported values for single walled nanotubes.³⁰ Peak heights from the AFM images were extracted for 20 lines of each image to give an average height for each SWNT. Figure 4.5 shows histograms of these heights for three different SWNTs which display a similar range of values. The AFM images also demonstrated the linearity of the SWNTs.

4.3.3 ELECTRICAL CHARACTERISATION

In order to characterise the electrical properties of the SWNTs, conductance current-voltage curves were recorded using a mercury hemisphere electrode,

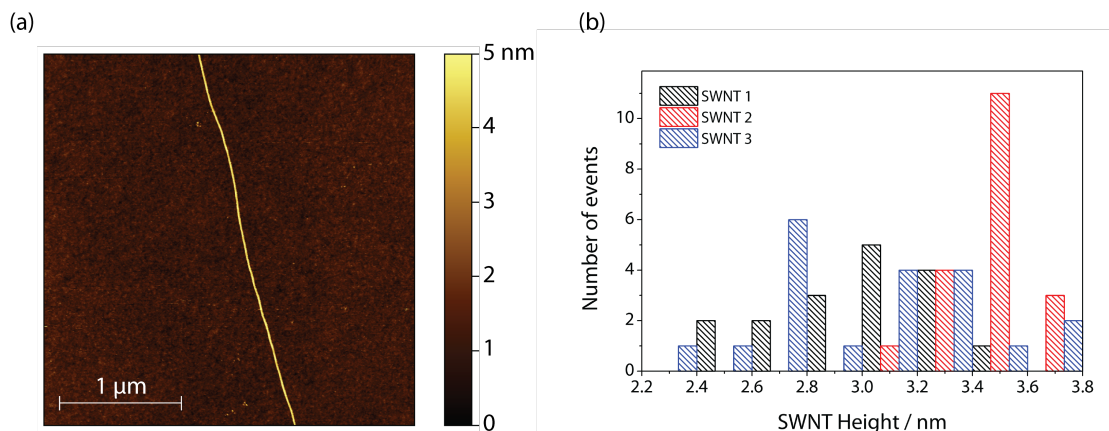


Figure 4.5: (a) Typical AFM image of an individual aligned SWNT. (b) Histogram of heights of three separate SWNTs.

deposited at the tip of a 25 μm diameter Pt ultramicroelectrode (UME). To achieve this, the UME was connected as a working electrode held in a solution of 10 mM mercury nitrate and 50 mM nitric acid with an Ag/AgCl reference electrode, whilst a potential of -0.15 V was applied. When the diffusion limited current increased to $\frac{\pi}{2}$ times the initial value, a hemisphere could be reasonably assumed to have formed, as confirmed by optical microscopy. The UME/mercury hemisphere (connected as the reference electrode) was then brought into contact with the sample (connected as the working electrode) whilst a potential of -0.5 V was applied to it. The UME was scanned laterally across the surface until a change in current was observed, corresponding to the mercury hemisphere coming into contact with a SWNT. Once in contact, the potential between the UME/mercury hemisphere electrode and the substrate was scanned between +3 and -3 V vs ground, producing a current-voltage curve.

As described in section 1.8.3, SWNTs exhibit either metallic or semiconducting behaviour dependent on their structure, and these different characteristic

behaviours give rise to different current-voltage responses. Figure 4.6 shows a current-voltage curve for an individual SWNT. The symmetrical response in the positive and negative potential regions indicates that this is a metallic SWNT.³¹ For semiconducting SWNTs, the response is asymmetrical, with lower currents observed in the positive potential region, since SWNTs are p-type semiconductors.³¹ For this study, we chose to work with only SWNTs that demonstrated metallic behaviour, to eliminate any variations in observed electroactivity between metallic and semiconducting SWNTs. Analysis of the current-voltage curves for these SWNTs yielded resistance values of 5.3 ± 4.4 M Ω , at a distance of ~ 1 mm from the Pd contact, consistent with reported values for pristine SWNTs containing relatively few defects.³¹

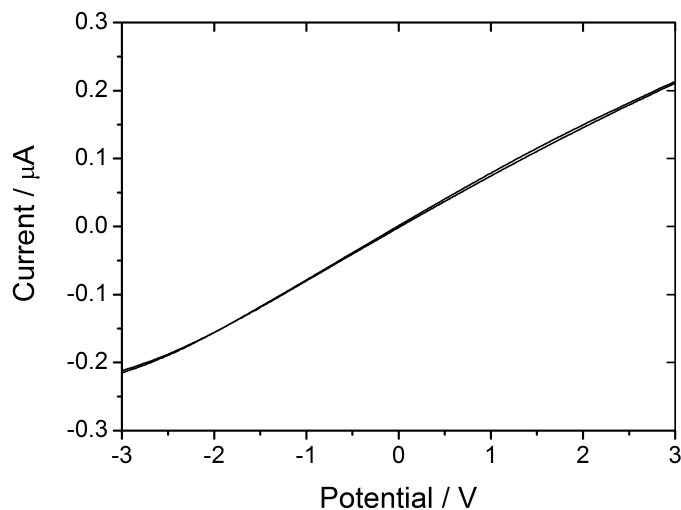


Figure 4.6: Typical current-voltage curve recorded on a metallic SWNT using a mercury hemisphere electrode.

4.4 DETERMINATION OF FORMAL POTENTIALS

The formal potential, E^0 , for the oxidation of $\text{FcTMA}^{+/2+}$ was determined by CV measurements on a freshly cleaved HOPG sample. The CV measurements displayed consistent, reversible behaviour in different areas of the HOPG surface, giving an E^0 value of +0.30 V and a difference in quartile potentials of 53 mV (Figure 4.7(a)). Whilst the oxidation of FcTMA^+ is reversible, serotonin oxidation is a complex and irreversible process. CV measurements of serotonin oxidation shows that the current does not reach a steady state value as the electrode fouls due to oxidation products adsorbing to the surface, causing a decrease in the current as can be seen in Figure 4.7(b). However, an approximation of the formal potential can be made from these measurements, allowing appropriate potentials to be chosen for SECCM imaging using the two different mediators, although kinetic analysis of the serotonin data is not possible without an accurate, known E^0 value.

4.5 REDOX ACTIVITY OF SWNTs FOR THE OXIDATION OF FcTMA^+

CVs were recorded on individual SWNTs which showed consistent responses at different positions along the length of the nanotube. Figure 4.8 shows a typical CV with the potentials used for SECCM imaging indicated.

The SECCM imaging procedure and instrumentation is described fully in section

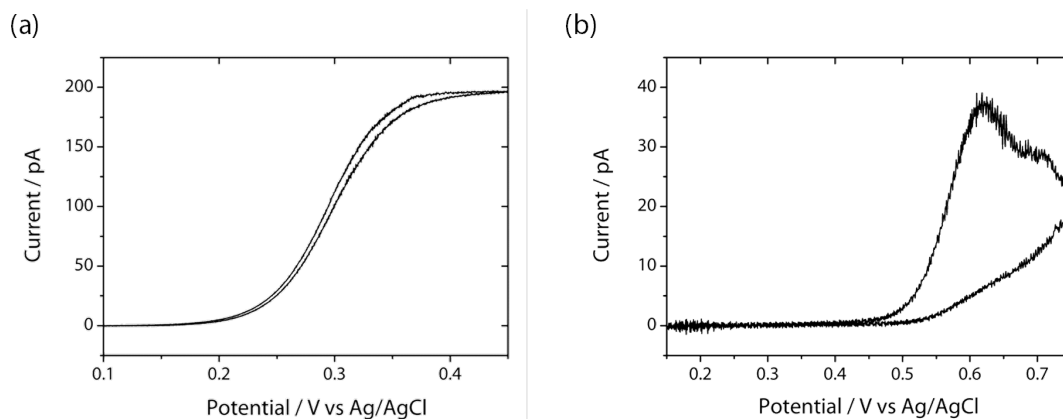


Figure 4.7: Cyclic voltammograms recorded on freshly cleaved HOPG at 100 mV s^{-1} with 0.5 V bias applied between the QRCEs for (a) the oxidation of 0.5 mM FcTMA⁺ with 50 mM NaCl in PBS with a $2 \mu\text{m}$ pipette and (b) the oxidation of 5 mM serotonin with 100 mM NaCl and 10 mM HEPES with a 400 nm pipette.

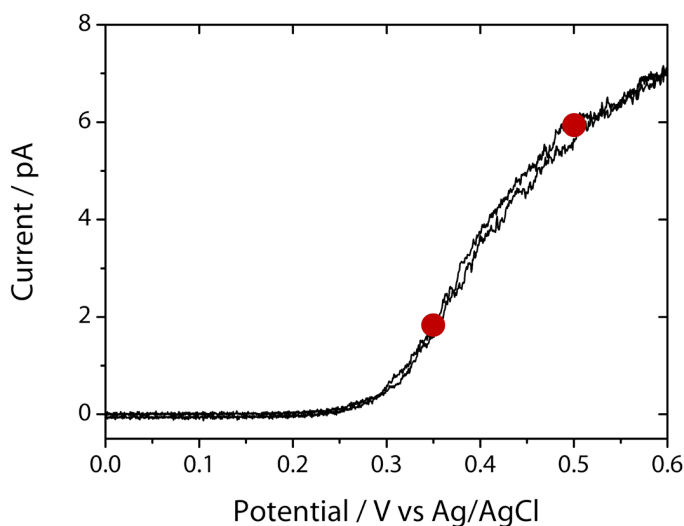


Figure 4.8: Typical cyclic voltammogram recorded at an individual SWNT for the oxidation of 0.5 mM FcTMA⁺ with 50 mM NaCl in PBS at 100 mV s^{-1} . The red dots indicate the applied potentials used for SECCM imaging.

2.5.1. The samples were oriented with the SWNTs perpendicular to the x -direction of the scan, so that the tip scanned across the SWNT on each line of the scan.

Imaging was carried out in the region between the palladium contact and the silver deposits to avoid any influence of the silver nanoparticles on the electrochemical response.

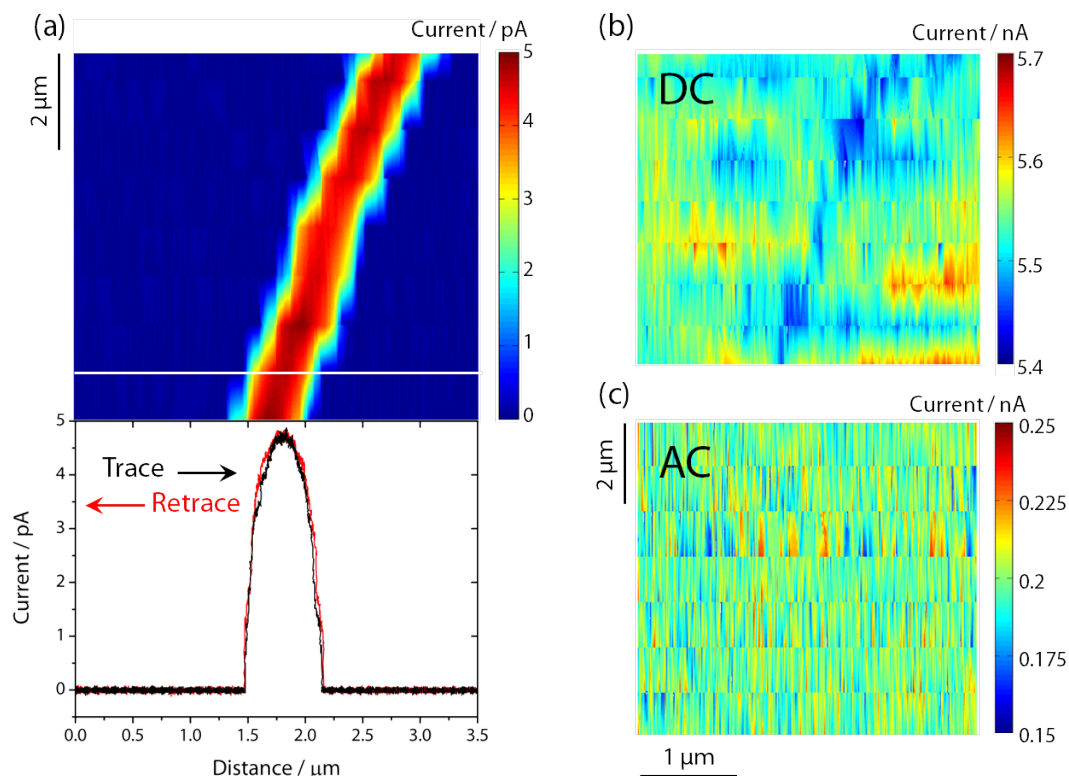


Figure 4.9: (a) SECCM map for the oxidation of 0.5 mM FcTMA⁺ at the SWNT surface ($\eta = 0.2$ V) in the forward scan direction with corresponding trace and retrace line profiles for the region indicated. (b) Conductance current recorded between the two QRCEs in the forward scan direction. (c) AC component of the conductance current recorded between the two QRCEs in the forward scan direction.

Each sample was connected as a working electrode and used to drive the oxidation of FcTMA⁺ at the SWNT surface. Figure 4.9(a) shows a typical SECCM image for the oxidation of 0.5 mM FcTMA⁺ at an overpotential ($\eta = E - E^0$, where E is the applied potential) of 0.2 V in the forward scan directions. In each line of

the scan, the length of SWNT in contact with solution was approximately 700 nm (corresponding to the size of the meniscus) and each line was spaced 800 nm apart so that there was a small region of SWNT between the scanned areas, to prevent the previous line scan influencing the following one in any way. The image in Figure 4.9(a) was produced by smoothing together the line scans in the y -direction.

The SECCM image produced clearly demonstrates that the SWNT is uniformly active along its length, in contrast to the widely held assumption that only SWNT ends and defect sites are responsible for electron transfer. Previous studies, upon which this assumption is based, have compared the electroactivity of basal plane and edge plane pyrolytic graphite electrodes to a basal plane pyrolytic graphite electrode modified with carbon nanotubes.^{14,17,18} Since the edge plane and CNT modified electrodes showed similar behaviour, with much faster kinetics than the bare basal plane electrode, the authors concluded that the edge plane like defects in the CNTs must be responsible for the observed activity. However, recent work has demonstrated that in fact basal plane HOPG exhibits high electrochemical activity when freshly cleaved, suggesting that this relationship is not accurate.^{25,32,33} Furthermore, the bulk produced CNTs used are likely to contain many more defects than the pristine cCVD-grown SWNTs used in this study, further complicating the analysis and conclusions that may be drawn about sidewall activity. Recent investigations on CVD-grown CNTs in which the activity of sidewalls and nanotube open ends (which contain many defects) have been studied independently, have shown comparable electrochemistry on the two regions, suggesting that the view of CNT sidewalls as inactive is no longer accurate.^{23,34}

Analysis of the variation within the SECCM maps provides further evidence for the role of the sidewall in electron transfer. Comparing the highest and lowest peak currents in Figure 4.9(a) yields a difference of approximately 8 %. Assuming that defects alone were responsible for electron transfer, this variation would require a defect density of approximately one defect every 50 nm. Raman analysis on cCVD-grown SWNTs has demonstrated their high quality,¹¹ and investigations into defect concentrations have reported values of one defect every few micrometres, indicating that this estimated defect density is physically unrealistic.³⁵ Moreover, simulations have been performed comparing the case where defects alone are assumed to be responsible for electron transfer to where the entire sidewall is active, which demonstrate that even very high defect concentrations, with unfeasibly high kinetic rate constants, cannot reproduce the observed electrochemical currents and that the entire sidewall must be considered active.²²

The line profile in Figure 4.9(a) shows good agreement between the trace and retrace line scans for the region indicated, demonstrating the consistency of the measurements and indicating that no fouling of the SWNT is occurring. The curved shape of the profile after initial contact with the SWNT is made, is due to the increasing length of nanotube in contact with the meniscus as the tip moves into alignment with the nanotube. The peak current corresponds to the position where the septum of the pipette is directly above the SWNT. Figure 4.9(b) shows the conductance current recorded between the two QRCEs throughout the scan. There is very little variation in the magnitude of the current, indicating that the size and shape of the meniscus remain constant, which is important for accurate kinetic analysis of the observed SECCM currents. Finally figure 4.9(c) shows the

AC component of the conductance current, which is used as the feedback parameter during scanning. There is clearly very little variation over the duration of the scan, indicating that excellent feedback is maintained throughout.

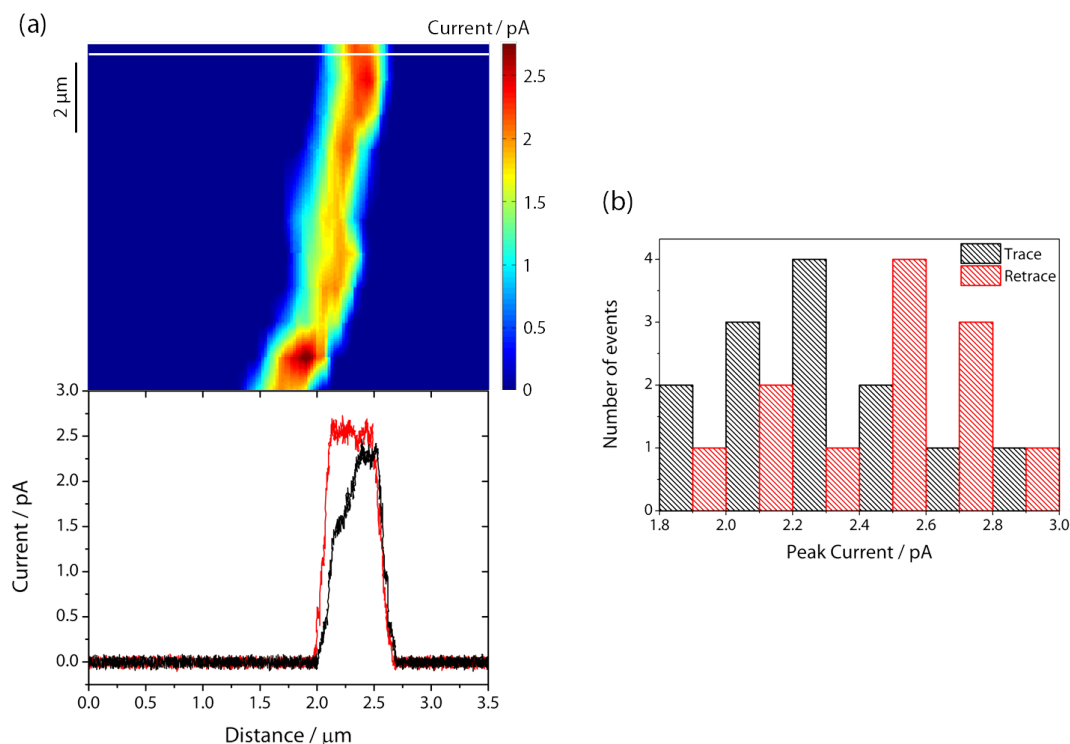


Figure 4.10: (a) SECCM map for the oxidation of 0.5 mM FcTMA⁺ at the SWNT surface ($\eta = 0.05$ V) in the forward direction with corresponding trace and retrace line scans for the region indicated. (b) Histogram of peak currents from each line of the trace and retrace SECCM images.

SECCM imaging was carried out at a range of different applied overpotentials, to ensure the kinetic response was consistent, independent of the driving force for FcTMA⁺ oxidation. Figure 4.10(a) shows an SECCM image for $\eta = 0.05$ V with trace and retrace line profiles for the region indicated. High activity is still observed along the length of the SWNT, although there is more slightly variation

in the response compared to Figure 4.9(a).

Figure 4.10(b) illustrates the range of peak currents for each line of the trace and retrace SECCM images. This indicates that although there is more variation than for the full driving case, the range of observed currents is relatively narrow, and there continues to be good agreement between trace and retrace currents.

4.6 QUANTITATIVE ANALYSIS OF HET KINETICS

In order to correlate the observed electrochemical currents with the standard HET rate constant, k^0 , a FEM model was developed as described in the previous section. SECCM images for FcTMA⁺ oxidation were recorded at a range of different overpotentials, from 0 to 0.3 V. For $\eta > 0.1$ V, the reaction was considered to be fully driven and hence k^0 values could not accurately be determined for these data. However, for all SECCM scans with $\eta \leq 0.1$ V, the electrochemical currents were determined for a range of simulated k^0 values, producing working curves of substrate current vs. $\log(k^0)$ (Figure 4.11(a)). For rate constants above 100 cm s⁻¹, the concentration of FcTMA⁺ is effectively zero and so this boundary condition was used to simulate the current for high k^0 values. From the working curves, the k^0 values corresponding to the observed electrochemical currents could be determined for each SWNT. As can be seen in Figure 4.11(b), the extracted k^0 values are relatively consistent along the length of the SWNT imaged. Between different SWNTs, k^0 values ranged from 1.1 cm s⁻¹ to 5.7 cm s⁻¹ with an average value of 2.5 ± 1.2 cm s⁻¹. Previous studies have reported k^0 values of > 4.6 cm s⁻¹,³⁶ 4 ± 2 cm s⁻¹,⁸ and 2 ± 1 cm s⁻¹³⁷ for

the oxidation of FcTMA^+ at individual SWNTs, giving confidence in our assigned k^0 values, which are in good agreement.

Whilst these values closely match previous work, there are a number of assumptions made during the simulation process which could lead to errors in the reported values. The approximation of the SWNT as a 2-dimensional band may lead to errors in the simulated electrochemical current since the surface area in contact with the solution may be slightly inaccurate, and the different geometry may have an impact on the mass transport to the nanotube. Whilst these factors would certainly impact the magnitude of the determined rate constants, the values would still be within the same order of magnitude and therefore comparable with previous work. The geometry of the meniscus is assumed to be constant throughout, despite slight variations in the measured conductance current. However, these variations are small and are highly unlikely to have any measurable impact on the determined rate constants.

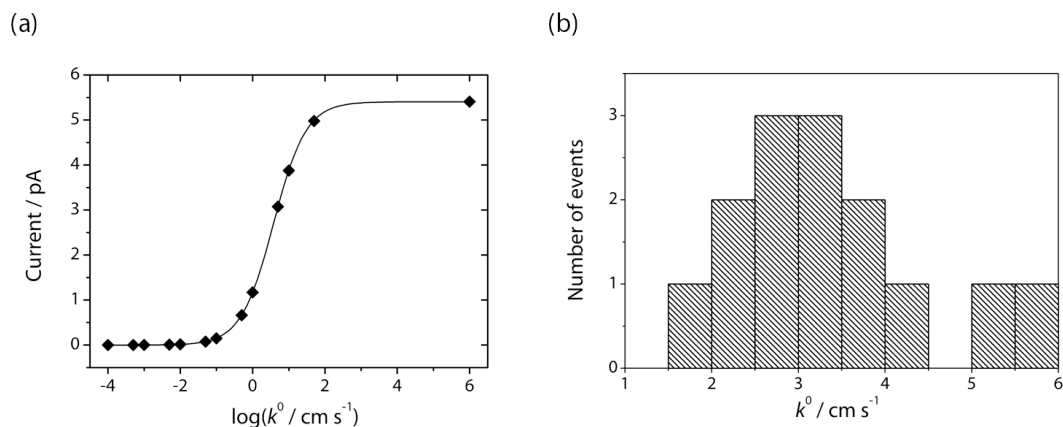


Figure 4.11: (a) Working curve of electrochemical current vs standard rate constant, k^0 , for the oxidation of FcTMA^+ with $\eta = 0.05$ V. (b) Histogram of k^0 values for an individual SWNT with $\eta = 0.05$ V.

Line profiles were also simulated by varying the position of the SWNT in relation to the centre of the pipette in the simulations. Figure 4.12 clearly shows good agreement between experiment and simulation for the data shown in Figure 4.9(a) (with $k^0 = 1.8 \text{ cm s}^{-1}$), indicating that modelling the SWNT as a fully active band electrode is justified in explaining the experimental data. Previous simulations have shown that modelling only point defects on the SWNT cannot feasibly account for the observed electrochemical activity, providing further evidence that the SWNT sidewall is fully active.²²

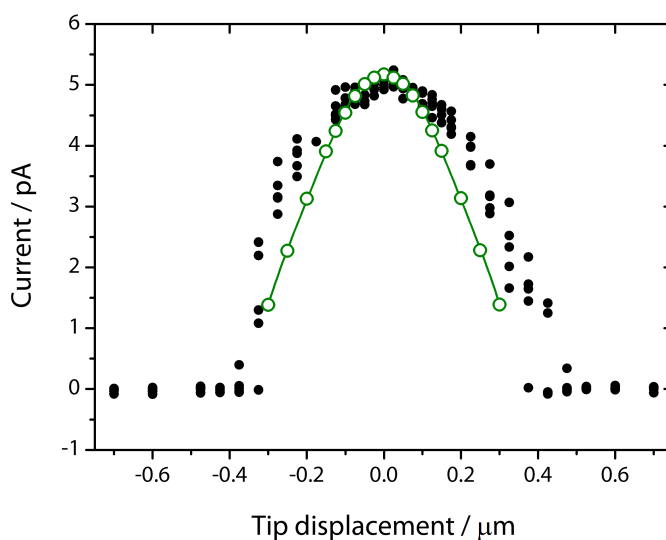


Figure 4.12: Comparison of experimental and simulated ($k^0 = 1.8 \text{ cm s}^{-1}$, $\eta = 0.2 \text{ V}$) data for the electrochemical currents as the SECCM pipette is scanned laterally across the SWNT.

4.7 ELECTROCHEMICAL RESPONSE OF SWNTs TO COMPLEX REDOX MEDIATORS

To investigate the response of SWNTs to more multi-step reactions, SECCM maps were recorded for the oxidation of serotonin (in 0.1 M NaCl and 10 mM HEPES). Once again, uniform activity along the length of the nanotube is observed, however there is significant difference in the shape of the line profiles recorded as the meniscus is scanned over the SWNT, compared to those for FcTMA^+ oxidation (Figure 4.13(a)). There is a large asymmetry in the peak due to fouling of the SWNT from adsorption of the oxidation products. Thus, as soon as the meniscus makes contact with the SWNT and serotonin oxidation begins, there is an initial surge in current, but as the meniscus continues its movement, the current decays even though the area of the SWNT exposed to the solution increases. This can be attributed to blocking of the SWNT by oxidation products, known to occur for serotonin oxidation (see Chapter 3).^{28,38,39} This effect is further evident in the reverse scan, where the current for the oxidation of serotonin is greatly diminished. By reducing the concentration of serotonin from 2 mM to 5 μM , this effect is mitigated and the line profile becomes symmetrical, and the forward and reverse maps are extremely consistent, indicating that fouling of the SWNT has been minimised; see Figure 4.13(a). This profile and associated image shows that the oxidation of serotonin occurs uniformly and readily over the SWNT.

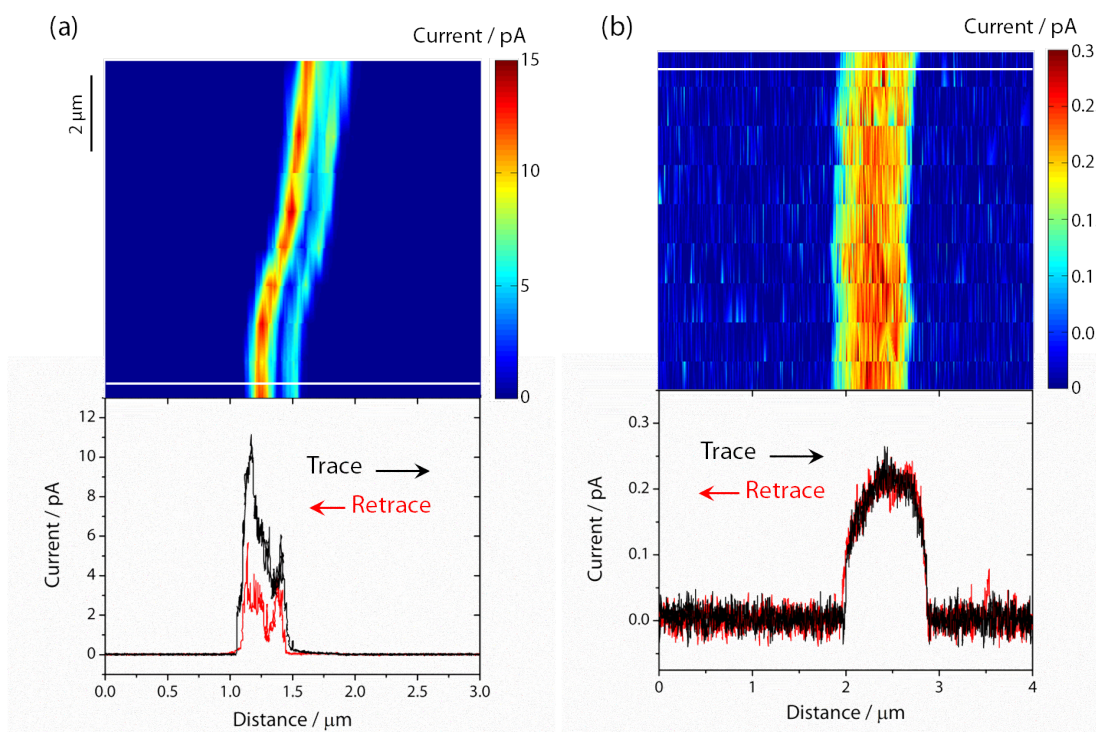


Figure 4.13: SECCM maps for the oxidation of (a) 5 mM and (b) 5 μ M serotonin at the SWNT surface ($E = 0.55$ V) in the forward direction with corresponding trace and retrace line scans for the region indicated.

4.8 CONCLUSIONS

Individual pristine flow-aligned individual SWNTs have been imaged with scanning electrochemical cell microscopy using two different redox mediators. With the format developed, the electrical character of each SWNT can be determined and the structure elucidated by techniques such as AFM. Electrochemical maps showed clear electrochemical activity along the length of the SWNT, providing evidence that HET occurs at the nanotube sidewalls, and defects and open ends are not solely responsible for the electrochemical activity of SWNTs. A FEM model was

developed in order to extract values of the standard rate constant, k^0 , for the oxidation of FcTMA^+ at different SWNTs. Kinetic analysis for the $\text{FcTMA}^{+/2+}$ couple, revealed fast HET rates, with average k^0 values of $2.5 \pm 1.2 \text{ cm s}^{-1}$, which were consistent along the length of each SWNT and in agreement with previous studies.

Complex, multi-stage reactions have also been shown to exhibit uniform activity along the length of the SWNTs, indicating that the density of defects is not governing the electrochemical response of the nanotube. Fouling was observed during the oxidation of serotonin, significantly reducing the electrochemical current on the reverse scan, and causing an asymmetry in the line profiles. However, reducing the concentration of mediator to the μM level, which is more physiologically relevant, virtually eliminated any fouling effects in the two line scans recorded and gave reproducible signals for both trace and retrace scans.

Overall, SECCM has great potential as a technique to probe the electrochemical activity of substrates on the nanometre scale, and coupled with FEM simulations, enables kinetic analysis of fast HET processes, which would be inaccessible with conventional electrochemical techniques.

4.9 REFERENCES

- [1] Valcárcel, M.; Cardenas, S.; Simonet, B. M. *Analytical Chemistry* **2007**, *79*, 4788–4797.
- [2] Avouris, P.; Chen, Z.; Perebeinos, V. *Nature Nanotechnology* **2007**, *2*, 605–615.
- [3] Vairavapandian, D.; Vichchulada, P.; Lay, M. D. *Analytica Chimica Acta* **2008**, *626*, 119–129.
- [4] Gooding, J. J. *Electrochimica Acta* **2005**, *50*, 3049–3060.
- [5] Wang, J. *Electroanalysis* **2005**, *17*, 7–14.
- [6] Dai, L.; Chang, D. W.; Baek, J.-B.; Lu, W. *Small* **2012**, *8*, 1130–1166.
- [7] Sun, Y.-P.; Fu, K.; Lin, Y.; Huang, W. *Accounts of Chemical Research* **2002**, *35*, 1096–1104.
- [8] Heller, I.; Kong, J.; Heering, H. A.; Williams, K. A.; Lemay, S. G.; Dekker, C. *Nano Letters* **2005**, *5*, 137–142.
- [9] Ebbesen, T. W.; Ajayan, P. M. *Nature* **1992**, *358*, 220–222.
- [10] Kong, J.; Cassell, A. M.; Dai, H. *Chemical Physics Letters* **1998**, *292*, 567–574.
- [11] Edgeworth, J. P.; Wilson, N. R.; Macpherson, J. V. *Small* **2007**, *3*, 860–870.
- [12] Burt, D. P.; Whyte, W. M.; Weaver, J. M. R.; Glidle, A.; Edgeworth, J. P.; Macpherson, J. V.; Dobson, P. S. *The Journal of Physical Chemistry C* **2009**, *113*, 15133–15139.
- [13] Pumera, M.; Iwai, H. *The Journal of Physical Chemistry C* **2009**, *113*, 4401–4405.

-
- [14] Banks, C. E.; Davies, T. J.; Wildgoose, G. G.; Compton, R. G. *Chemical Communications* **2005**, 829–841.
- [15] Chou, A.; Bocking, T.; Singh, N. K.; Gooding, J. J. *Chemical Communications* **2005**, 842–844.
- [16] Dumitrescu, I.; Unwin, P. R.; Wilson, N. R.; Macpherson, J. V. *Analytical Chemistry* **2008**, *80*, 3598–3605.
- [17] Banks, C. E.; Moore, R. R.; Davies, T. J.; Compton, R. G. *Chemical Communications* **2004**, 1804–1805.
- [18] Holloway, A. F.; Toghill, K.; Wildgoose, G. G.; Compton, R. G.; Ward, M. A. H.; Tobias, G.; Llewellyn, S. A.; Ballesteros, B.; Green, M. L. H.; Crossley, A. *The Journal of Physical Chemistry C* **2008**, *112*, 10389–10397.
- [19] Liu, B.; Ren, W.; Gao, L.; Li, S.; Pei, S.; Liu, C.; Jiang, C.; Cheng, H.-M. *Journal of the American Chemical Society* **2009**, *131*, 2082–2083.
- [20] Dai, H. *Surface Science* **2002**, *500*, 218–241.
- [21] Dumitrescu, I.; Edgeworth, J. P.; Unwin, P. R.; Macpherson, J. V. *Advanced Materials* **2009**, *21*, 3105–3109.
- [22] Güell, A. G.; Ebejer, N.; Snowden, M. E.; McKelvey, K.; Macpherson, J. V.; Unwin, P. R. *Proceedings of the National Academy of Sciences* **2012**, *109*, 11487–11492.
- [23] Miller, T. S.; Ebejer, N.; Güell, A. G.; Macpherson, J. V.; Unwin, P. R. *Chemical Communications* **2012**, *48*, 7435–7437.
- [24] Patten, H. V.; Meadows, K. E.; Hutton, L. A.; Iacobini, J. G.; Battistel, D.; McKelvey, K.; Colburn, A. W.; Newton, M. E.; Macpherson, J. V.; Unwin, P. R. *Angewandte Chemie International Edition* **2012**, *51*, 7002–7006.
- [25] Lai, S. C. S.; Patel, A. N.; McKelvey, K.; Unwin, P. R. *Angewandte Chemie*

- International Edition* **2012**, *51*, 5405–5408.
- [26] Güell, A. G.; Ebejer, N.; Snowden, M. E.; Macpherson, J. V.; Unwin, P. R. *Journal of the American Chemical Society* **2012**, *134*, 7258–7261.
- [27] Patten, H. V.; Lai, S. C. S.; Macpherson, J. V.; Unwin, P. R. *Analytical Chemistry* **2012**, *84*, 5427–5432.
- [28] Swamy, B. E. K.; Venton, B. J. *Analyst* **2007**, *132*, 876–884.
- [29] Güell, A. G.; Meadows, K. E.; Unwin, P. R.; Macpherson, J. V. *Physical Chemistry Chemical Physics* **2010**, *12*, 10108–10114.
- [30] Youn, S. K.; Yazdani, N.; Patscheider, J.; Park, H. G. *RSC Adv.* **2013**, *3*, 1434–1441.
- [31] Wilson, N. R.; Cobden, D. H.; Macpherson, J. V. *The Journal of Physical Chemistry B* **2002**, *106*, 13102–13105.
- [32] Patel, A. N.; Collignon, M. G.; OConnell, M. A.; Hung, W. O. Y.; McKelvey, K.; Macpherson, J. V.; Unwin, P. R. *Journal of the American Chemical Society* **2012**, *134*, 20117–20130.
- [33] Patel, A. N.; McKelvey, K.; Unwin, P. R. *Journal of the American Chemical Society* **2012**, *134*, 20246–20249.
- [34] Gong, K.; Chakrabarti, S.; Dai, L. *Angewandte Chemie International Edition* **2008**, *47*, 5446–5450.
- [35] Fan, Y.; Goldsmith, B. R.; Collins, P. G. *Nature Materials* **2005**, *4*, 906–911.
- [36] Kim, J.; Xiong, H.; Hofmann, M.; Kong, J.; Amemiya, S. *Analytical Chemistry* **2010**, *82*, 1605–1607.
- [37] Dudin, P. V.; Snowden, M. E.; Macpherson, J. V.; Unwin, P. R. *ACS Nano* **2011**, *5*, 10017–10025.
- [38] Wrona, M. Z.; Dryhurst, G. *The Journal of Organic Chemistry* **1989**, *54*,

2718–2721.

- [39] Jackson, B. P.; Dietz, S. M.; Wightman, R. M. *Analytical Chemistry* **1995**, *67*, 1115–1120.

CHAPTER 5

INVESTIGATION OF HETEROGENEOUS ELECTRON TRANSFER KINETICS AT POLYCRYSTALLINE BORON DOPED DIAMOND ELECTRODES USING FINITE ELEMENT METHOD SIMULATIONS

Determination of the rates of heterogeneous electron transfer at an electrode is an important but challenging problem. In this chapter, high resolution electrochemical maps of a heterogeneous surface, pBDD, are obtained using intermittent contact scanning electrochemical microscopy. With this technique it is possible to resolve the electrochemical response of each facet of the polycrystalline material individually, enabling correlation of structural differences with observed electroactivity. A finite element model is developed to determine the rate constants corresponding to the observed electrochemical currents, in order to compare HET kinetics at facets with different dopant densities. Coupling these results with local capacitance measurements reveals that HET kinetics correlate with the local density of states of the material.

5.1 INTRODUCTION

Understanding the kinetics of heterogeneous electron transfer (HET) is of widespread interest and has been investigated extensively with a variety of different electrochemical techniques.¹⁻⁴ The kinetic rates of electrochemical

processes can be influenced by a multitude of factors associated with the redox couple, solvent, experimental geometry and the electrode itself, making accurate analysis challenging.⁵⁻⁸ The development of micrometer sized electrodes has overcome some of these limitations by reducing the uncompensated resistive potential drop (IR drop) and increasing mass transport rates, allowing faster electrode kinetics to be studied.⁹⁻¹¹

In scanning electrochemical microscopy (SECM), mass transfer can be further enhanced by reducing the electrode-substrate separation. When operating in substrate generation tip collection (SG-TC) mode, the close proximity of substrate and electrode gives rise to extremely high rates of turnover of the electroactive species between the tip and the substrate, enabling the study of fast HET processes.^{12,13}

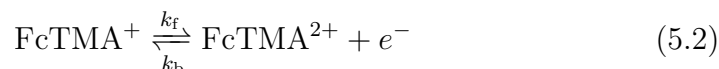
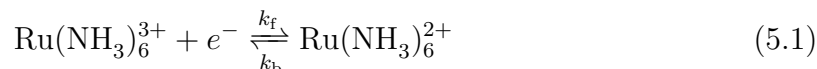
Since the data collected experimentally in SECM is the tip electrode current, a model is usually required in order to extract kinetic rates. Due to the complexity of the experimental system, a numerical approach is often necessary, and the most common methods for solving the differential equations governing mass transport in the system are the finite different method (FDM)¹⁴ and finite element method (FEM).¹⁵ In both of these approaches, solutions to the mass transport equations are calculated at discrete locations, approximating the continuous diffusion field. As discussed in section 1.9, the FDM is less computationally expensive, but has limitations in terms of the experimental geometries that can be accurately simulated. In this chapter, the finite element method is used, implemented within COMSOL Multiphysics, to model the kinetics of HET at a polycrystalline boron doped diamond (pBDD) electrode.

The experimental data presented were obtained using a variant of SECM, intermittent contact-SECM (IC-SECM).¹⁶ In this technique, the UME is oscillated perpendicular to the substrate by applying an AC perturbation to the piezoelectric positioner controlling its movement. As the UME is brought into contact with the substrate, a damping in the oscillation is detected, which is used as a feedback mechanism to maintain a constant tip-substrate separation. Since conventional SECM has no positional feedback mechanism to ensure a constant distance between the UME and substrate, it is extremely difficult to decouple the effects of surface topography and activity on the electrochemical current. Even for a substrate such as pBDD, which has a surface roughness of only 1-2 nm, if the sample and UME are not aligned parallel to one another, the resulting SECM image will show a variation in electrochemical current due to the tilt of the sample, complicating the analysis of kinetic rates. IC-SECM eliminates this complication, in addition to maintaining a small tip-substrate separation, which enhances the resolution of the technique. In this way, the HET rates of individual grains can be accurately extracted from the electrochemical data by means of the FEM model presented herein.

5.2 THEORY AND SIMULATIONS

To quantify IC-SECM tip currents, FEM modelling was employed to simulate the tip current response as a function of the standard rate constant, k^0 , using Butler-Volmer kinetics for the pBDD electrode.¹⁷ For these simulations, the following

one-electron redox processes were considered:



where k_f and k_b are the forward (reduction) and backward (oxidation) rate constants respectively. For each redox species studied, the following steady-state diffusion equation was solved:

$$D_i \left(\frac{\partial^2 c_i}{\partial r^2} + \frac{1}{r} \frac{\partial c_i}{\partial r} + \frac{\partial^2 c_i}{\partial z^2} \right) = 0 \quad (5.3)$$

where c_i (mol cm³) and D_i (cm² s⁻¹) represent the concentration and diffusion coefficient of species i (ruthenium hexaamine ($\text{Ru}(\text{NH}_3)_6^{3+}$) or ferrocenylmethyltrimethylammonium (FcTMA^+)) and r and z are the coordinates in the directions radial and normal to the centre of the Pt UME surface. In order to simplify the model, D_i was assumed to be identical for both oxidation states of the redox couple, to allow each simulation to be formulated with only one species.

The FEM model was used to determine the current response at the Pt UME in the SG-TC mode by solving the diffusion equation on the interior of the domain depicted in Figure 5.1 subject to the boundary conditions of the system, which are summarised in Table 5.1.

In Table 5.1, \underline{n} represents the inward-pointing unit normal vector and c^* represents the concentration of the electroactive species in bulk solution. The simulations

Table 5.1: Summary of the boundary conditions used for the simulation of the Pt UME tip current in SG-TC mode.

| Label in Figure 5.1 | Boundary Type | Coordinates | Equation |
|---------------------|------------------|---|---|
| 1 | Axis of Symmetry | $r = 0$ $0 \leq z \leq h$ | $0 = \nabla c \cdot \underline{n}$ |
| 2 | Pt UME Tip | $0 \leq r \leq a$ $z = d$ | $c = c^*$ |
| 3 | UME Glass Sheath | $a \leq r \leq a \times \text{RG}$ $z = d$ and $r = a \times \text{RG}$ $d \leq z \leq h$ | $0 = \nabla c \cdot \underline{n}$ |
| 4 | pBDD Substrate | $0 \leq r \leq l$ $z = 0$ | $D \frac{\partial c}{\partial z} = k_b(c^* - c) - k_f c$ (for $\text{Ru}(\text{NH}_3)_6^{3+}$) $D \frac{\partial c}{\partial z} = k_f(c^* - c) - k_b c$ (for FcTMA^+) |
| 5 | Bulk Solution | $a \times \text{RG} \leq r \leq l$ $z = h$ and $r = l$ $0 \leq z \leq h$ | $c = c^*$ |

were carried out with $\text{RG} = 10$, $l = 200 \text{ } \mu\text{m}$ and $h = 200 \text{ } \mu\text{m}$. The height, h , effectively defines the Nernst diffusion layer,¹⁸ which is typically of the order of several hundred micrometers. Changing h over this range (150 - 300 μm) had a negligible influence on the tip current, because this is essentially governed by d and the substrate kinetics. By setting l to 200 μm , it was reasonable to apply a boundary condition that resulted in planar diffusion at this position.

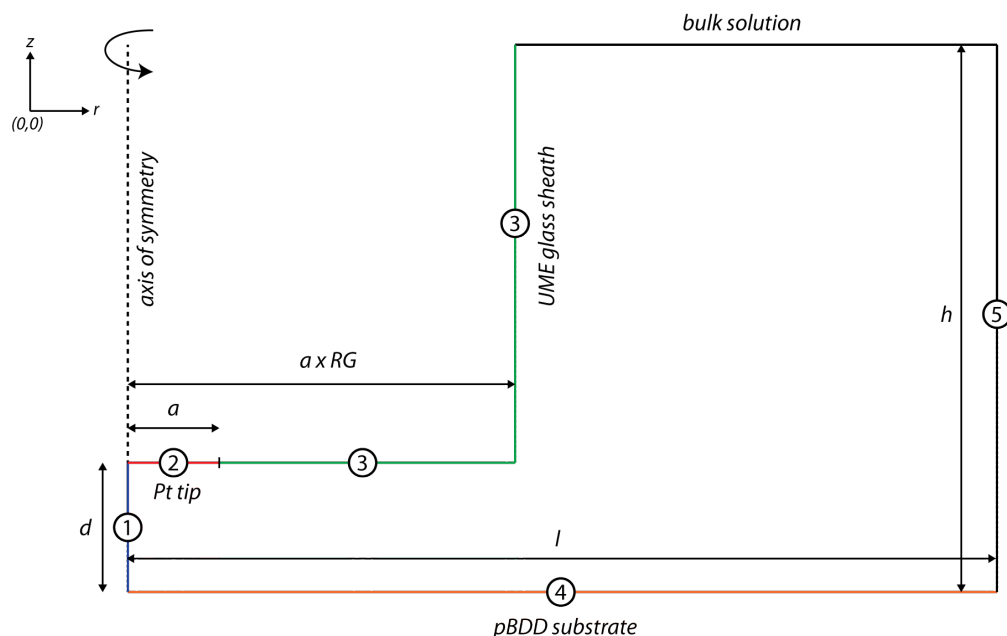


Figure 5.1: 2D simulation domain (height, h , is $200\text{ }\mu\text{m}$) for the SG-TC set-up (not to scale); d between the Pt UME and pBDD is typically $1.0\text{ }\mu\text{m}$.

The Butler-Volmer equations¹⁷ (Eq. 5.4 and Eq. 5.5) were used to describe HET kinetics at the pBDD electrode/solution interface:

$$k_f = k^0 \exp \left[-\alpha \frac{\eta F}{RT} \right] \quad (5.4)$$

$$k_b = k^0 \exp \left[(1 - \alpha) \frac{\eta F}{RT} \right] \quad (5.5)$$

where k_f and k_b are as defined previously, R is the ideal gas constant, T is the temperature, α is the transfer coefficient and η is the overpotential, $E - E^0$, where E^0 is the formal potential of the electrode. Simulations were carried out for $T = 298$ K, as employed in the experiments and $\alpha = 0.5$.

As an example, Figure 5.2 shows the steady-state $\text{Ru}(\text{NH}_3)_6^{3+}$ concentration profile

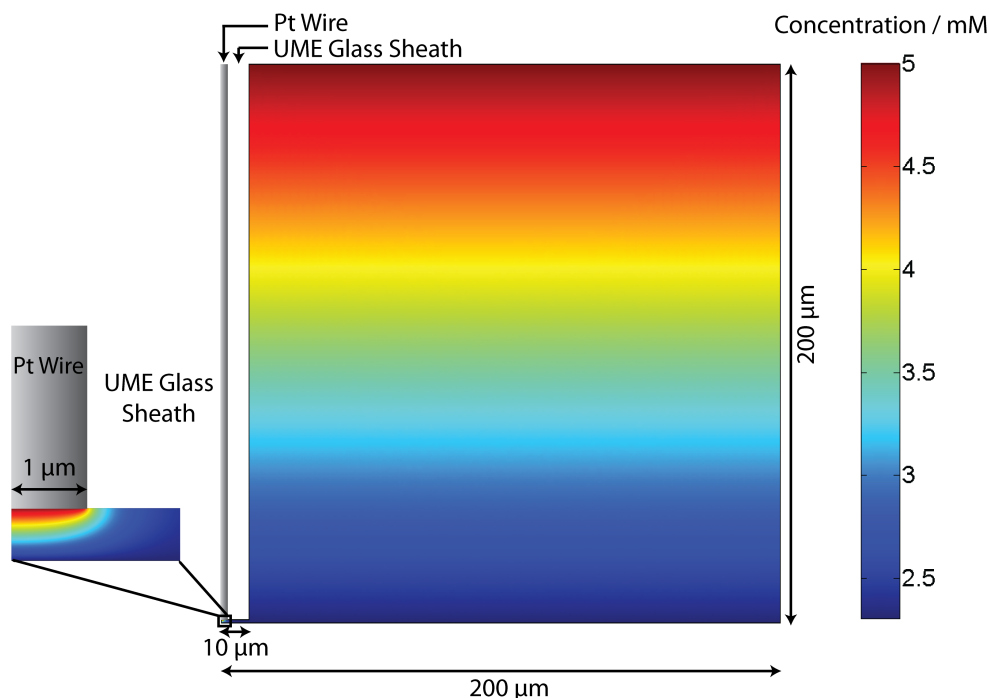


Figure 5.2: Example simulated steady-state diffusion-limited concentration profile of $\text{Ru}(\text{NH}_3)_6^{3+}$ (present in bulk solution at a bulk concentration of 5 mM) in the SG-TC mode with an overpotential, $\eta = -0.004$ V and $k^0 = 0.1 \text{ cm s}^{-1}$ at the pBDD surface.

in SG-TC mode. The pBDD substrate is at an overpotential, $\eta = -0.004$ V, at which $\text{Ru}(\text{NH}_3)_6^{3+}$ is partially reduced to $\text{Ru}(\text{NH}_3)_6^{2+}$, which is subsequently collected at the Pt UME tip.

Figure 5.3 considers in more detail the concentration profiles and flux distribution for parameters appropriate for the study of $\text{Ru}(\text{NH}_3)_6^{3+/2+}$, with $\eta = -0.004$ V. The plots highlight that the majority of the flux to the tip electrode comes from the region of the substrate electrode directly below the tip. For high k^0 values ($k^0 = 0.1 \text{ cm s}^{-1}$), 70 % of the flux is collected from the region directly below the tip and 95% from within a distance of two radii. For lower k^0 values ($k^0 = 0.01 \text{ cm s}^{-1}$), 80% of the total flux comes from within two radii away. Since all recorded

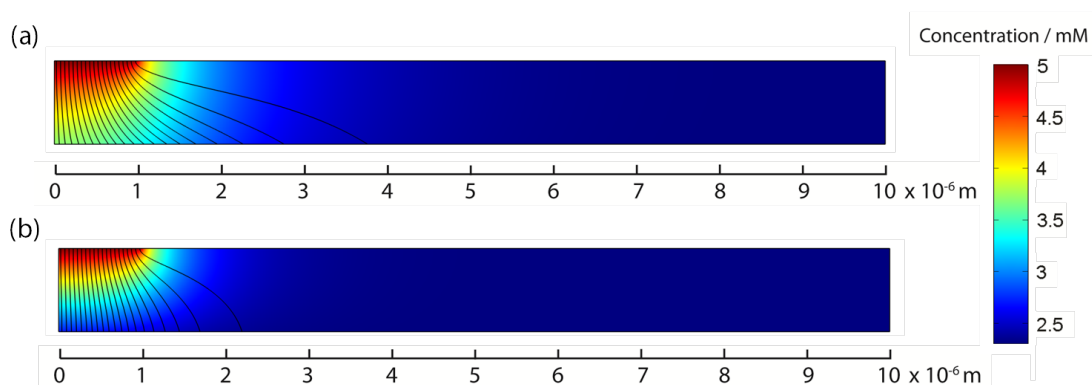


Figure 5.3: Contour plots (and concentration profiles) showing the flux to the tip electrode ($a = 1.0 \mu\text{m}$) from the substrate, $d = 1.0 \mu\text{m}$, at 5% intervals for k^0 values of (a) 0.1 cm s^{-1} and (b) 0.01 cm s^{-1} (for the case of $\text{Ru}(\text{NH}_3)_6^{3+}$ with $\eta = -0.004 \text{ V}$). These are as examples of maximum and minimum rate constants observed in the IC-SECM measurements.

k^0 values lie within this range, these data illustrate that it is reasonable to model the substrate with uniform activity, as the flux to the tip is only affected by a very small region of the substrate at the small tip-substrate separations used, and thus, to a first approximation, the heterogeneity of the whole sample does not need to be considered. Note that for $\text{FcTMA}^{+/2+}$, the kinetics are faster (*vide infra*), giving greater spatial resolution.

A series of simulations were carried out whereby k^0 was varied systematically and the limiting Pt UME tip current magnitude, i_{tip} , was obtained for each k^0 , producing a sigmoidal plot of i_{tip} vs. $\log(k^0)$ for each set of experimental conditions (Figure 5.4). A Boltzmann curve was then fitted to the simulation data to obtain an analytical expression for the form of the curve. The experimental i_{tip} currents could then be readily converted into a k^0 value, and the IC-SECM maps plotted as k^0 versus tip x, y position to obtain quantitative information on HET activity across the heterogeneously doped surface.

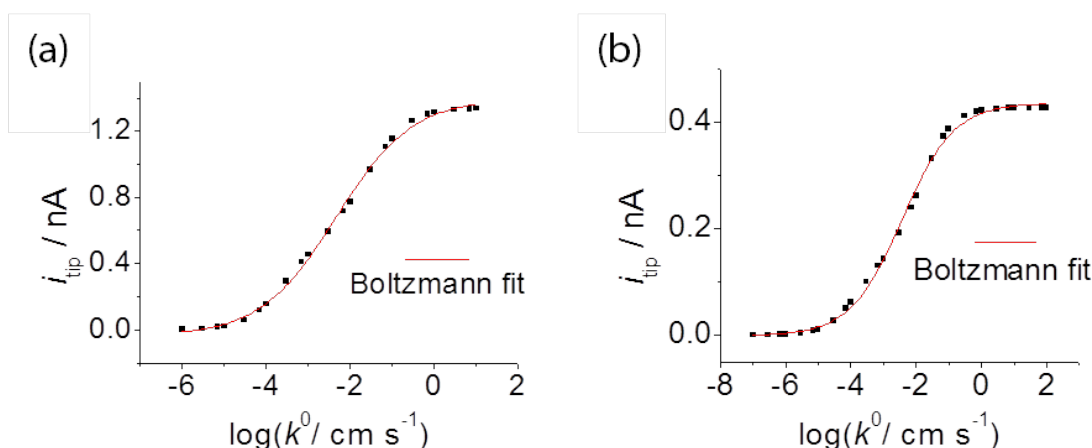


Figure 5.4: Plots of simulated Pt UME tip limiting current magnitude versus $\log(k^0)$ for: (a) collection of $\text{Ru}(\text{NH}_3)_6^{2+}$ (by oxidation), electrogenerated at the surface of the pBDD ($\eta = -0.004$ V); (b) collection of FcTMA^{2+} (by reduction) electrogenerated at the surface of the pBDD ($\eta = 0.045$ V).

5.3 ANALYSIS OF THE ELECTROACTIVITY OF pBDD WITH DIFFERENT REDOX MEDIATORS

5.3.1 CHARACTERISATION OF THE pBDD SAMPLE

The field emission scanning electron microscopy (FE-SEM) image shown in Figure 5.5(a) clearly shows the heterogeneous structure of the pBDD surface, due to differences in dopant densities between facets. Previous studies have shown that the darker regions in electron microscopy images contain a higher concentration of boron, which is confirmed by the Raman map corresponding to the same region (Figure 5.5(b)).¹⁹ Here, the integrated area beneath the sp^3 peak centred at 1332 cm^{-1} is directly related to boron concentration, decreasing as the

boron concentration increases, causing a shift of the peak to lower wavenumbers.²⁰ Therefore the darker regions correspond to areas of higher boron content, as observed in the FE-SEM image.

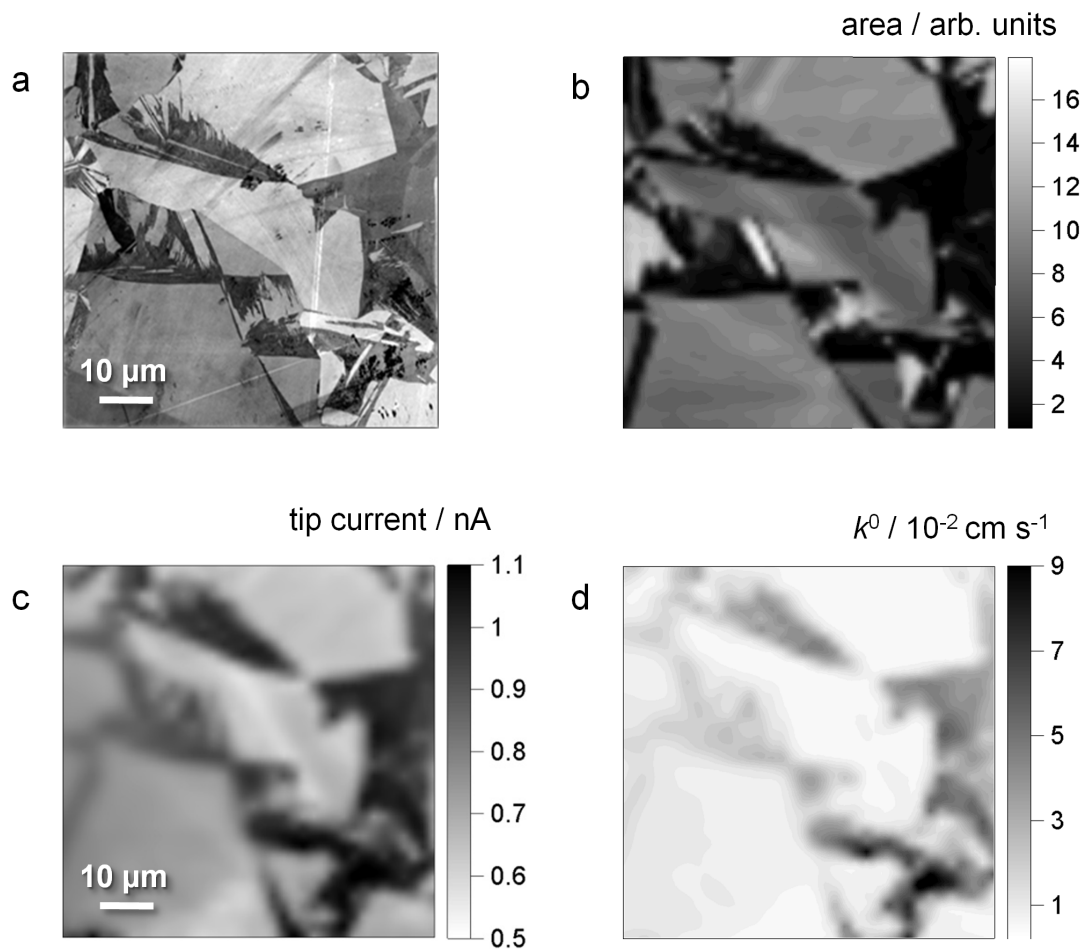


Figure 5.5: Images of a 70 μm × 70 μm region of pBDD obtained with (a) FE-SEM at 2 kV with an in-lens detector, (b) Raman microscopy, with each pixel displaying the integrated area beneath the peak centred at ~ 1332 cm⁻¹ as a function of laser spot position, (c) IC-SECM SG-TC mapping for the collection of Ru(NH₃)₆²⁺, electrogenerated at the pBDD surface ($\eta = -0.004$ V). (d) shows the k^0 values determined from the tip currents in (c) with FEM simulations.

5.3.2 IC-SECM IMAGING

To determine the effect of differences in boron concentration on the local electrochemical activity of the pBDD surface, IC-SECM imaging was carried out in substrate generation tip collection (SG-TC) mode (Figure 5.6). The sample was biased at a potential of -0.17 V ($\eta = -0.004$ V) vs. the Ag/AgCl wire reference electrode (with a Pt wire counter electrode), in order to drive the reduction of hexamine ruthenium chloride ($\text{Ru}(\text{NH}_3)_6^{3+}$) present in solution (with 50 mM KNO_3 supporting electrolyte). The reduced species was subsequently collected at the UME which was held at 0.0 V, and the resulting current was recorded as the tip was scanned across the sample. The positional feedback available with IC-SECM was of critical importance in obtaining high resolution images. A constant distance between tip and substrate of 1 μm was maintained throughout each scan, enhancing mass transport of both forms of the electroactive species, and therefore increasing the measured currents. The tip current map shown in Figure 5.5(c), shows a clear correlation between electrochemical activity and boron dopant concentration, and that all facets of the substrate are active.

To extract more precise kinetic information about the rate of HET, FEM simulations were used, modelling the kinetics at the pBDD surface with the Butler-Volmer equations, to determine the standard HET rate constant, k^0 . The kinetic map in Figure 5.5(d) indicates that the highly doped facets all exhibit a similar level of activity, as do the lower doped facets.

To gain further insights into HET rates at pBDD, the oxidation of

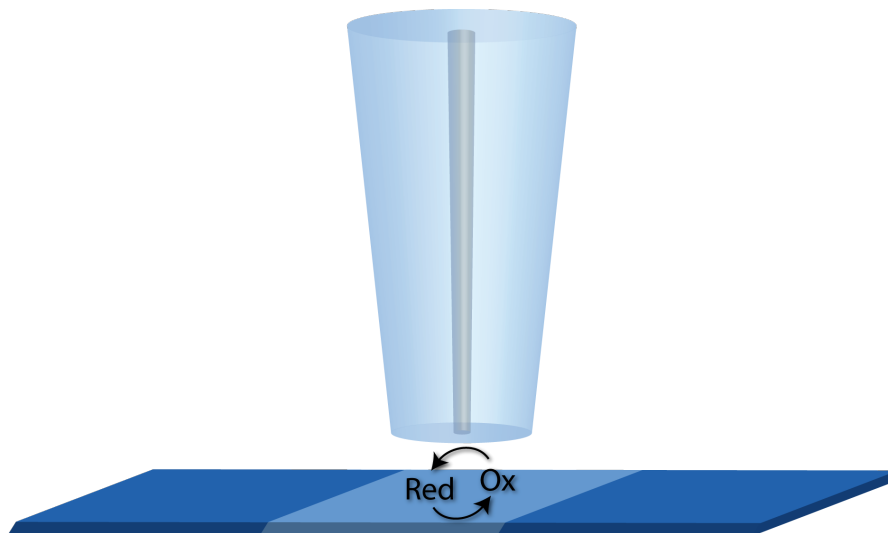


Figure 5.6: Schematic of IC-SECM setup in substrate generation tip collection mode. The species is reduced at the surface and subsequently oxidised at the tip.

ferrocenylmethyltrimethylammonium, FcTMA^+ , was also studied. Figure 5.7 shows the FE-SEM, Raman, IC-SECM and k^0 images for part of the pBDD surface, with similar differences in activity between areas of high and low boron concentration observed as with $\text{Ru}(\text{NH}_3)_6^{3+}$. The redox potential of $\text{FcTMA}^{+/2+}$ is considerably more positive than $\text{Ru}(\text{NH}_3)_6^{3+/2+}$, so the sample was biased at a potential of 0.42 V ($\eta = 0.045$ V) to drive the oxidation of FcTMA^+ , with the UME held at 0.0 V to collect back the oxidised species.

5.3.3 KINETIC ANALYSIS

In order to analyse the kinetics of the higher and lower doped regions individually, a threshold method was applied to the k^0 values. Threshold values of $k^0 > 5 \times 10^{-2} \text{ cm s}^{-1}$ for FcTMA^+ oxidation and $k^0 > 1.5 \times 10^{-2} \text{ cm s}^{-1}$ for $\text{Ru}(\text{NH}_3)_6^{3+}$ reduction yielded the results shown in Figure 5.8, with values above the threshold identified

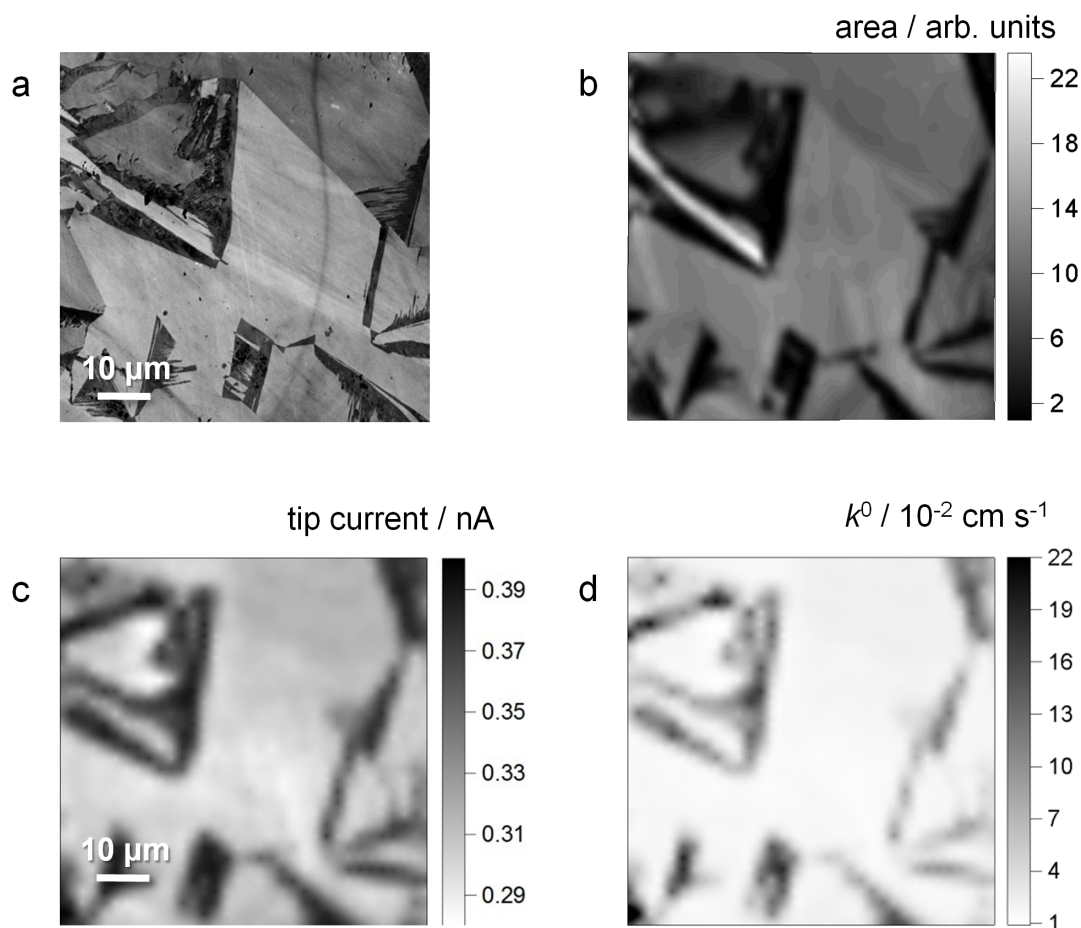


Figure 5.7: Images of a $70\ \mu\text{m} \times 70\ \mu\text{m}$ region of pBDD obtained with (a) FE-SEM at 2 kV with an in-lens detector, (b) Raman microscopy, with each pixel displaying the integrated area beneath the peak centred at $\sim 1332\ \text{cm}^{-1}$ as a function of laser spot position, (c) IC-SECM SG-TC mapping for the collection of FcTMA^{2+} , electrogenerated at the pBDD surface ($\eta = 0.045\ \text{V}$). (d) shows the k^0 values determined from the tip currents in (c) with FEM simulations.

with a black dot.

The data from the two regions were used to determine average k^0 values for the oxidation of FcTMA^+ , giving $k^0 = 9.7(\pm 4.0) \times 10^{-2}\ \text{cm s}^{-1}$ for the high doped facets and $k^0 = 2.2(\pm 0.8) \times 10^{-2}\ \text{cm s}^{-1}$ for the low doped facets. For the

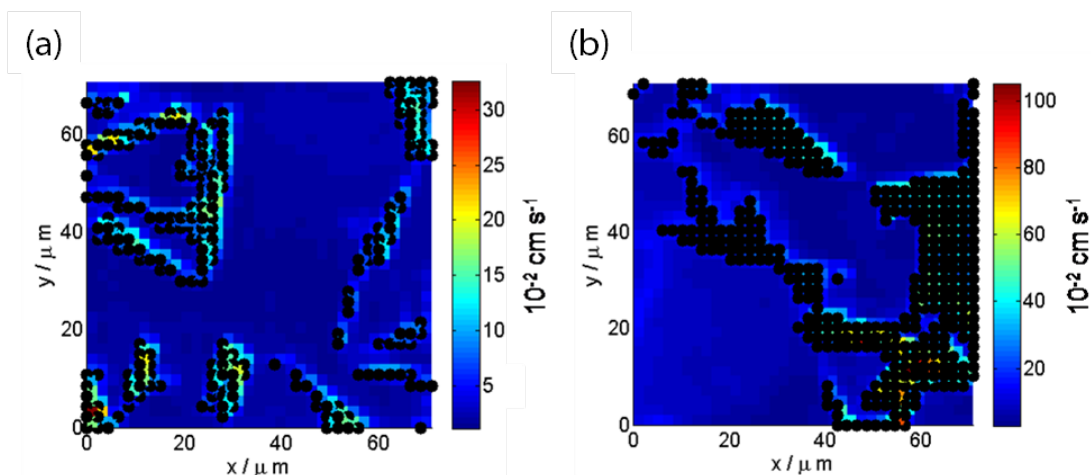


Figure 5.8: IC-SECM HET images with values above the assigned threshold of k^0 identified as black dots for (a) the oxidation of FcTMA^+ and (b) the reduction of $\text{Ru}(\text{NH}_3)_6^{3+}$.

$\text{Ru}(\text{NH}_3)_6^{3+}$ case, values of $k^0 = 3.3(\pm 1.5) \times 10^{-2} \text{ cm s}^{-1}$ for the high doped facets, and $k^0 = 0.7(\pm 0.3) \times 10^{-2} \text{ cm s}^{-1}$ for the low doped facets were obtained. These kinetic values further support the Raman data (Figure 5.5), which indicate the whole area is doped with sufficiently high boron concentrations to ensure metal-like behaviour with no semiconducting regions. Since the redox potential for $\text{Ru}(\text{NH}_3)_6^{3+}$ lies in the band gap of semiconducting BDD (illustrated in Figure 5.9),²¹ if any of these regions were present, considerably lower HET kinetic rates would be expected than are observed here. Interestingly, the ratio of k^0 values between high and low doped facets is approximately 4 for both mediators.

The FEM simulations used to determine the kinetic rate constants are subject to several assumptions which may impact the extracted k_0 values. The largest source of error in the model is the radius of the Pt wire, since this is calculated from CV measurements run prior to IC-SECM imaging (see section 2.2.3 for details) and not measured directly. The determined values ranged between 0.9



Figure 5.9: Band structure for p-type semiconducting BDD, where E_{VB} is the valence band potential, E_{CB} is the conduction band potential and E_A is the acceptor band, arising due to boron doping.

and $1.3\ \mu\text{m}$ demonstrating the variability between measurements. Another source of error comes from the assumption that the transfer coefficient, α , is 0.5, which may be an oversimplification for this semi-metallic material. However, since these assumptions are consistent within each IC-SECM map, the determined k_0 values will show the same qualitative relationship between the high and low doped regions, even though the quantitative values may exhibit some inaccuracies.

5.4 DETERMINATION OF THE LOCAL DENSITY OF STATES

To investigate this relationship between k_0 values for the high and low doped regions, capacitance measurements were carried out in regions of different boron dopant concentration to infer information about the local density of states (LDOS) of the material. To ensure the capacitance of different facets could be

measured independently, an SECCM setup was used,²² confining the measurements to the size of the meniscus at the end of the capillary, which was approximately 1.4 μm . The pulled theta pipet (filled with electrolyte solution (50 mM KNO_3) and containing an Ag/AgCl wire quasi-reference counter electrode (QRCE)) was approached towards the surface whilst a sinusoidal oscillation was applied to its z -position (200 nm amplitude, 80 Hz frequency). A bias of 200 mV was applied between the two QRCEs generating a conductance current, and contact with the substrate was detected via a change in the AC component of this current. A 0.15 V peak-to-peak triangular wave centred on 0.0 V (scan rate $\nu = 30 \text{ V s}^{-1}$) was applied to the QRCEs (whilst maintaining the bias between them) with respect to the substrate. The observed current amplitude, i_{amp} , is defined as the difference between the current values for the forward and reverse scans and is related to capacitance via the following equation:

$$C_{\text{meas}} = \frac{i_{\text{amp}}}{2\nu A} \quad (5.6)$$

where A is the area of the electrode, in this case defined by the region of the substrate in contact with the meniscus.

Measured capacitance values, C_{meas} , of $5.2(\pm 0.8) \text{ mF cm}^{-2}$ for high doped facets and $3.1(\pm 0.4) \text{ mF cm}^{-2}$ for low doped facets were observed, which, when assuming a typical value of $20 \mu\text{F cm}^{-2}$ for the Helmholtz capacitance (C_{H}), gives values for the LDOS of $6.3(\pm 2.0) \times 10^{20} \text{ cm}^{-3} \text{ eV}^{-1}$ and $1.7(\pm 0.7) \times 10^{20} \text{ cm}^{-3} \text{ eV}^{-1}$, for the

high and low doped facets respectively, from the following equations.²³

$$C_{\text{meas}}^{-1} = C_{\text{H}}^{-1} + C_{\text{SC}}^{-1} \quad (5.7)$$

$$C_{\text{SC}} = \sqrt{e_0 \epsilon \epsilon_0 D(E_{\text{f}})} \quad (5.8)$$

Here C_{SC} is the capacitance of the space charge region, e_0 is the electronic charge, ϵ is the dielectric constant of pBDD, ϵ_0 is the vacuum permittivity and $D(E_{\text{f}})$ is the LDOS at the Fermi level. Comparing the values of the LDOS for the two regions, gives a ratio of approximately 4 between high and low doped facets, corresponding with the k^0 values obtained from FEM simulations. Based on these observations, it can be concluded that HET kinetics at the pBDD surface are largely governed by the LDOS, which are determined by the local concentration of boron present.

5.5 CONCLUSIONS

IC-SECM has provided a powerful tool for extremely high resolution imaging of heterogeneous surfaces, producing images with much greater detail than would be possible with conventional SECM. Analysing data from this technique with FEM simulations allows a wealth of information to be extracted on electrode kinetics, providing quantitative analysis of HET rates. Areas of different boron concentration, identified with FE-SEM and Raman spectroscopy, clearly exhibit different levels of electrochemical activity for the oxidation of FcTMA^+ and the reduction of $\text{Ru}(\text{NH}_3)_6^{3+}$. Modelling the measured electrochemical currents has allowed k^0 values to be determined, and analysis of these values in high and low

doped regions reveals a similar difference for both mediators. With micro-scale capacitance measurements, the LDOS for each region has been estimated, which differs by a factor of 4 between high and low doped facets. This suggests that the LDOS has a significant influence on the HET kinetics observed and is itself dependent on the local dopant density of the material.

5.6 REFERENCES

- [1] Khoshtariya, D. E.; Dolidze, T. D.; Shushanyan, M.; Davis, K. L.; Waldeck, D. H.; van Eldik, R. *Proceedings of the National Academy of Sciences* **2010**, *107*, 2757–2762.
- [2] Shen, M.; Bard, A. J. *Journal of the American Chemical Society* **2011**, *133*, 15737–15742.
- [3] Smalley, J. F.; Finklea, H. O.; Chidsey, C. E. D.; Linford, M. R.; Creager, S. E.; Ferraris, J. P.; Chalfant, K.; Zawodzinsk, T.; Feldberg, S. W.; Newton, M. D. *Journal of the American Chemical Society* **2003**, *125*, 2004–2013.
- [4] Murray, R. W. *Chemical Reviews* **2008**, *108*, 2688–2720.
- [5] Mishra, A. K.; Waldeck, D. H. *The Journal of Physical Chemistry C* **2009**, *113*, 17904–17914.
- [6] Bano, K.; Nafady, A.; Zhang, J.; Bond, A. M.; ul Haque, I. *The Journal of Physical Chemistry C* **2011**, *115*, 24153–24163.
- [7] Gosavi, S.; Marcus, R. A. *The Journal of Physical Chemistry B* **2000**, *104*, 2067–2072.
- [8] Amemiya, S.; Nioradze, N.; Santhosh, P.; Deible, M. J. *Analytical Chemistry* **2011**, *83*, 5928–5935.
- [9] Wipf, D. O.; Kristensen, E. W.; Deakin, M. R.; Wightman, R. M. *Analytical Chemistry* **1988**, *60*, 306–310.
- [10] Bond, A. M.; Henderson, T. L. E.; Mann, D. R.; Mann, T. F.; Thormann, W.; Zoski, C. G. *Analytical Chemistry* **1988**, *60*, 1878–1882.

- [11] Birkin, P. R.; Silva-Martinez, S. *Analytical Chemistry* **1997**, *69*, 2055–2062.
- [12] Mirkin, M. V.; Bulhoes, L. O. S.; Bard, A. J. *Journal of the American Chemical Society* **1993**, *115*, 201–204.
- [13] Miao, W.; Ding, Z.; Bard, A. J. *The Journal of Physical Chemistry B* **2002**, *106*, 1392–1398.
- [14] Smith, G. D. *Numerical Solution of Partial Differential Equations: Finite Difference Methods*, 3rd ed.; Oxford University Press, 1985.
- [15] Huebner, K. H.; Dewhurst, D. L.; Smith, D. E.; Byrom, T. G. *The Finite Element Method for Engineers*, 4th ed.; Wiley & Sons, Inc, New York, 2001.
- [16] McKelvey, K.; Edwards, M. A.; Unwin, P. R. *Analytical Chemistry* **2010**, *82*, 6334–6337.
- [17] Bard, A. J.; Faulkner, L. R. *Electrochemical Methods: Fundamentals and Applications*, 2nd ed.; John Wiley & Sons Inc.: New York, 2001.
- [18] Amatore, C.; Szunerits, S.; Thouin, L.; Warkocz, J.-S. *Journal of Electroanalytical Chemistry* **2001**, *500*, 62–70.
- [19] Miller, J. B.; Brandes, G. R. *Journal of Applied Physics* **1997**, *82*, 4538–4545.
- [20] Bernard, M.; Deneuve, A.; Muret, P. *Diamond and Related Materials* **2004**, *13*, 282–286.
- [21] Holt, K. B.; Bard, A. J.; Show, Y.; Swain, G. M. *The Journal of Physical Chemistry B* **2004**, *108*, 15117–15127.
- [22] Ebejer, N.; Schnippering, M.; Colburn, A. W.; Edwards, M. A.; Unwin, P. R. *Analytical Chemistry* **2010**, *82*, 9141–9145.
- [23] Gerischer, H. *The Journal of Physical Chemistry* **1985**, *89*, 4249–4251.

CHAPTER 6

A NEW APPROACH FOR THE FABRICATION OF MICROSCALE LIPID BILAYERS AT GLASS PIPETTES: APPLICATIONS FOR PASSIVE PERMEATION VISUALISATION

In this chapter, a new method of planar lipid bilayer formation is presented, which overcomes many of the limitations of conventional bilayer preparation techniques. With this method, stable, solvent-free lipid bilayers exhibiting a high seal resistance can be formed rapidly, easily and reproducibly. Using these bilayers, the passive permeation of a series of carboxylic acids is investigated, to determine the trend in permeability with lipophilicity. Bilayers are formed at the tip openings of pulled theta pipettes, and the rate of permeation of each carboxylic acid across the bilayer, from within the pipette into the bulk solution is determined. The pH change associated with the permeation of a weak acid is measured using a pH-sensitive fluorophore, which can be visualised with the confocal laser scanning microscope. Fluorescence profiles can then be extracted and matched to FEM simulations in order to determine the permeation coefficient for each species. Analysis of the series of weak acids shows increasing permeability with lipophilicity, in agreement with Overton's rule.

6.1 INTRODUCTION

For almost 50 years, planar lipid bilayers, or black lipid membranes (BLMs), have been used as model cell membrane systems to investigate a variety of cellular processes.¹ They are widely used to study the transport of molecules across cell membranes either via passive diffusion,²⁻⁹ or active transport involving ion channels.¹⁰⁻¹⁴ BLMs containing reconstituted ion channels have been used for many years to investigate the interaction of ligands with receptor protein channels,^{15,16} however, recently there has been considerable interest in the use of ion channels as biosensors¹⁷ for both organic¹⁸⁻²⁰ and inorganic molecules²¹ and DNA sequencing.^{22,23}

Methods for the study of passive permeation across BLMs are of particular interest since most drug compounds are transported via this mechanism, and, as such, BLMs are used in both high throughput drug screening²⁴⁻²⁶ and more detailed studies of trends in permeation rates between molecules.^{3,5,7,8} Permeation coefficients of small molecules have commonly been analysed using Overton's rule,²⁷ which considers the permeation coefficient, P , of a molecule, across a membrane between two aqueous solutions to be proportional to the product of the partition coefficient, K , and diffusion coefficient, D of the molecule in the membrane.²⁸ There has, however, been some debate as to whether this simplistic view of the permeation process is sufficient to describe the permeation of all small molecules, since it does not take into account the amphipathic nature of the phospholipids in a lipid bilayer. Whilst the majority of studies show a positive correlation between lipophilicity and permeation rate,

the relationship is often not linear^{4,29} and there is considerable variation in the P values reported for the same molecules.^{3,7-9} Some studies have seen contrasting trends for some molecules, suggesting permeation may be governed by other factors such as diffusion.^{2,30} However, several of the existing techniques have limitations which limit the accurate measurement of permeation coefficients.

A significant issue in permeation studies is the method of bilayer formation. For example, one of the most widely used procedures, the painting method,³¹ produces lipid bilayers which contain residual solvent molecules in the interior of the bilayer, raising questions about the integrity and reliability of such model membranes.³² This is also problematic for ion channel experiments, since these molecules may denature any proteins embedded in the BLM. The folding method³³ produces BLMs containing less residual solvent, and lipid bilayers produced by the tip-dip method³⁴ are solvent-free, but have comparatively short lifetimes, making them unsuitable for ion channel recordings which can take many hours. Improvements in BLM stability have been achieved through the use of gel-phase materials which have produced bilayers which are extremely durable,³⁵⁻⁴⁰ however, due to the slow diffusion of analytes through the gel, the temporal responses are very slow.¹⁹

Some of the challenges associated with the use of planar lipid bilayers in permeation measurements may be overcome with the use of liposomes. With most methods of liposome preparation, there is no issue of residual solvent molecules in the interior of the membrane and they are typically stable for considerably longer periods than planar lipid bilayers. However, since the interior of the liposome is inaccessible for sampling, measurement of permeation rates can be difficult. NMR techniques can

be used, but only give a bulk view of the process at steady state. Recently CLSM has been employed to give increased resolution of the permeation of molecules into a single liposome.⁴¹ Using this technique, it is possible to study not only fluorescent permeants but also weak acids, by means of a pH-sensitive fluorophore, enabling visualisation of local pH changes as the molecule permeates either into a liposome²⁹ or across a BLM.²

In conventional bilayer systems, BLMs are formed across an aperture in a polymer membrane e.g. Teflon, up to 100 μm in diameter. The surface area of the lipid bilayer affects the membrane capacitance which accounts for much of the noise in the system.⁴² By reducing the size of the aperture, the system noise is reduced which allows for greater resolution in ionic current recordings, which is particularly advantageous for single ion channel measurements. White and co-workers reported the formation of suspended lipid bilayers over glass nanopores of < 100 nm, which show very high mechanical and electrical stability, and extremely low capacitance due to the small area of the bilayers.⁴³ The use of fused quartz instead of glass in the fabrication of nanopore membranes, further improves the electrical properties of the bilayers, with seal resistances of > 1 T Ω reported for nanopores as small as 6 nm.⁴⁴ These nanopore membranes are particularly suitable for ion channel recordings as their small size limits the number of channels that can be inserted, and exceptionally low leakage currents give excellent current resolution. Furthermore, ion channels can be reproducibly incorporated upon the application of a small positive pressure and subsequently removed by a small negative pressure whilst leaving the bilayer intact.⁴⁵

Here, we report the use of dual-barrel theta capillaries for the formation of

exceptionally stable, solvent-free, suspended BLMs. This method enables the formation of bilayers simply, quickly and reproducibly, which are long-lasting and exhibit resistances up to 600 G Ω . Using this system, we determine the permeation coefficients of a series of aliphatic carboxylic acids as they passively permeate across the bilayer. By using CLSM with a pH-sensitive fluorophore,^{2,29} the movement of these molecules can be tracked by monitoring the local pH changes around the end of the pipette. Combining this with FEM modelling, permeation coefficients for the series of acids can be extracted to determine the effect of permeant lipophilicity on permeability. By positioning quasi-reference counter electrodes (QRCEs) on either side of the bilayer, the effect of a potential field on the permeation rate of molecules can also be investigated.

6.2 PRINCIPLES

The simple method of BLM fabrication presented herein enables the rapid formation of solvent-free, suspended bilayers with exceptional electrical properties. To form these bilayers, borosilicate glass theta capillaries are pulled using a laser puller to produce pipettes with tapered tip openings 5-10 μm in diameter. The two pipette barrels are half-filled with the weak acid solution and a QRCE is inserted into each barrel. A small potential (typically 100 mV) is applied between the two to ensure there is a well-formed meniscus at the end of the pipette before it is immersed into the lipid solution (1 mg/ml 1,2-dipalmitoyl-sn-glycero-3-phosphocholine (DPPC) or soy phosphatidylcholine (PC) in chloroform) (Figure 6.1(a)). This concentration is sufficiently high that a monolayer assembles at the oil/water interface, which can be tracked by

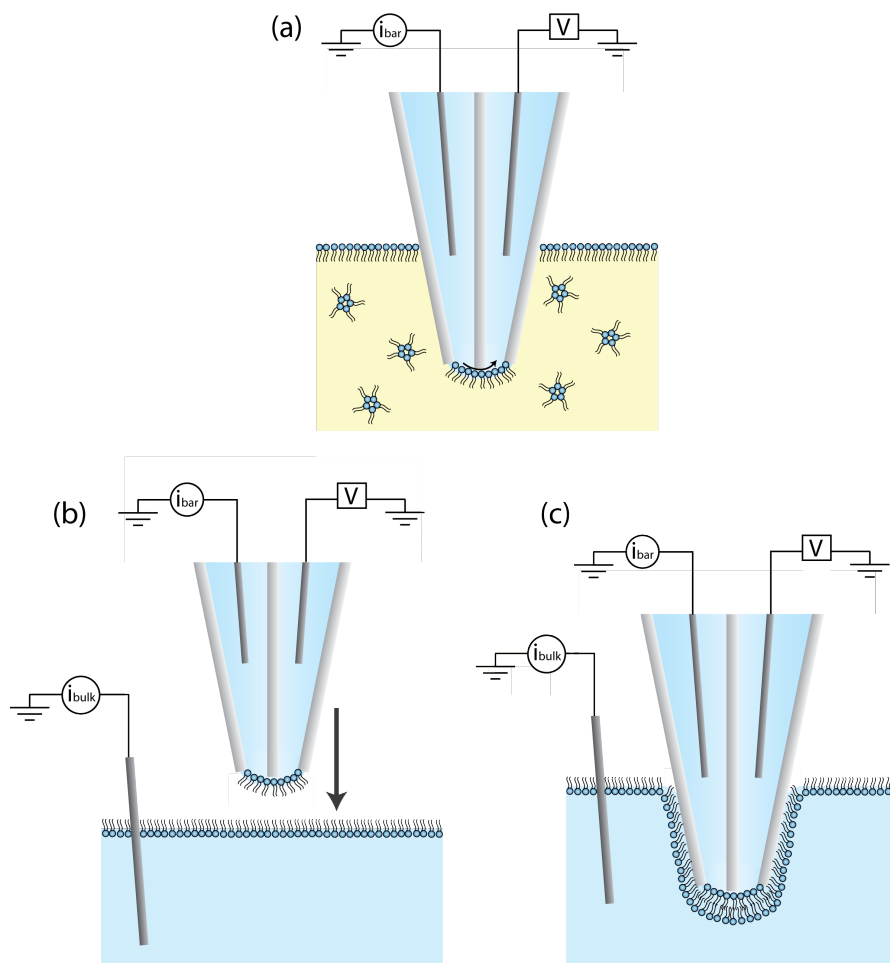


Figure 6.1: Schematic illustration of the bilayer formation process. The pipette is lowered into the lipid solution (in chloroform) whilst applying a small potential between the two QRCEs to ensure the meniscus is well-formed (a). The pipette is held in the solution for one minute before it is retracted, and the cell and solution replaced with an aqueous electrolyte. A small volume of lipid solution (in chloroform) is dropped onto the aqueous electrolyte and the volatile organic solvent allowed to evaporate forming a lipid monolayer (b). The pipette is then slowly lowered until the two monolayers make contact and a bilayer is formed (c).

monitoring the change in resistance (current, i_{bar}) between the two QRCEs in the theta pipette. As the monolayer assembles, the resistance between the pipette barrels increases from $\sim 3\text{-}5\text{ M}\Omega$ to $\sim 2\text{-}10\text{ G}\Omega$ as the meniscus is compressed.

Once fully assembled, the pipette is removed from the lipid solution, leaving the monolayer intact on the meniscus of the pipette and allowing any residual volatile solvent molecules to easily evaporate (Figure 6.1(b)). The pipette is then positioned above an electrolyte solution onto the surface of which, a small amount of lipid solution ($\sim 10 \mu\text{l}$) is dropped, forming a monolayer at the air/water interface.

Pressure/area isotherms for the DPPC were recorded using a Langmuir trough, indicating that for a fully assembled monolayer, the area per molecule is $\sim 35 \text{ \AA}^2$ with a surface pressure of $\sim 50 \text{ mN m}^{-1}$ (Figure 6.2). To ensure full monolayer coverage on the surface of the bulk electrolyte solution in the CLSM cell, $10 \mu\text{l}$ of 1 mg/ml lipid solution is added, giving a theoretical area per lipid of 34 \AA^2 .

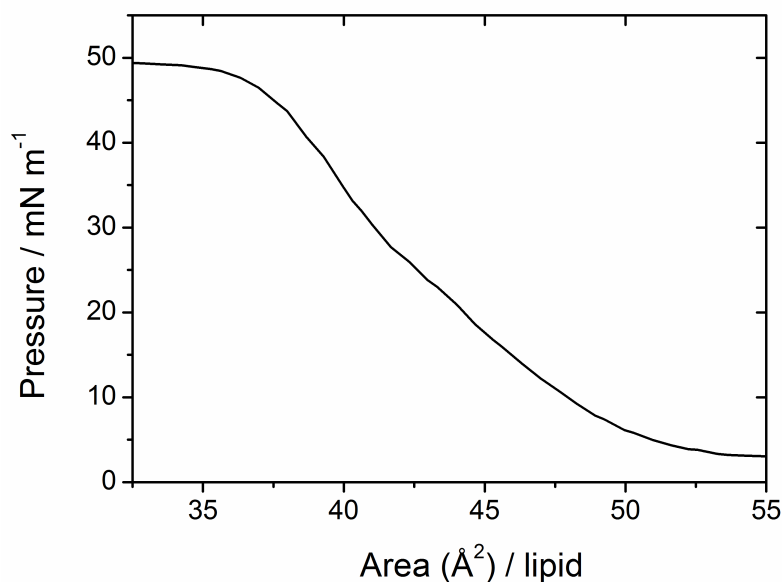


Figure 6.2: Pressure/area isotherm for the compression of a DPPC monolayer.

A third QRCE is placed into the bulk electrolyte solution to monitor the resistance across the bilayer as it forms. The pipette is slowly lowered until the

two monolayers make contact and a bilayer is formed (Figure 6.1(c)). Once formed, the current between the pipette and bulk solution (i_{bulk}) is monitored as the potential is varied to determine the resistance of the bilayer from the current-voltage curves produced.

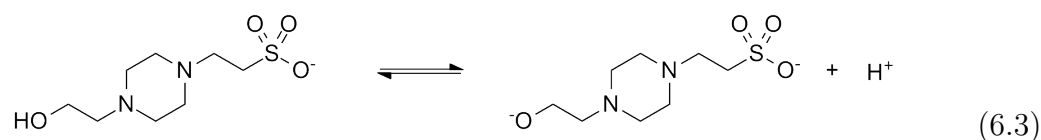
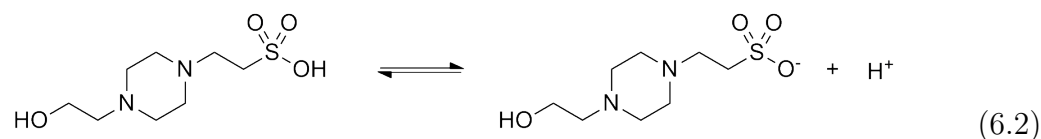
For the measurement of permeation coefficients, the pipettes are filled with a carboxylic acid solution containing 0.1 M KCl and 5 μM fluorescein which is adjusted to pH ~ 4.2 to ensure the protonated form of the weak acid is the dominant species. Since charged species cannot permeate across the bilayer, it is important to ensure the carboxylic acids are in the neutral form.⁴⁶ The bulk solution, into which the molecules permeate, contains 0.1 M KCl, 50 μM HEPES and the pH-sensitive fluorophore fluorescein (5 μM), which is adjusted to pH 8 so that any permeating weak acid molecules tend to dissociate, changing the pH locally. This pH change can be visualised using the confocal laser scanning microscope and the resulting fluorescence profiles analysed with FEM simulations to elucidate permeation coefficients as described herein.

6.3 THEORY AND SIMULATIONS

Using FEM modelling, the steady state fluorescence profiles arising due to the permeating species can be simulated as a function of permeation coefficient, which is the only adjustable parameter in the simulations. For each weak acid (HX) studied, the following solution process was considered:



where X^- is the conjugate anion of the weak acid, the concentration of which is dependent on the local pH and pK_a of the weak acid. The bulk electrolyte solution was weakly buffered with 50 μ M HEPES to prevent pH changes in the bulk solution, and so the following equilibria were also included:



The very fast kinetics of the protonation processes compared to the experimental timescale mean that they could be considered as equilibria controlled by the local pH. To ensure the equilibria were handled correctly, the pK_a values for the weak acid and buffer were corrected for ionic activity with 0.1 M KCl using the Davies Equation.⁴⁷

For each species, i , modelled in the simulation (H^+ , X^- , HX , HEPES , HEPES^- , HEPES^{2-}), a time-independent solution to the reaction-diffusion equation below was sought

$$D_i \left(\frac{\partial^2 c}{\partial r^2} + \frac{1}{r} \frac{\partial c}{\partial r} + \frac{\partial^2 c}{\partial z^2} \right) + R_i = 0 \quad (6.4)$$

where c_i and D_i are the concentration and diffusion coefficient of species i respectively, r and z are the radial and normal coordinates with respect to the centre of the pipette, and R_i is the rate of production of species i in the domain (shown in Figure 6.3(a)). The diffusion coefficients and pK_a values for each of

the weak acids are listed in Table 6.1.

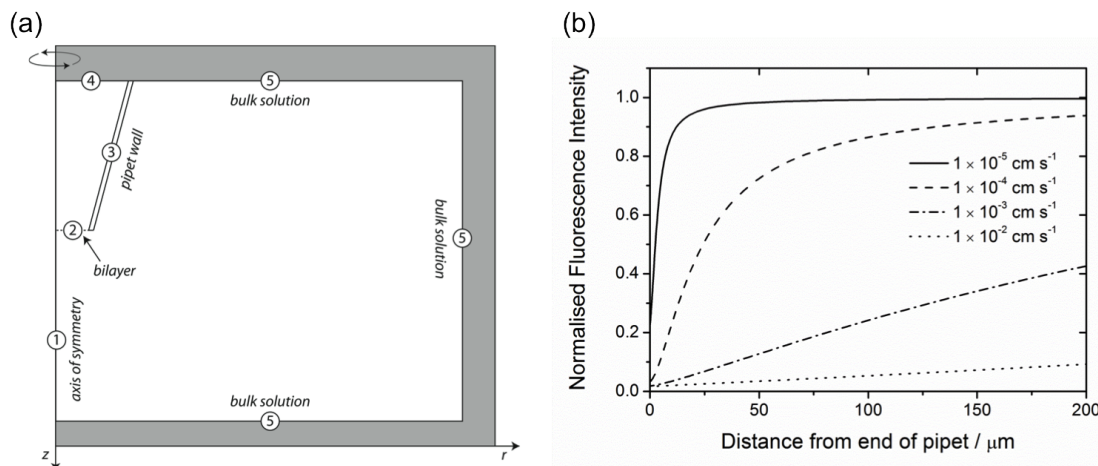


Figure 6.3: (a) Simulation domain for permeation coefficient determination. The pipette geometry is determined from optical microscopy and a range of permeation coefficients for the diffusion of the weak acid across the bilayer are simulated. (b) Series of simulated fluorescence profiles at different P values for the permeation of 100 mM propanoic acid.

Table 6.1: Diffusion coefficient, D_{HX} , and $\text{p}K_{\text{a}}$ values for each weak acid studied.²

| Carboxylic Acid | $\text{p}K_{\text{a}}$ | $D_{\text{HX}} (\times 10^{-6} \text{ cm}^2 \text{ s}^{-1})$ |
|-----------------|------------------------|--|
| Acetic | 4.76 | 12.71 |
| Propanoic | 4.83 | 9.18 |
| Butanoic | 4.83 | 8.17 |
| Hexanoic | 4.85 | 7.84 |

The protonation state of fluorescein has been shown to have no significant effect at the concentrations used here and was therefore ignored in the calculations.²

The finite element method was used to determine the concentration of each of the species on each side of the bilayer over time by solving equation 6.4 subject to the boundary conditions of the system which are summarised in Table 6.2. Here N_{bilayer} describes the flux of the neutral weak acid across the bilayer (with c_i^{out} and c_i^{in} , the concentration of the species outside and inside the pipette respectively). Although the neutral form of the HEPES buffer may permeate across the bilayer, due to the relatively high pH in the bulk solution, the concentration of the neutral molecule was less than 0.1 nM and so was not considered as a permeating species. All other species were treated as impermeable. The initial concentrations of each of the species, i , inside and outside of the pipette are denoted $c_i^{\text{in}*}$ and $c_i^{\text{out}*}$.

Table 6.2: Summary of the boundary conditions used for the simulation of the permeation of a weak acid across a bilayer.

| Label in Figure 6.3(a) | Boundary | Boundary Condition Type | Equation | |
|------------------------|------------------|-------------------------|--|---|
| 1 | Axis of Symmetry | Symmetry | $0 = \nabla c_i \cdot \underline{n}$ | |
| 2 | Bilayer | Flux/No Flux | $N_{\text{bilayer}} = P(c_i^{\text{out}} - c_i^{\text{in}})$ $0 = \nabla c_j \cdot \underline{n}$ | $i = \text{HX}$ $j = \text{all other species}$ |
| 3 | Pipette Wall | No Flux | $0 = \nabla c_i \cdot \underline{n}$ | |
| 4 | Top of Pipette | Concentration | $c_i^{\text{in}} = c_i^{\text{in}*}$ | |
| 5 | Bulk Solution | Concentration | $c_i^{\text{out}} = c_i^{\text{out}*}$ | |

The resulting steady-state profiles for the H^+ ions were converted to pH and subsequently to fluorescence intensity (I) using the empirical relation determined previously in our group for the pH dependency of fluorescein fluorescence

intensity under these conditions:²

$$I = 1 - \frac{0.983}{1 + e^{-3.36(6.18 - \text{pH})}} \quad (6.5)$$

A series of simulation profiles are shown for a typical acid which visibly demonstrates that this model is sensitive to permeation rates over 4 orders of magnitude (Figure 6.3(b)). Moreover, it is easily tuneable to a particular region by altering the experimental conditions: the pipette geometry, pH of internal and external solutions and buffer concentrations can all be varied.

To correlate the experimental data with the simulations, CLSM images were analysed to produce fluorescence profiles normal to the end of the pipette. To calculate the average fluorescence, a cone of pixels was selected normal to the end of the pipette and the fluorescence intensity was plotted against the absolute distance from the end of the pipette. A polynomial fit was then applied to reduce the experimental noise and this fit was matched to simulated profiles to extract a permeation coefficient. The raw fluorescence profile for the permeation of 100 mM propanoic acid is shown in Figure 6.4(a) along with the polynomial fit which allows for easier comparison with the simulated data whilst still preserving the main features of the profile. Figure 6.4(b) shows a 2D cross-section perpendicular to the plane of the bilayer in which the experimental CLSM fluorescence profile for the permeation of 100 mM propanoic acid has been converted into a pH map using equation 6.5. The simulated pH profile shows excellent agreement with the experimental data although the noise present in the fluorescence profile in Figure 6.4(b) is also evident in the CLSM image.

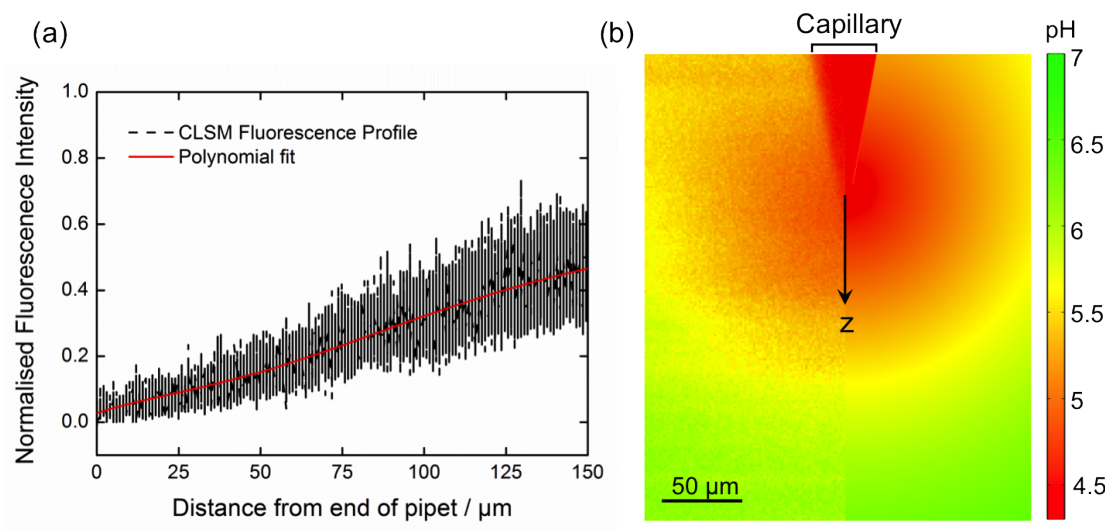


Figure 6.4: (a) Fluorescence intensity-distance plot normal to the end of the pipette extending into the bulk solution. The CLSM fluorescence profile and polynomial fit is shown for 100 mM propanoic acid. (b) Experimental (left) and simulated (right) pH profile for the permeation of 100 mM propanoic acid across the bilayer located at the end of the pipette. The weak acid containing solution in the pipette is at low pH to ensure all the weak acid is in the neutral form since the charged species is unable to permeate across the bilayer.

6.4 BILAYER CHARACTERISATION

The setup for bilayer formation and weak acid permeation visualisation is shown in Figure 6.5(a). After the formation of a lipid bilayer, suspended across the orifice of the pipette, the seal resistance was measured by recording current-voltage curves across the bilayer. The resistance varied over a fairly narrow range from $\sim 100 \text{ G}\Omega$ to $600 \text{ G}\Omega$, with an average value of $259 \pm 136 \text{ G}\Omega$ based on ~ 15 independent measurements on different bilayers. These values are comparable to those previously reported in the literature on similar sized apertures.^{43,45,48} Figure 6.5(b) shows typical i - V curves between the pipette and bulk solution,

before and after bilayer formation, with a typical increase in resistance of 5 orders of magnitude. For these measurements, the potential of one of the QRCEs in the pipette was swept whilst the current was recorded at the QRCE in the bulk solution (on the other side of the bilayer).

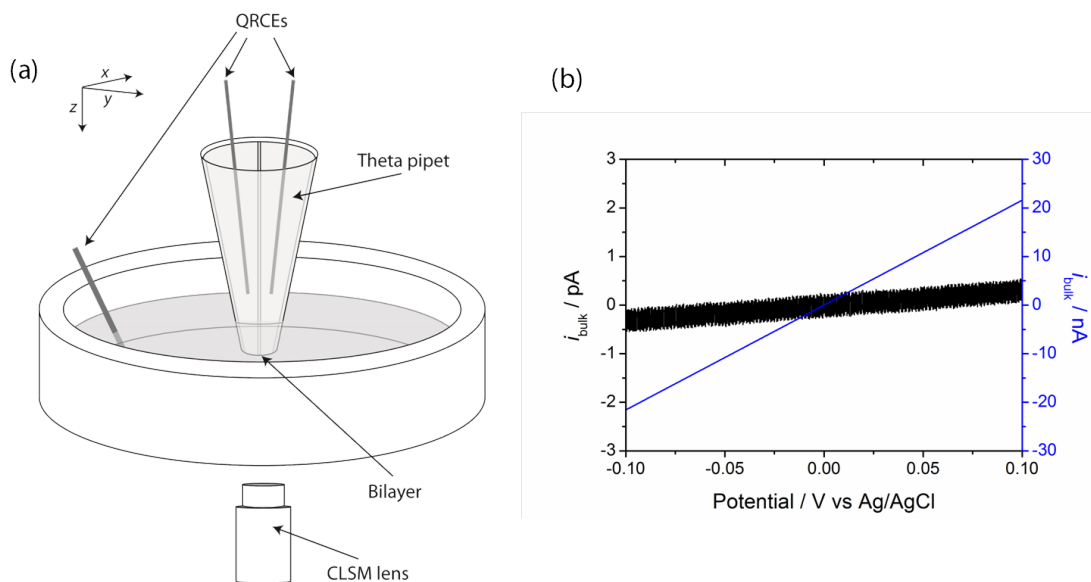


Figure 6.5: (a) Schematic illustration of the experimental setup for CLSM measurements. (b) Typical i - V curves for a $8 \mu\text{m}$ diameter pipette. The potential of one of the QRCEs in the pipette was swept and the resulting current was measured in the bulk solution before (blue line) and after (black line) bilayer formation. The open pipette and bilayer seal resistances are $4.6 \text{ M}\Omega$ and $330 \text{ G}\Omega$ respectively.

These bilayers offer several advantages compared to other methodologies, most notably the lack of residual solvent molecules within the bilayer. By forming the two monolayers individually, there is sufficient time for any solvent molecules to evaporate, which is expected to produce solvent-free bilayers when the two monolayers are brought into contact. The bilayers produced were often stable for several hours and under extreme potentials (from -1 to $+1 \text{ V}$). The absence of

residual solvent molecules is particularly advantageous for this study, since the passive permeation of small molecules greatly depends on the structure of the bilayer and any organic residues could affect the rate of transport.

6.5 VISUALISATION OF WEAK ACID TRANSPORT

The microscale bilayer system, in which a suspended bilayer is formed at the tip of a tapered pipette, is advantageous compared to many existing permeation systems since very high mass transport rates can be achieved. In contrast, in many previous studies permeation coefficients have typically been determined by measuring the flux of a permeant between two adjacent stirred chambers separated by a bilayer.⁶ Stirring increases the rate of mass transport of the permeant to the bilayer, but because of the restricted fluid flow at the interface there is a region where the rate of transport is dominated by diffusion. In this unstirred layer (USL), which is often difficult to define precisely, a diffusive gradient exists between the bulk concentration of the permeant and the concentration at the bilayer interface.⁴⁹ This layer can extend for several hundred microns on either side of the bilayer which causes significant resistance to the rates of permeation that can be measured, since the rate at which a molecule crosses the USL is generally much slower than the rate of permeation across the bilayer.^{2,50} Failure to correct for the USL can lead to large errors in the calculation of permeation coefficients and this appears to be a key factor in explaining the variation in reported permeation coefficients for the same molecules.^{3,51}

The method herein of using local pH changes to detect the rate of permeation

eliminates any USL problems, since the permeant is delivered directly to the bilayer, and the resulting fluorescence profile is generated in seconds unlike conventional proton titration, bulk pH or tracer molecule studies which can take several hours.^{7,8}

Figure 6.6 shows example profiles for the permeation of 10 mM butanoic and hexanoic acid across bilayers formed on pipettes with 8 μm diameter tip openings. It can clearly be seen that hexanoic acid has a significantly larger fluorescence profile than butanoic acid, and, since the concentration of the permeant and size of the pipette are consistent, the permeation coefficient must be higher in the hexanoic acid case, leading to a faster rate of interfacial transfer. In fact, when the fluorescence profiles for the rest of the series of acids at the same concentration are compared, there is a clear correlation between the permeation rate and acyl tail length, indicating that permeability increases with lipophilicity.

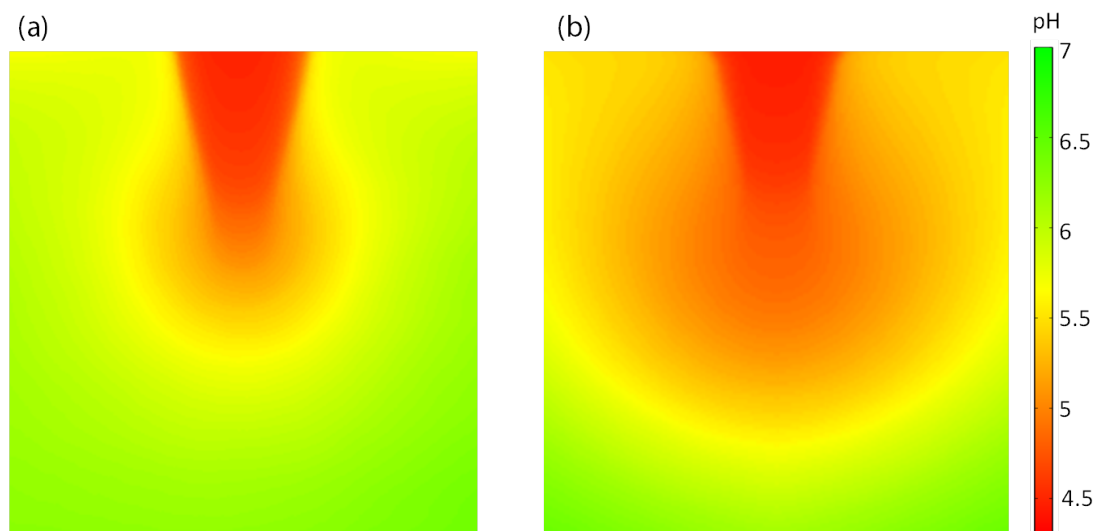


Figure 6.6: CLSM fluorescence intensity images showing the permeation of (a) 10 mM butanoic acid and (b) 10 mM hexanoic acid across a bilayer formed on 8 μm tip diameter pipettes.

6.6 QUANTITATIVE DETERMINATION OF PERMEATION COEFFICIENTS

As can be seen in Figure 6.7(a), when no weak acid is present there is sharp change in pH between the interior and exterior of the pipette. The experimental profile, however, shows a gradual increase in fluorescence from the end of the pipette, which is an artefact of CLSM imaging at this magnification. Light from outside the focal plane is not perfectly rejected, such that in the region around the end of the pipette the measured fluorescence is a combination of that from inside and outside the pipette. If this profile is compared to that of acetic acid, which shows the sharpest change in fluorescence between the inside and outside of the pipette, there is a clear difference between the two, and it is evident that this imaging artefact does not significantly affect the shape of the measured fluorescence profile over most of the distance (Figure 6.7(b)). However, in order to reduce the error in fitting a simulated profile to the experimental data, the first 25 μm of each of the profiles was discarded; after this point the profile with no weak acid has reached 90 % of its maximum value and so the contribution of this effect for further distances in the weak acid profiles can be assumed to be minimal.

To identify the permeation coefficient P for each weak acid, a series of simulated fluorescence profiles was produced from the FEM model to allow the best match to the experimental profile to be determined. P values were also chosen to fit the upper and lower bounds of two independent profiles from bilayers formed with different pipettes. As can be seen in Figure 6.8, the experimental profiles for each of the acids fit the simulated profiles well over this length scale. Further into the

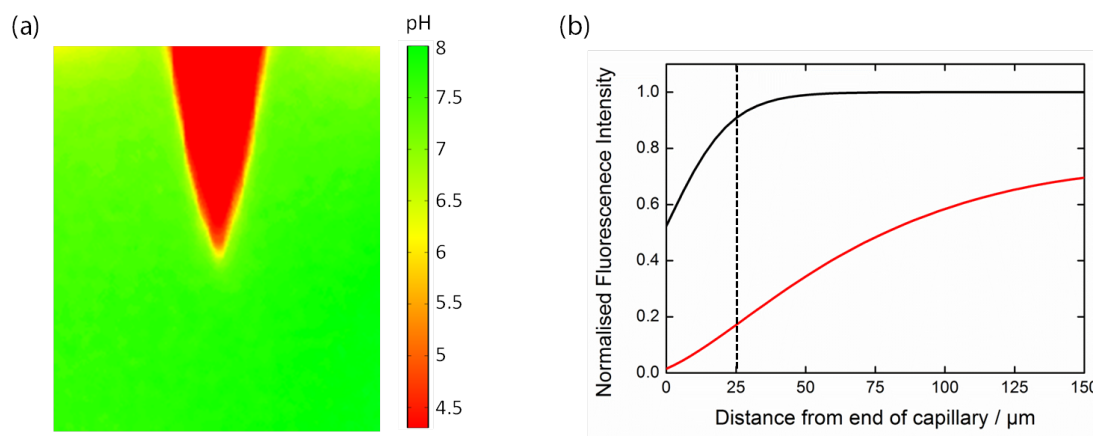


Figure 6.7: (a) CLSM image of a pipette containing only 0.1 M KCl at pH 4.2 after bilayer formation. (b) Fluorescence intensity profiles normal to the pipette orifice for the same pipette (black line) in comparison to that for 100 mM acetic acid at pH 4.2 (red line).

solution, the effects of natural convection will influence the process⁵² so only the first 150 μm of the profiles were considered.

As expected from visual inspection of the CLSM images, the permeation coefficients of each of the weak acids were found to monotonically increase with acyl tail length and partition coefficient, K , as can be seen in Figure 6.9. This finding supports the general trend of Overton's rule, which predicts that there is a correlation between P and K , but the relationship is more complex than expected, i.e. there is not a strict dependence of P and K .

The data presented here lies within the range of values reported previously (Table 6.3), although there is considerable variation between studies, which can be attributed to a number of factors. The composition of the bilayer controls its phase at room temperature, which, in turn, will affect the rate at which molecules permeate the bilayer. A bilayer formed from saturated lipids such as DPPC will be in the gel phase at room temperature and hence will give slower

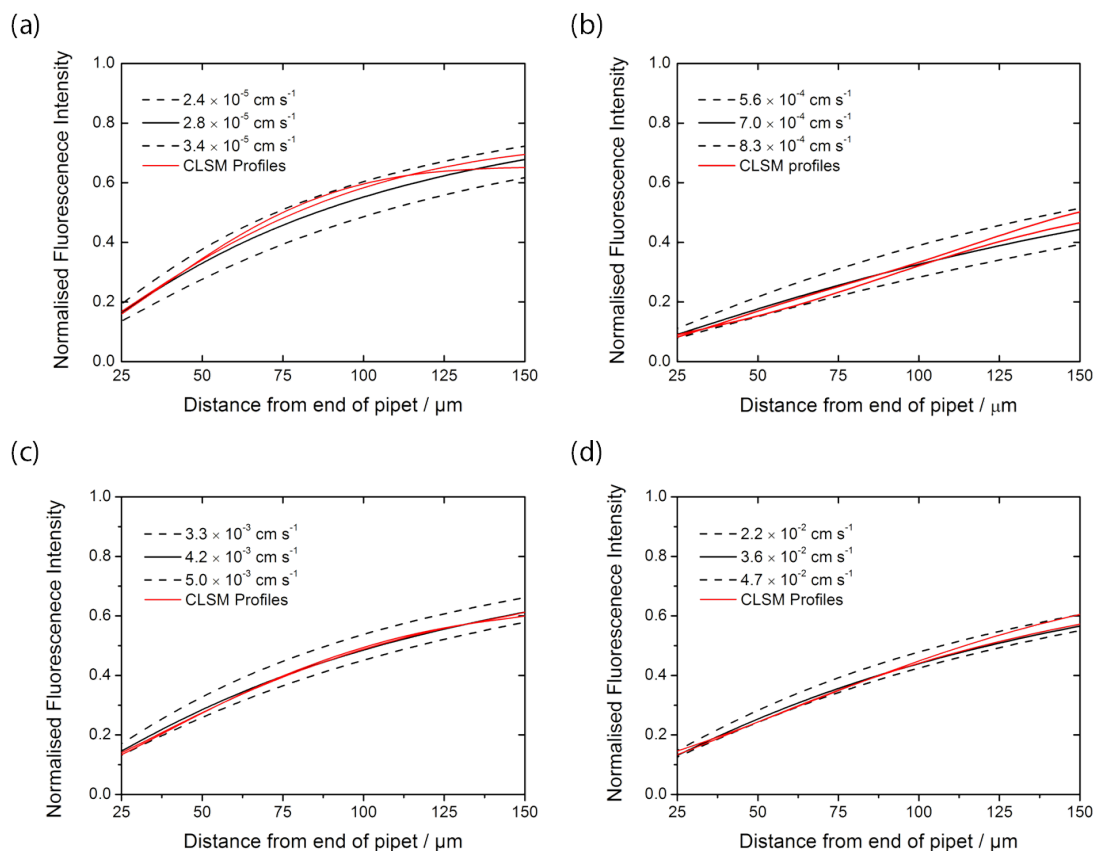


Figure 6.8: Experimental and corresponding simulated fluorescence-distance plot for (a) 100 mM acetic acid, (b) 100 mM propanoic acid, (c) 10 mM butanoic acid and (d) 10 mM hexanoic acid.

permeation rates than unsaturated bilayers, formed from, for example, soy or egg phosphatidylcholine (PC), which exist in the fluid phase. Additionally, for these lipids, the paintbrush method is typically used to form bilayers and consequently there will be residual organic solvent molecules within the bilayers which may affect the rate of transport.

Finally, for studies where an USL exists, its poorly defined nature means the accurate determination of permeation coefficients is extremely difficult and large

Table 6.3: Permeation coefficients (P) from previous weak acid permeation studies (units 10^{-2} cm s $^{-1}$).

| Weak Acid | Ref. 29 | Ref. 2 | Ref. 30 | Ref. 5 | This study (DPPC) | This study Soy PC |
|-----------------|----------------------------|--------|---------|--------|-------------------|-------------------|
| Acetic | 0.06 | 0.22 | 0.0028 | 0.66 | 0.0028 | 0.09 |
| Propanoic | 0.19 | - | 0.0025 | 2.6 | 0.070 | 0.26 |
| Butanoic | 0.72 | 0.089 | 0.0061 | 9.5 | 0.42 | 0.82 |
| Hexanoic | 23.0 | 0.0633 | - | 110 | 3.6 | - |
| Lipid | DPPC, DOPC and cholesterol | Soy PC | DPPC | Egg PC | DPPC | Soy PC |
| Temperature, °C | 22 ± 2 | 20 ± 2 | 30 | 22 ± 2 | 22 ± 2 | 22 ± 2 |

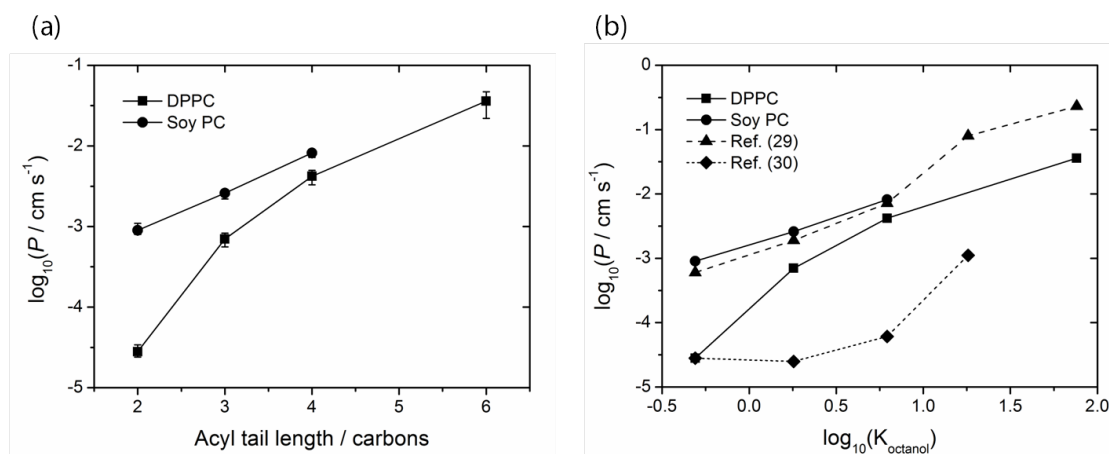


Figure 6.9: Plot of the permeation coefficient (P) of each weak acid across DPPC and soy PC bilayers vs. (a) acyl tail length and (b) water/octanol partition coefficient (K).

errors can easily be introduced.³ To assess what effect the structural phase of the bilayer had on permeability, preliminary experiments were carried out with soy PC which exists in the fluid phase at room temperature. From Figure 6.9(a) it is

evident that whilst the same trend in permeability is observed, the P values are higher than for DPPC bilayers, particularly for acetic and propanoic acid. This indicates that in the DPPC bilayers, there is a significant barrier to permeation of less lipophilic molecules due to the close packing of the saturated lipid tails in the interior of the bilayer. The differences between P values for DPPC and soy PC bilayers, however, do not represent the full range of values reported in the literature, indicating that the variation is not solely due to bilayer structure.

In addition to the wide range of permeation coefficients reported for the same molecules, there has been considerable debate as to whether the qualitative relationship predicted by Overton's rule is accurate. Previous work from the Warwick group demonstrated a *decreasing* trend in permeability with lipophilicity, in contrast to the results presented herein, and most other existing data.² However, some studies also reported decreasing permeability with lipophilicity, for at least some of the weak acids in the series.^{4,30} Whilst the phase of the lipid bilayer and USL effects may account for the discrepancies in these studies, other factors must be considered for the data presented by Grime *et al.*. The bilayers used were formed via the painting method, introducing the possibility that organic solvent molecules within the bilayer could affect the measured permeation rates. Additionally, using a UME to electrogenerate the weak acid molecule at the bilayer interface may not be as well defined a process as expected (as discussed in Chapter 7), and the resulting electric field arising during this process could affect the structure of the bilayer, influencing its permeability.

The novel method of bilayer formation and measurement of permeation

coefficients described in this chapter eliminates virtually all of the sources of error listed above, providing an extremely reliable set of data from which to draw conclusions. The bilayers produced contain no residual solvent molecules, and the weak acid molecules are delivered directly to the bilayer interface, so that the measured permeation rates are not influenced by USL effects or any factors associated with the electrogeneration of the weak acid by a UME.

To assess the exact relationship between P and K , the water/octanol partition coefficients and measured permeation coefficients have been plotted for this work and previous studies also using DPPC (Figure 6.9(b)). The partition coefficient is a measure of how readily a molecule will dissolve in an aqueous phase compared to an organic phase, and as such is a measure of the lipophilicity of a molecule. Overton's rule states that there is a correlation between P and K , i.e. more lipophilic molecules will permeate more readily, since they are more soluble in the organic phase. However, the lipid bilayer contains both hydrophilic and hydrophobic moieties, which Overton's rule does not account for.

Our DPPC data shows a strong linear trend with the exception of acetic acid which is lower than would be expected based on Overton's rule. This observation could attributed to the gel phase structure of the bilayer creating a greater energy barrier for the permeation of the more hydrophilic molecule, compared to those with longer acyl tails.⁵³ Li and co-workers, avoided this issue by using a mixture of lipids to ensure the bilayers were in the liquid phase and which explains their reported higher permeation coefficients.²⁹ Our soy PC data correlate exceptionally well with the partition coefficients and the P values are in excellent agreement with previous work.

6.7 EFFECTS OF POTENTIAL FIELD ON PERMEABILITY

One other application of this bilayer system is in the study of potential field effects on the rate of transport of molecules. Potential fields have been shown to increase the rate of transport of ions across the membrane via the formation of pores within the membrane.^{54,55} These pores may provide an additional route to permeation and therefore increase the permeation rates of molecules through bilayers held under a potential field. Figure 6.10 shows CLSM profiles of 5 mM hexanoic acid permeating across bilayers at potentials of 0 V, 0.5 V and 1 V with the potential applied to one of the QRCEs in the pipette. As can be seen visually, there is a small increase in permeability with increasing potential, supporting the idea that the potential field disrupts the membrane. Analysis of these profiles gives permeation coefficients of $6.5 \times 10^{-3} \text{ cm s}^{-1}$ at 0 V, $8.1 \times 10^{-3} \text{ cm s}^{-1}$ at 0.5 V and $13 \times 10^{-3} \text{ cm s}^{-1}$ at 1 V showing a two-fold increase in permeability from 0 to 1 V.

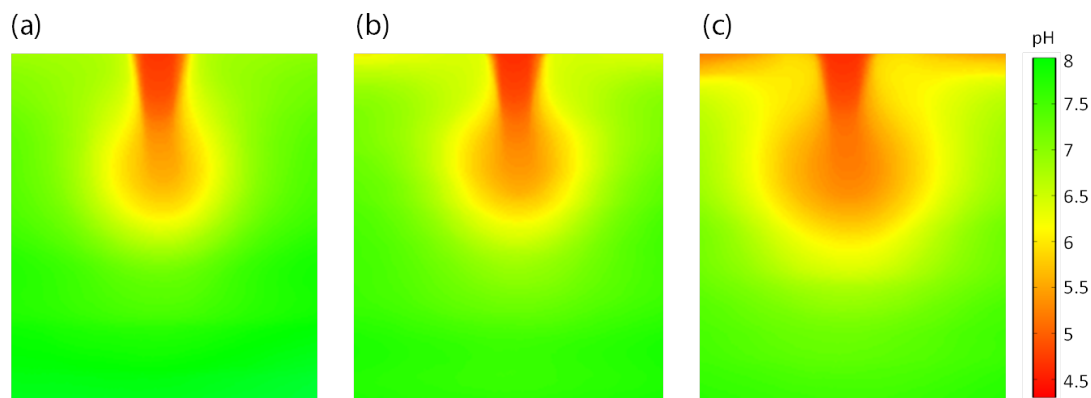


Figure 6.10: CLSM fluorescence intensity images showing the permeation of 5 mM hexanoic acid at potentials of (a) 0 V, (b) 0.5 V and (c) 1 V vs. Ag/AgCl.

The experiment was repeated with propanoic acid, yielding P values of 1.9×10^{-4} cm s⁻¹ at 0.1 V, 2.3×10^{-4} cm s⁻¹ at 0.5 V, and 3.1×10^{-4} cm s⁻¹ at 1 V (Figure 6.11), indicating that the effect of the potential field on permeability is not influenced by the lipophilicity of the molecule.

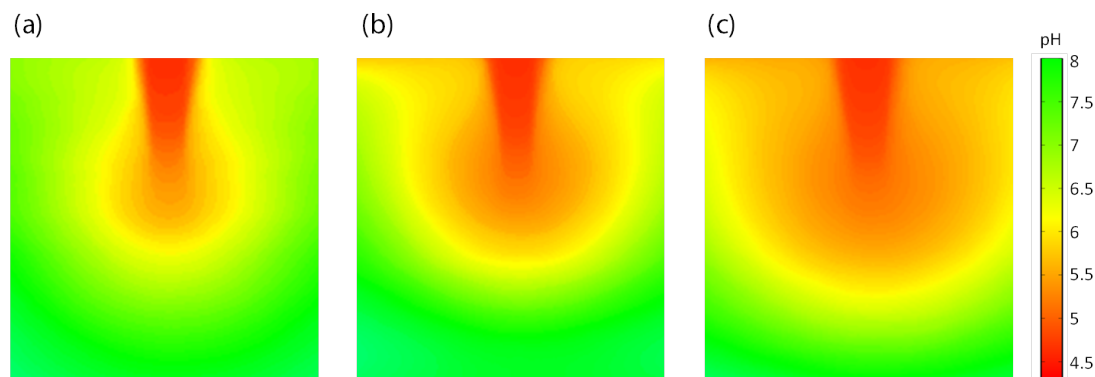


Figure 6.11: CLSM fluorescence intensity images showing the permeation of 100 mM propanoic acid at potentials of (a) 0.1 V, (b) 0.5 V and (c) 1 V vs. Ag/AgCl.

6.8 CONCLUSIONS

This new method of suspended BLM fabrication allows for the rapid formation of solvent-free bilayers which are durable over long time periods, stable under extreme potentials and exhibit extremely high seal resistances. Each monolayer is assembled individually allowing volatile residual solvent molecules to evaporate before the bilayer is formed. Here, this property has been exploited to investigate the permeability of a series of carboxylic acids across these solvent-free bilayers. By monitoring the change in fluorescence intensity of a pH-sensitive fluorophore, local pH changes can be visualised as these acids permeate across the bilayers. A clear trend is observable from the fluorescence images, with the more lipophilic

acids showing larger changes in pH and therefore faster permeation rates. However, accurate permeation coefficients can be extracted from this data by fitting to simulated fluorescence profiles generated by the FEM model. There is an increase in permeation coefficient with partition coefficient, although the relationship does not strictly follow Overton's rule. Comparison of the data from DPPC and soy PC bilayers indicates that the composition of the bilayer does not affect this trend, i.e. the phase in which the lipids exist does not affect permeation rates, at least qualitatively, although higher permeation coefficients are observed for bilayers formed from lipids in the fluid phase.

The effects of potential fields on permeation rate have also been investigated which show slightly increased rates of transport for more positive potentials which can be attributed to the formation of pores in the membrane induced by the potential field.

Since weak acids and bases are commonly used in pharmaceuticals, the technique is of considerable value in analysing permeation rates of these molecules to determine how particular molecular characteristics influence rates of transport. This could also be coupled with further investigations into the effects of potential fields on permeation to enhance the delivery of these molecules into cells. Additionally, there are potential applications for these bilayers in asymmetric bilayer studies due to the individual formation of each monolayer, and also in ion-channel measurements due to their high seal resistances. Furthermore, the ability to control the size of the pipette tip opening would allow the system to be optimised for single ion-channel recordings for possible applications as biosensors, where nanometre sized apertures are highly beneficial.^{17,43}

6.9 REFERENCES

- [1] Mueller, P.; Rudin, D. O.; Tien, H.; Wescott, W. C. *Nature* **1962**, *194*, 979.
- [2] Grime, J. M. A.; Edwards, M. A.; Rudd, N. C.; Unwin, P. R. *Proceedings of the National Academy of Sciences* **2008**, *105*, 14277–14282.
- [3] Walter, A.; Hastings, D.; Gutknecht, J. *The Journal of General Physiology* **1982**, *79*, 917–933.
- [4] Walter, A.; Gutknecht, J. *Journal of Membrane Biology* **1984**, *77*, 255–264.
- [5] Evtodienko, V. Y.; Kovbasnjuk, O. N.; Antonenko, Y. N.; Yaguzhinsky, L. S. *Biochimica et Biophysica Acta (BBA) - Biomembranes* **1996**, *1281*, 245–251.
- [6] Missner, A.; Kagler, P.; Saparov, S. M.; Sommer, K.; Mathai, J. C.; Zeidel, M. L.; Pohl, P. *Journal of Biological Chemistry* **2008**, *283*, 25340–25347.
- [7] Wolosin, J.; Ginsburg, H. *Biochimica et Biophysica Acta (BBA) - Biomembranes* **1975**, *389*, 20–33.
- [8] Walter, A.; Gutknecht, J. *Journal of Membrane Biology* **1986**, *90*, 207–217.
- [9] Orbach, E.; Finkelstein, A. *The Journal of General Physiology* **1980**, *75*, 427–436.
- [10] Sugawara, M.; Hirano, A.; Bühlmann, P.; Umezawa, Y. *Bulletin of the Chemical Society of Japan* **2002**, *75*, 187–201.
- [11] Matsuno, Y.; Osono, C.; Hirano, A.; Sugawara, M. *Analytical Sciences* **2004**, *20*, 1217–1221.
- [12] Heitz, B. A.; Xu, J.; Hall, H. K.; Aspinwall, C. A.; Saavedra, S. S. *Journal of the American Chemical Society* **2009**, *131*, 6662–6663.

-
- [13] Ide, T.; Kobayashi, T.; Hirano, M. *Analytical Chemistry* **2008**, *80*, 7792–7795.
- [14] Hanke, W.; Methfessel, C.; Wilmsen, U.; Boheim, G. *Bioelectrochemistry and Bioenergetics* **1984**, *12*, 329–339.
- [15] Hirano, A.; Sugawara, M.; Umezawa, Y.; Uchino, S.; Nakajima-Iijima, S. *Biosensors and Bioelectronics* **2000**, *15*, 173–181.
- [16] Uto, M.; Michaelic, E. K.; Hu, I. F.; Umezawa, Y.; Kuwana, T. *Analytical Sciences* **1990**, *6*, 221–225.
- [17] Bayley, H.; Cremer, P. S. *Nature* **2001**, *413*, 226.
- [18] Gu, L. Q.; Braha, O.; Conlan, S.; Cheley, S.; Bayley, H. *Nature* **1999**, *398*, 686.
- [19] Shim, J. W.; Gu, L. Q. *Analytical Chemistry* **2007**, *79*, 2207–2213.
- [20] Guan, X.; Gu, L.-Q.; Cheley, S.; Braha, O.; Bayley, H. *ChemBioChem* **2005**, *6*, 1875–1881.
- [21] Braha, O.; Gu, L. Q.; Zhou, L.; Lu, X.; Cheley, S.; Bayley, H. *Nature Biotechnology* **2000**, *18*, 1005.
- [22] Kasianowicz, J.; Brandin, E.; Branton, D.; Deamer, D. *Proceedings of the National Academy of Sciences* **1996**, *93*, 13770–13773.
- [23] Vercoutere, W.; Winters-Hilt, S.; Olsen, H.; Deamer, D.; Haussler, D.; Akeson, M. *Nature Biotechnology* **2001**, *19*, 248.
- [24] Chen, X.; Murawski, A.; Patel, K.; Crespi, C.; Balimane, P. *Pharmaceutical Research* **2008**, *25*, 1511–1520.
- [25] Kansy, M.; Senner, F.; Gubernator, K. *Journal of Medicinal Chemistry* **1998**, *41*, 1007–1010.
- [26] Sugano, K.; Nabuchi, Y.; Machida, M.; Aso, Y. *International Journal of Pharmaceutics* **2003**, *257*, 245–251.

-
- [27] Overton, C. *Vierteljahrsschrift der Naturforschenden Gesellschaft in Zurich* **1899**, *44*, 88–135.
- [28] Overton, C. *Studies in Narcosis*; Fischer, Jena, Germany, 1901.
- [29] Li, S.; Hu, P.; Malmstadt, N. *Biophysical Journal* **2011**, *101*, 700–708.
- [30] Xiang, T.-X.; Anderson, B. D. *Biophysical Journal* **1998**, *75*, 2658–2671.
- [31] Mueller, P.; Rudin, D. O.; Tien, H. T.; Wescott, W. C. *The Journal of Physical Chemistry* **1963**, *67*, 534–535.
- [32] Moscho, A.; Orwar, O.; Chiu, D. T.; Modi, B. P.; Zare, R. N. *Proceedings of the National Academy of Sciences* **1996**, *93*, 11443–11447.
- [33] Montal, M.; Mueller, P. *Proceedings of the National Academy of Sciences* **1972**, *69*, 3561–3566.
- [34] Coronado, R.; Latorre, R. *Biophysical Journal* **1983**, *43*, 231–236.
- [35] Ide, T.; Yanagida, T. *Biochemical and Biophysical Research Communications* **1999**, *265*, 595–599.
- [36] Malmstadt, N.; Jeon, T.-J.; Schmidt, J. J. *Advanced Materials* **2008**, *20*, 84–89.
- [37] Lu, X.; Ottova, A. L.; Tien, H. *Bioelectrochemistry and Bioenergetics* **1996**, *39*, 285–289.
- [38] Beddow, J. A.; Peterson, I. R.; Heptinstall, J.; Walton, D. J. *Analytical Chemistry* **2004**, *76*, 2261–2265.
- [39] Jeon, T.-J.; Malmstadt, N.; Schmidt, J. J. *Journal of the American Chemical Society* **2006**, *128*, 42–43.
- [40] Hirano, M.; Kobayashi, T.; Ide, T. *e-Journal of Surface Science and Nanotechnology* **2008**, *6*, 130–133.
- [41] Li, S.; Hu, P.; Malmstadt, N. *Analytical Chemistry* **2010**, *82*, 7766–7771.

-
- [42] Wonderlin, W.; Finkel, A.; French, R. *Biophysical Journal* **1990**, *58*, 289–297.
- [43] White, R. J.; Ervin, E. N.; Yang, T.; Chen, X.; Daniel, S.; Cremer, P. S.; White, H. S. *Journal of the American Chemical Society* **2007**, *129*, 11766–11775.
- [44] Schibel, A. E. P.; Edwards, T.; Kawano, R.; Lan, W.; White, H. S. *Analytical Chemistry* **2010**, *82*, 7259–7266.
- [45] Schibel, A. E. P.; Heider, E. C.; Harris, J. M.; White, H. S. *Journal of the American Chemical Society* **2011**, *133*, 7810–7815.
- [46] Saparov, S. M.; Antonenko, Y. N.; Pohl, P. *Biophysical Journal* **2006**, *90*, L86–L88.
- [47] Davies, C. *Ion Association*; Butterworths, 1962.
- [48] Fertig, N.; Meyer, C.; Blick, R. H.; Trautmann, C.; Behrends, J. C. *Physical Review E* **2001**, *64*, 040901.
- [49] Barry, P. H.; Diamond, J. M. *Physiological Reviews* **1984**, *64*, 763–872.
- [50] Korjamo, T.; Heikkinen, A. T.; Monkkonen, J. *Journal of Pharmaceutical Sciences* **2009**, *98*, 4469–4479.
- [51] Antonenko, Y.; Denisov, G.; Pohl, P. *Biophysical Journal* **1993**, *64*, 1701–1710.
- [52] Rudd, N. C.; Cannan, S.; Bitziou, E.; Ciani, I.; Whitworth, A. L.; Unwin, P. R. *Analytical Chemistry* **2005**, *77*, 6205–6217.
- [53] Xiang, T.; Anderson, B. *Biophysical Journal* **1997**, *72*, 223–237.
- [54] Weaver, J. C.; Chizmadzhev, Y. *Bioelectrochemistry and Bioenergetics* **1996**, *41*, 135–160.
- [55] Kinoshita, K.; Ashikawa, I.; Saita, N.; Yoshimura, H.; Itoh, H.; Nagayama, K.; Ikegami, A. *Biophysical Journal* **1988**, *53*, 1015–1019.

CHAPTER 7

INVESTIGATION OF THE LATERAL DIFFUSION OF PROTONS AT SURFACES USING CONFOCAL LASER SCANNING MICROSCOPY COUPLED WITH SECM AND FEM SIMULATIONS

In this chapter, a combined CLSM-SECM technique is used to investigate the interaction of protons with different substrates. Protons are generated galvanostatically via the oxidation of water, due to the application of an anodic current to a Pt UME. This process elicits a change in the local pH, which is monitored via a pH-sensitive fluorophore, and a series of CLSM fluorescence profiles are captured over time. In order to quantitatively analyse the data, a FEM simulation has been developed, which models both the proton-substrate affinity, and lateral diffusion of the protons along the substrate surface. By comparing these simulated profiles to the experimental data, the interaction of protons with inert (poly-L-lysine) and negatively charged (poly-L-glutamic acid) substrates can be quantified, and the lateral diffusion coefficient of protons along an egg PC bilayer can be extracted. The quantification of the interaction of protons with these surfaces demonstrates that FEM simulations can be a powerful tool for determining experimental parameters that would otherwise be inaccessible by experimental techniques. Moreover, discrepancies observed between experimental and simulated data can provide insights into how both the experimental setup and FEM model can be optimised.

7.1 INTRODUCTION

The movement of protons between sites in biological membranes is of fundamental importance to many bioenergetic processes.¹ Lateral diffusion of the protons along the membrane surface represents the most efficient mechanism of transport, however, there has been considerable debate as to the extent to which this pathway operates.²⁻⁴ The process of proton transfer in biological systems is of critical importance, as the movement of protons drives bioenergetic processes in mitochondria, chloroplasts and bacteria. Oxidative phosphorylation occurs in the membranes of each, and is the process by which all cells derive their energy. It relies on the translocation of protons, generating a proton gradient, which, when coupled with an electric potential gradient, generates a “protonmotive force” according to the chemiosmotic theory proposed by Mitchell.⁵ Protons move down this gradient, through the enzyme adenosine triphosphate (ATP) synthase, which uses the potential energy of the protons to drive the synthesis of ATP. Whilst the translocation of protons across the membrane is facilitated by a series of enzymes, there are competing theories about the mechanism of lateral transport between enzymes along the membrane.⁶⁻⁸

A number of experimental techniques have been used to study this phenomenon, many of which involve the use of a fluorescent probe such as fluorescein. By covalently attaching this molecule to the surface of the membrane at a particular location, it can be used to monitor the local change in pH as protons are introduced at a separate position on the membrane. For example, in some of the early studies by Teissié *et al.*, acid solution was injected into the system, and the change in

fluorescence of the fluorescein was monitored several centimetres away.^{3,9} More recently, a modified version of this technique has been used, whereby a micropipette is used for acid/base injection, allowing measurement of proton diffusion over much smaller length scales.¹⁰

Alternatively, excited-state proton emitter molecules can be used as a proton source, which release a proton upon excitation with a laser pulse.¹¹ Finally, photochemically active membrane proteins such as bacteriorhodopsin will undergo a photochemical reaction cycle upon excitation with a light pulse, releasing protons from a fixed position in the membrane. This allows spatial and temporal monitoring of proton transfer to the surface-bound pH indicator molecules also present within the membrane.^{4,12}

Electrochemical methods have also been used to study lateral proton diffusion. Using an SECM setup, the tip-current can be recorded as the UME is positioned close to a Langmuir monolayer whilst driving the reduction of H^+ .¹³ This current can then be analysed to determine the rate of diffusion of protons along the surface of the monolayer, to replace those consumed at the electrode. Conductivity measurements in the proximity of a Langmuir monolayer have also been used, which record the change in conductivity as the monolayer is compressed. From this, conclusions about lateral diffusion within the monolayer can be drawn.¹⁴

There are a number of processes that must be considered when studying lateral proton diffusion. Firstly, the transport of protons in bulk solution is unlike any other ion, since they diffuse by the Grotthuss mechanism (Figure 7.1).¹⁵ This mechanism describes how the hydrogen bonds between neighbouring water

molecules within the solvation shell of the H_3O^+ ion become covalent bonds as the charge of the proton is displaced along this network.

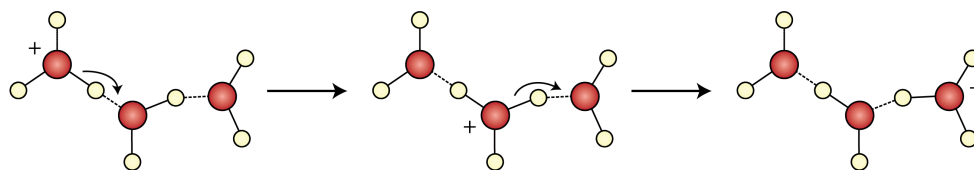


Figure 7.1: Illustration of the Grotthuss mechanism of proton transport through aqueous solution.¹⁵

Secondly the interaction of the protons with the membrane surface must be considered. Previous work has shown that protons diffuse over much longer distances than would be expected from the average lifetime of the proton on the surface based on its $\text{p}K_{\text{a}}$ value.¹⁶ Cherepanov *et al.* have proposed that this phenomenon is due to a potential barrier at the membrane surface resulting from the low dielectric permittivity of water in this region, which causes protons to remain close to the membrane.¹⁷ In this work, the effect of mobile buffer molecules in solution on the interfacial energy barrier was investigated, showing that the electric charge on the buffer affected the rate of proton equilibration between the bulk solution and the surface, by altering the height of the energy barrier above the surface.¹⁸ These observations are in agreement with previous work, demonstrating the influence of mobile buffers on lateral diffusion coefficients.¹⁹

The fixed buffers on the membrane surface must also be taken into account, since the movement of protons along the membrane is often treated as a series of binding

and release events between these groups. These include the headgroups of the phospholipids and other ionizable groups present in the membrane. These groups are typically spaced 5-10 Å apart, precluding direct proton transfer between them. The “jump” model, in which a proton dissociates from one group and diffuses and binds to the next, predicts considerably lower diffusion coefficients than are observed, indicating that this explanation of proton diffusion does not accurately describe the process occurring.²⁰

One alternative theory suggests that the overlapping Coulomb cages of the different groups may give rise to a continuous potential well in which the proton can diffuse unhindered, or that they are connected by water wires, along which protons may travel.²¹ In either case, the pK_a of these groups would be expected to have a significant impact on lateral diffusion rates. However, Springer *et al.* have recently presented data indicating that, in fact, the pK_a of the surface has very little impact on lateral diffusion rates. Furthermore, they demonstrated that replacing H₂O in the system with D₂O significantly reduces the lateral diffusion coefficient of protons, indicating that transport occurs predominantly via an interfacial water layer.²⁰

A number of approaches have been utilised in modelling the lateral diffusion of protons, with varying levels of complexity. Antonenko and Pohl used simple, analytical solutions to the 2D and 3D diffusion equations to model the change in fluorescence at a specific point on the membrane after the injection of protons.¹⁰ This simple approach can be extended by adding a term describing the adsorption and desorption of the protons onto and off the membrane surface which can include contributions from both fixed buffers on the membrane

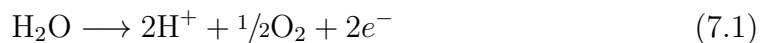
surface, and mobile buffers in the aqueous solution. The adsorption of protons onto fixed sites on the membrane can be modelled with an array of proton collecting antenna of a finite radius, between which, protons diffuse laterally.^{21,22} The exchange of protons between the aqueous solution and proton antenna can be modelled as a rapid or slow process, affecting the dwell time of the protons on the surface and consequently influencing whether proton diffusion at the surface can be considered as being decoupled from the bulk.¹⁶ Finally, the effects of the potential barrier can also be included, which affect the adsorption and desorption rates of the protons onto the membrane surface.¹⁸

In this chapter, a FEM model is developed to model the interaction of protons with a number of different substrates. Combining electrochemical and fluorescence techniques, the local pH close to different surfaces was observed by means of the pH-sensitive fluorophore fluorescein. Protons were generated galvanostatically via the oxidation of water, and the adsorption and lateral diffusion of these protons gave rise to different pH profiles. Using FEM simulations, it is possible to quantify the rates of these processes at different substrates.

7.2 SECM-CLSM PRINCIPLES

For each substrate studied herein, the same experimental procedure was used to study changes in the distribution of protons in the system over time. To generate protons, a two electrode galvanostatic setup was used with a platinum reference electrode and a 25 μm diameter UME working electrode (fabricated using procedures described previously²³) positioned 20 μm above the substrate using a

piezoelectric positioner. An anodic current between 0.5 and 2 nA was applied to the UME via a home-built galvanostat, producing a proton flux from the oxidation of water:



The aqueous solution contained the pH-sensitive fluorophore fluorescein, the fluorescence intensity of which is high in alkaline, and low in acidic environments. The pH of the bulk solution was adjusted to 7.8 so that the initial fluorescence intensity was high (approximately 90% of the maximum intensity, see Figure 7.3). As the anodic current was applied to the UME, generating protons, the pH around the tip decreased, causing a reduction in fluorescence intensity. Using the confocal laser scanning microscope, line scans were taken at the midpoint between the substrate and UME every 2 ms, recording the change in fluorescence intensity over time. Figure 7.2 shows the experimental setup indicating the positioning of the UME and CLSM lens with respect to the substrate. For each line scan recorded after the application of the anodic current, the fluorescence intensity was lowest directly beneath the Pt tip, gradually increasing with increasing distance from the centre of the UME. Over longer time periods, the fluorescence intensity beneath the UME decreased as the proton concentration increased, and a faster change in this intensity was observed at higher currents, as the flux of protons increased more rapidly.

The spread of these fluorescence profiles can be used to quantify the proton-substrate interaction, since adsorption of the protons onto the surface will reduce the spread of the fluorescence profile. In order to analyse these profiles, a

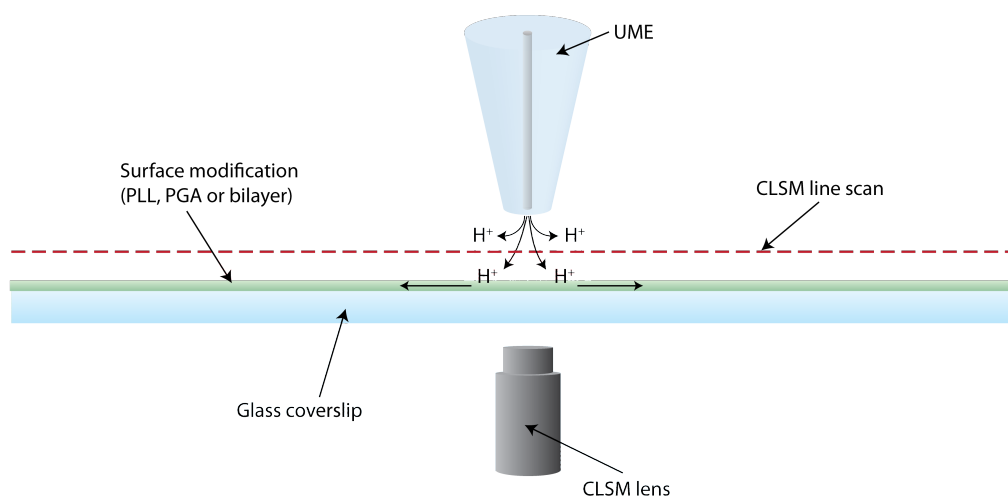


Figure 7.2: Schematic of the experimental setup for CLSM studies of proton adsorption/diffusion (not to scale).

calibration curve was recorded by measuring the fluorescence intensity at a range of different pH values (Figure 7.3). A Boltzmann fit was applied to the data to give an analytical expression for the relationship, and the pH value at which the half-maximum fluorescence intensity occurred was determined. Using this value, each line profile was analysed to find the distance from the centre of the UME at which the pH was equal to this value. Analysing each line profile in this way produced a spatio-temporal plot of distance at which the half-maximum fluorescence intensity occurred against time.

7.3 THEORY AND SIMULATIONS

With the aid of FEM simulations, the CLSM fluorescence profiles presented herein can be quantified to determine quantitative information about the

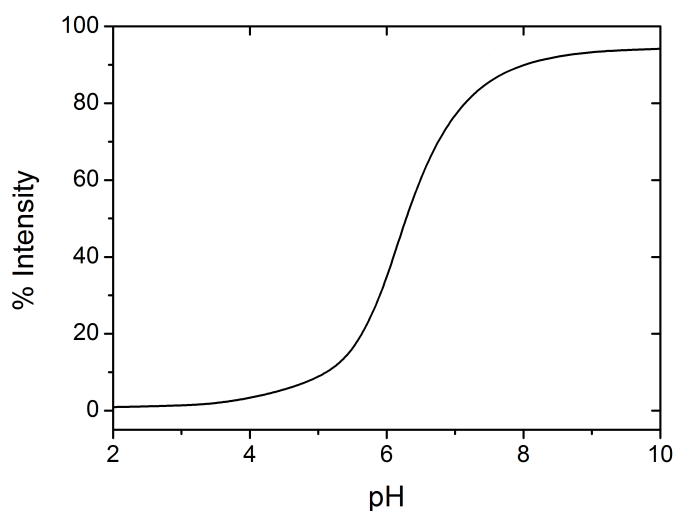


Figure 7.3: Calibration curve showing the change in normalised fluorescence intensity with pH.

different substrates, and the means by which protons interact with them. Whilst the only species of interest in the simulation is H^+ , there are others which must be taken into account. The water equilibrium:



will buffer the solution to some extent and may affect the resulting pH changes. To assess the extent of this effect, simulations were run with and without the water equilibrium with the concentration of each species corrected for the ionic activity of the solution (0.1 M KNO_3) using the Davies equation (Figure 7.4).²⁴ As can be seen, the presence of this equilibrium has only a very small effect on the resulting profile, and was therefore not included in all other simulations for computational efficiency.

Fluorescein is also present in solution to monitor changes in pH and exists in

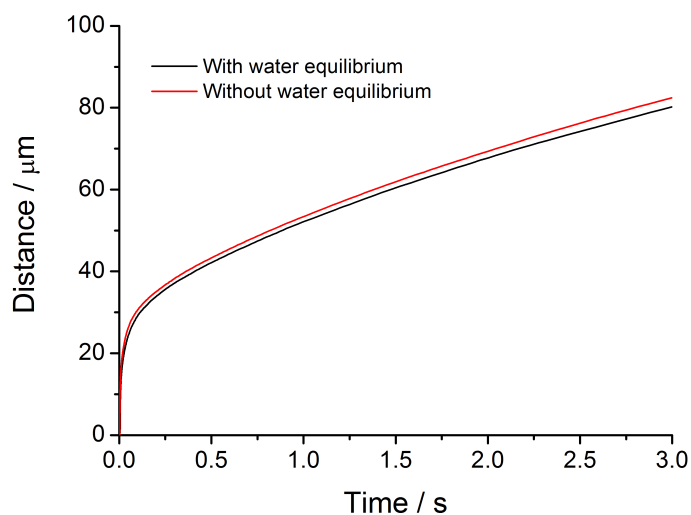
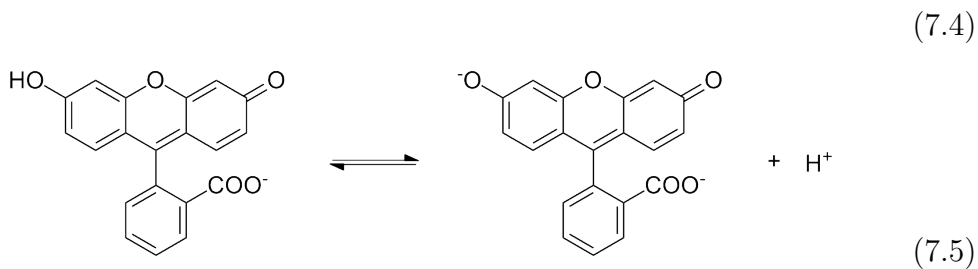
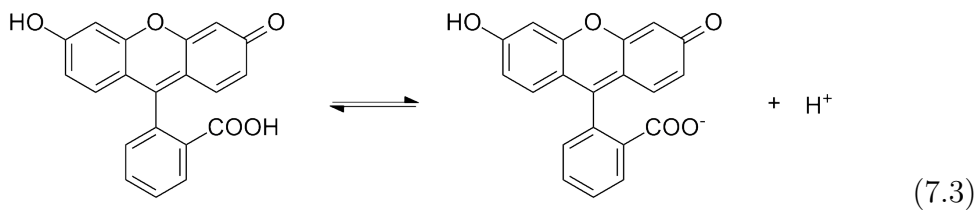


Figure 7.4: Simulated spatio-temporal plots of the half-maximum fluorescence intensity for an inert surface, with and without the inclusion of the water equilibrium.

three states of protonation depending on the pH of the surrounding solution (as described in section 1.6.2):



However, as for the water equilibrium, inclusion of these equilibria had little effect on the results of the simulations, due to the low concentration of fluorescein present

in solution.

In order to simulate the distribution of protons within the system over time, an axisymmetric simulation domain with length 5 mm and height 5 mm was constructed. The UME was modelled as a 12.5 μm radius Pt wire surrounded by a glass sheath (radius 125 μm). The initial concentration of protons was calculated from the bulk pH value, and the diffusion coefficient was set as $7.6 \times 10^{-5} \text{ cm}^2 \text{ s}^{-1}$, which is appropriate for the experimental conditions used.²⁵

To calculate the concentration of protons within this domain, the following time-dependent reaction-diffusion equation was solved in the axisymmetrical cylindrical geometry appropriate to SECM:

$$\frac{\partial c}{\partial t} = D \left(\frac{\partial^2 c}{\partial r^2} + \frac{1}{r} \frac{\partial c}{\partial r} + \frac{\partial^2 c}{\partial z^2} \right) + R \quad (7.6)$$

where c , D and R are the concentration, diffusion coefficient and rate of production of protons respectively, and r and z are the radial and normal coordinates with respect to the centre of the UME. Protons are galvanostatically generated at the Pt UME tip, with the resulting flux reasonably described by Equation 7.7

$$J = \frac{i_{\text{app}}}{nAF} \quad (7.7)$$

where i_{app} is the applied current, n is the number of electrons transferred (in this case, 1) and A is the area of the electrode.

The extent to which protons adsorb onto or desorb from the substrate is dependent on the surface potential, ψ_0 , which can be determined from the Gouy-Chapman

model²⁶

$$\sigma_0 = (8\epsilon\epsilon_0RTI)^{1/2} \sinh\left(\frac{F\psi_0}{2RT}\right) \quad (7.8)$$

where σ_0 is the charge density, ϵ is the dielectric constant, ϵ_0 is the permittivity of free space, R is the gas constant, T is the temperature and I is the ionic strength of the supporting electrolyte.

This charge density will be dependent on the proportion of surface sites which are protonated:

$$\sigma_0 = F\theta N \quad (7.9)$$

where θ is the proportion of unprotonated surface sites and N is the total concentration of these sites.

The rate constants for the adsorption and desorption processes are given by the following expressions, which can be written in terms of intrinsic parameters, independent of the surface potential:²⁶

$$k_a = k_a^i \exp\left(\frac{F\psi_0}{2RT}\right) \quad (7.10)$$

$$k_d = k_d^i \exp\left(\frac{-F\psi_0}{2RT}\right) \quad (7.11)$$

The intrinsic adsorption and desorption rate constants are related to the pK_a of the surface functional groups:

$$k_d^i = k_a^i \times 10^{-pK_a} \quad (7.12)$$

Coupling the adsorption/desorption process with lateral diffusion at the surface, gives the boundary condition which is applied to the substrate

$$D \frac{\partial c}{\partial z} = -k_d \theta + k_a (1 - \theta) c \quad (7.13)$$

with the time dependence of theta given by

$$N \frac{\partial \theta}{\partial t} = N D_{\text{surf}} \left[\frac{\partial^2 \theta}{\partial r^2} + \frac{1}{r} \frac{\partial \theta}{\partial r} \right] - k_d \theta + k_a (1 - \theta) c \quad (7.14)$$

The reaction-diffusion equation (Equation 7.6) is solved subject to the boundary conditions of the system to produce a profile of the proton concentration over time. In order to compare this profile to the experimental data, the $[\text{H}^+]$ profile is converted into a pH profile and a line profile is extracted for each time point, 10 μm above the substrate. This data is further analysed by finding the horizontal distance along the line profile at which the fluorescence intensity is at half its maximum value, which corresponds to a pH of 6.1 based on calibration curves obtained for the system (Figure 7.3).

7.4 VISUALISATION OF PROTON INTERACTION WITH MODIFIED SUBSTRATES

7.4.1 CASE 1: POLY-L-LYSINE

The FEM model was first parameterised to simulate the case of an inert surface, corresponding to the poly-L-lysine (PLL) modified substrate used for the

experiments. The chemical structure of PLL is shown in Figure 7.5 along with PGA, studied in the next section.

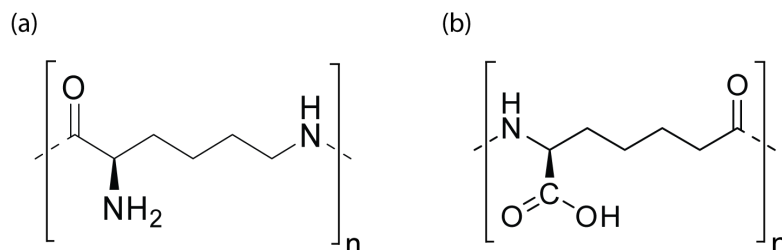


Figure 7.5: Chemical structure of (a) PLL and (b) PGA.

Whilst the substrate itself is inert since will not adsorb any protons due to its positive charge in the pH range studied, the glass of the UME will adsorb some of the protons produced at the Pt tip. To account for this, an adsorption boundary condition was applied, and a number of simulations were run for different $\text{p}K_a$ values, setting the concentration of adsorption sites as $N = 1 \times 10^{-9} \text{ mol cm}^{-2}$. As can be seen visually in Figure 7.6, adding this boundary condition greatly affects the resulting pH profile, and the results for different $\text{p}K_a$ values clearly show that this parameter has a large influence on the extent of proton adsorption (Figure 7.7).

Comparing the experimental and simulated data, however, shows a significant discrepancy between the two (Figure 7.7). Whilst the gradient of the experimental data appears to match the simulation after around 1 s, initially there is a considerable difference. For the simulated data, there is a very fast rise in the diffusion profile of the protons around the UME after the initiation of galvanostatic proton generation, which is not present in the experimental data. After this initial period ($\sim 30 \text{ ms}$), the adsorption of protons onto the glass

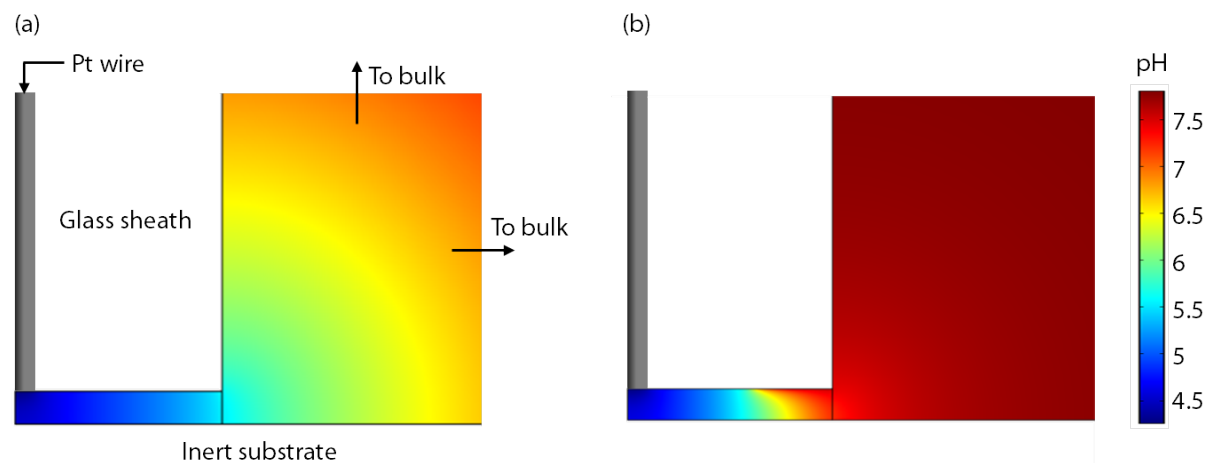


Figure 7.6: Simulated pH profiles 3 s after initiation of a 1.5 nA anodic current for an inert substrate with (a) no proton adsorption at the UME glass surface and (b) an adsorption boundary condition applied ($pK_a = 8.3$, $N = 1 \times 10^{-9} \text{ mol cm}^{-2}$).

surface starts to influence the shape of the profile, controlling its gradient.

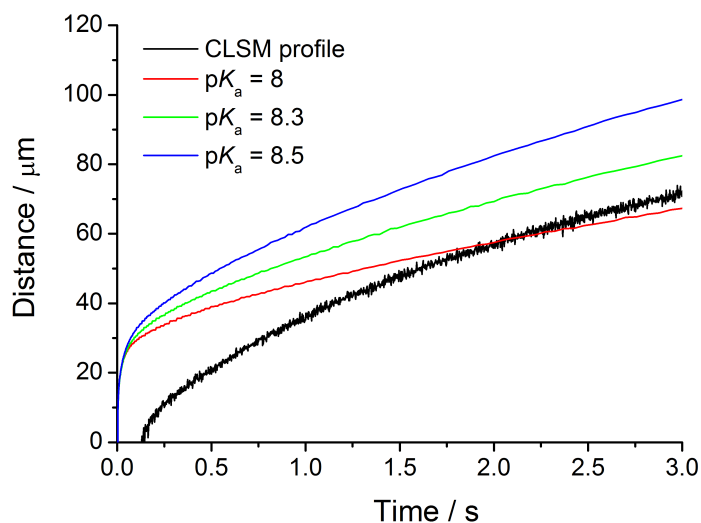


Figure 7.7: Experimental and simulated spatio-temporal plots of the radial position of the half-maximum fluorescence intensity for different effective pK_a values on the UME glass surface ($N = 1 \times 10^{-9} \text{ mol cm}^{-2}$).

Figure 7.8 shows the pH profile 5 ms after initiation of the anodic current, in which it can clearly be seen that the pH has already reached 6.1, 10 μm above the substrate. However, in the experimental profile, this pH value is not reached until ~ 0.2 s, indicating that solution processes involving the uptake of protons are occurring. Previous SECM studies have taken advantage of this “chemical lens” created by scavenger molecules, which uptake species generated at the UME, to increase the resolution of the instrument,²⁷ however, here the unknown nature of the solution processes convolutes the analysis.

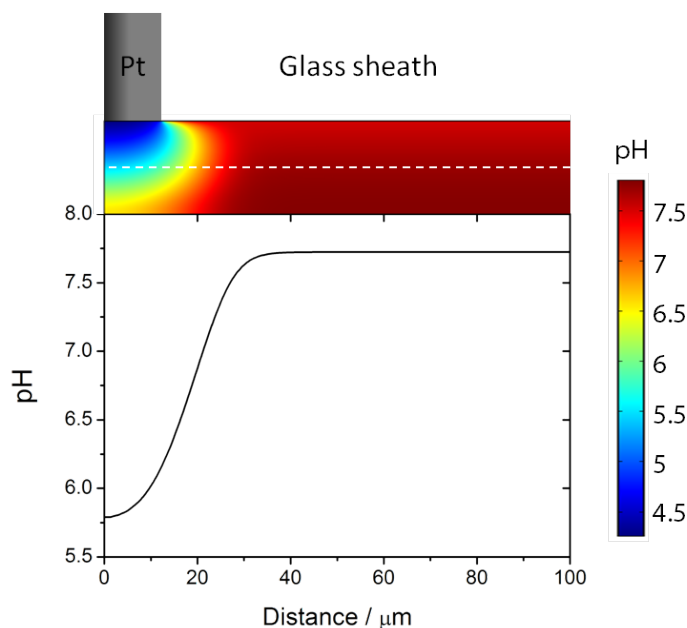


Figure 7.8: Simulated pH profile 5 ms after the initiation of the 1.5 nA anodic current (pK_a 8.3 on UME glass, $N = 1 \times 10^{-9}$ mol cm $^{-2}$).

To overcome this initial inconsistency, the distance corresponding to the time at which surface adsorption starts to dominate the shape of the simulated profiles was found, and the time axis offset to match the experimental data. During this initial time period, solution processes such as the uptake of protons by dissolved CO₂

will reduce the flux of protons to the substrate, causing a discrepancy between the experimental and simulated data. After the initial period of equilibration between the flux of protons from the UME and uptake in solution, the solution processes will have less of an influence on the pH profile, and proton-substrate interactions will begin to dominate the response. Offsetting the experimental data to account for this process results in good agreement between experiment and simulation with an effective pK_a value of 8.3 at the UME glass boundary, at a range of different applied currents, from 0.5 to 2 nA, as can be seen in Figure 7.9.

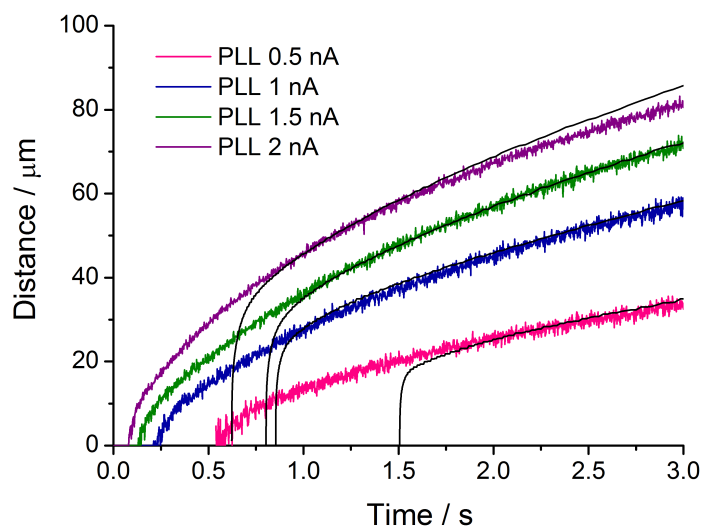


Figure 7.9: Experimental and simulated spatio-temporal plots for PLL-modified substrates at a range of different applied anodic currents (pK_a 8.3 on UME glass, $N = 1 \times 10^{-9}$ mol cm $^{-2}$).

This simple approach to overcome the unaccounted complexities of the experimental system is useful in demonstrating how FEM simulations can be used to determine intrinsic parameters, however, there may be additional factors influencing the process, for example if the applied current does not generate the flux of proton expected, which will affect the results. Therefore, whilst this

model is useful for providing estimates for the effective surface pK_a values and lateral diffusion coefficients, reliable conclusions about the quantitative values of these parameters cannot be drawn at this point.

7.4.2 CASE 2: POLY-L-GLUTAMIC ACID

Poly-L-glutamic acid (PGA) is a polymeric amino acid, commonly used for a wide variety of biological applications.²⁸⁻³⁰ Each glutamic acid subunit has an intrinsic pK_a value of 4.1, and should therefore be fully deprotonated at pH 7.8, acting as a sink for proton adsorption. However, the effective pK_a value may be different due to polymer-surface interactions. In order to determine this effective pK_a value, the substrate is no longer considered inert, and a second adsorption/desorption boundary condition is applied to this surface. The surface density of PGA is fixed at 5×10^{-10} mol cm⁻²,³¹ corresponding to the number of sites available for proton adsorption, and the pK_a of the surface is varied. This will affect the adsorption and desorption kinetics and giving rise to different pH profiles. As can be seen in Figure 7.10, an effective pK_a value of 7.3 fits the experimental data well for all applied currents, indicating that protons are not adsorbing to the surface as rapidly as expected based on the intrinsic pK_a value.

7.4.3 CASE 3: PHOSPHATIDYLCHOLINE BILAYER

Bilayers composed of egg phosphatidylcholine (PC) were formed on glass coverslips by incubating in a solution containing egg PC SUVs for 128 minutes. After this time, a stable, uniform supported lipid bilayer was formed. As for the

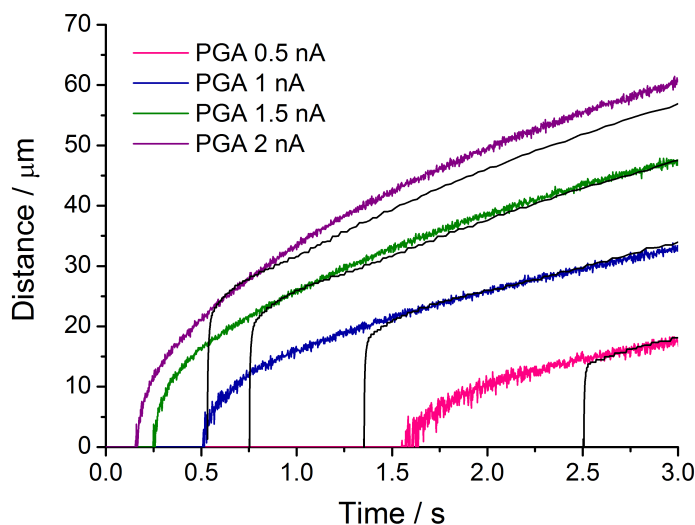


Figure 7.10: Experimental and simulated spatio-temporal plots for PGA-modified substrates at a range of different applied anodic currents with substrate $pK_a = 7.3$ and $N = 5 \times 10^{-10} \text{ mol cm}^{-2}$.

other substrates, protons were galvanostatically generated from the UME, and the resulting fluorescence profiles were analysed to produce spatio-temporal plots of the half-maximum fluorescence. For the bilayer case, a lateral diffusion term must now be included in the simulation boundary condition on this surface. Additionally, the adsorption/desorption term is modified to more accurately represent the proton-bilayer interaction. Since there is no buffer in the aqueous phase (to allow changes in pH to be measured) there will be a strong potential barrier at the surface, preventing protons from desorbing from the bilayer. Previous studies have also shown that the pK_a of the substrate has no impact on the rate of adsorption and lateral diffusion of protons, since this is assumed to occur predominantly in the water layer adjacent to the bilayer.²⁰ To reflect these conditions, the desorption term is removed and adsorption is modelled as $k_a(1 - \theta)c$, where k_a is set at a fast rate of 1 cm s^{-1} . With this modified

boundary condition and setting the number of concentration of surface sites as $2.5 \times 10^{-10} \text{ mol cm}^{-2}$,³² corresponding to the lipid surface coverage, the lateral diffusion coefficient, D_{surf} , can be varied to match simulated and experimental profiles.

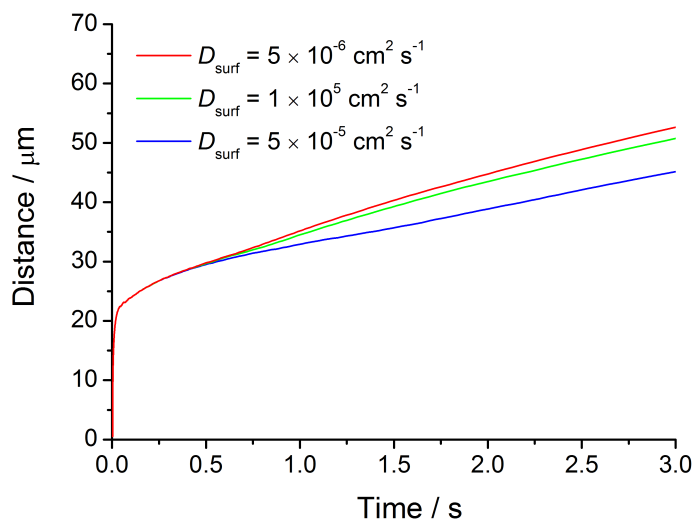


Figure 7.11: Simulated spatio-temporal plots for supported egg PC bilayers with a range of lateral diffusion coefficients (D_{surf}). The number of adsorption sites was set as $N = 2.5 \times 10^{-10} \text{ mol cm}^{-2}$ with the adsorption rate $k_a = 1 \text{ cm s}^{-1}$.

Figure 7.11 clearly shows the effect of increasing the lateral diffusion coefficient on the simulated profiles, since as protons adsorb onto the surface, they diffuse along the membrane surface allowing more protons to adsorb. Once again, by shifting the time axis of the simulated data, a good fit with the experimental data can be achieved for a diffusion coefficient value of $5 \times 10^{-5} \text{ cm}^2 \text{ s}^{-1}$ at the three different currents used (Figure 7.12).

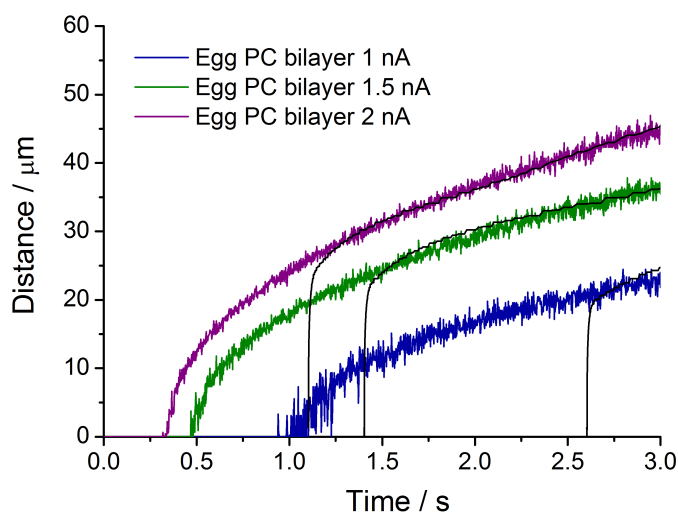


Figure 7.12: Experimental and simulated spatio-temporal plots for supported egg PC bilayers at a range of different applied anodic currents ($D_{\text{surf}} = 5 \times 10^{-5} \text{ cm}^2 \text{ s}^{-1}$, $N = 2.5 \times 10^{-10} \text{ mol cm}^{-2}$ and $k_a = 1 \text{ cm s}^{-1}$).

7.5 OPTIMISATION OF EXPERIMENTAL SETUP AND SIMULATION METHODS

Whilst good agreement between experiment and simulation can be achieved by applying a time offset, it would be more beneficial to determine methods of reducing the inconsistency. Figure 7.13 shows the time offset applied for each substrate at each anodic current. There is a clear trend between the applied current and the offset implemented, indicating that this issue can be overcome to a certain extent with the application of higher currents.

Interestingly, there is also an effect of the substrate on the time offset, which is not observed in the simulations. Figure 7.14 shows the simulated profiles for each of the different substrates studied using the parameters of best fit, demonstrating

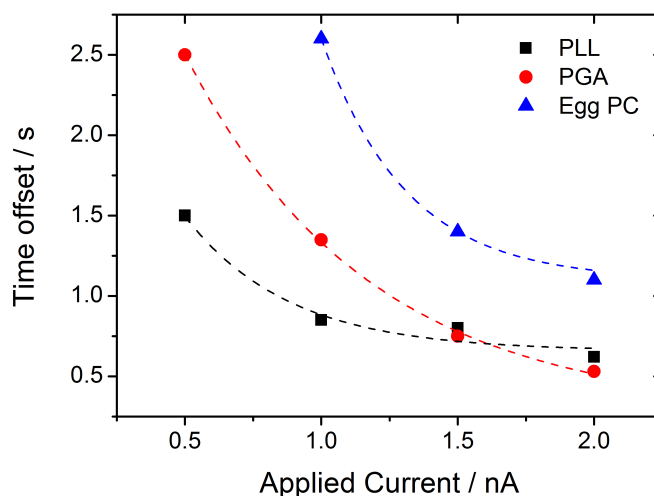


Figure 7.13: Plot of the time offset applied to the simulated data for each anodic current applied and substrate investigated.

that the surface only affects the proton distribution once the initial flux of protons from the UME has been established. This substrate-dependent effect could be due to the presence of functional groups in solution, which have detached from the surface and act as another proton carrier. For the egg PC bilayer case, it is possible that applying an anodic current disrupts the bilayer, due to the electric field generated. Further experiments were also carried out with bilayers containing egg PC with 20% DSPG which is negatively charged. This charged bilayer appears to have a greater impact on proton generation than the neutral case, indicating that this may be due to disruption of the membrane by the electric field, which would affect the charged bilayer to a greater extent than the neutral bilayer.

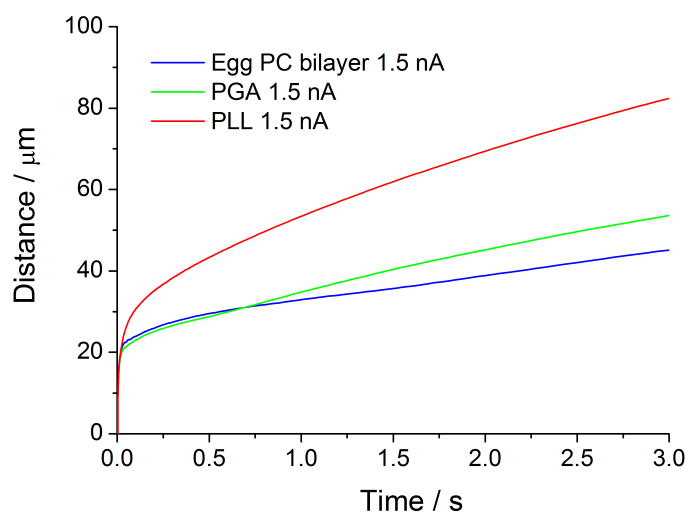


Figure 7.14: Simulated spatio-temporal plots for each substrate studied with an applied anodic current of 1.5 nA. For all cases, the UME glass pK_a was 8.3, with $N = 1 \times 10^{-9} \text{ mol cm}^{-2}$. For the PGA substrate, $pK_a = 7.3$ with $N = 5 \times 10^{-10} \text{ mol cm}^{-2}$, and for the egg PC bilayer, $D_{\text{surf}} = 5 \times 10^{-5} \text{ cm}^2 \text{ s}^{-1}$ with $N = 2.5 \times 10^{-10} \text{ mol cm}^{-2}$ and the adsorption constant, $k_a = 1 \text{ cm s}^{-1}$.

7.6 CONCLUSIONS

This chapter has demonstrated how FEM simulations can be used to understand the interaction of protons with different substrates. Protons were generated via the application of an anodic current to a UME and the resulting pH distribution was monitored with CLSM to produce spatio-temporal plots of the resulting profiles. Although there were significant discrepancies between the initial region of the experimental and simulated profiles, shifting the time axis of the simulated profile to eliminate this region from the analysis produced a good fit, which was consistent for the different applied currents. The inert, PLL surface required an adsorption boundary condition on the UME glass sheath to account for the

observed fluorescence profile, whilst the negatively charge PGA surface did not adsorb protons to the extent expected from its low intrinsic pK_a value. The egg PC bilayer exhibited a high lateral diffusion coefficient, which gave consistent agreement between experiment and simulation for all applied currents. However, this case displayed the greatest inconsistency between the experimental and simulated profiles, indicating that proton generation at the UME is affected by the presence of the bilayer.

Whilst the data presented herein cannot be used to draw reliable quantitative conclusions about the systems studied, the simulations highlight issues with the experimental setup, which could be overcome simply to obtain more reliable data. Increasing the anodic current would minimise discrepancies between experimental and simulated data, and by carrying out the experiment in an inert atmosphere, the influence of dissolved CO_2 in the system could be eliminated. Alternatively, additional solution processes could be introduced into the model to more accurately reflect the experimental conditions. Overall, carrying out simulations in conjunction with experiments, provides an opportunity for both the experimental setup and model to be optimised to give the most consistent and reliable data, in a way that would not be possible with either approach in isolation.

7.7 REFERENCES

- [1] Gennis, R. B. *Biomembranes: Molecular Structure and Function*; Springer-Verlag, New York, 1989.
- [2] Scherrer, P. *Nature* **1995**, *374*, 222–222.
- [3] Prats, M.; Teissie, J.; Tocanne, J.-F. *Nature* **1986**, *322*, 756–758.
- [4] Heberle, J.; Riesle, J.; Thiedemann, G.; Oesterhelt, D.; Dencher, N. A. *Nature* **1994**, *370*, 379–382.
- [5] Mitchell, P. *Nature* **1961**, *191*, 144–148.
- [6] Antonenko, Y. N.; Kovbasnjuk, O. N.; Yaguzhinsky, L. S. *Biochimica et Biophysica Acta (BBA) - Biomembranes* **1993**, *1150*, 45–50.
- [7] Gutman, M.; Nachliel, E.; Gershon, E. *Biochemistry* **1985**, *24*, 2937–2941.
- [8] Serowy, S.; Saparov, S. M.; Antonenko, Y. N.; Kozlovsky, W.; Hagen, V.; Pohl, P. *Biophysical Journal* **2003**, *84*, 1031–1037.
- [9] Teissié, J.; Prats, M.; Soucaille, P.; Tocanne, J. F. *Proceedings of the National Academy of Sciences* **1985**, *82*, 3217–3221.
- [10] Antonenko, Y.; Pohl, P. *European Biophysics Journal* **2008**, *37*, 865–870.
- [11] Marantz, Y.; Nachliel, E.; Aagaard, A.; Brzezinski, P.; Gutman, M. *Proceedings of the National Academy of Sciences* **1998**, *95*, 8590–8595.
- [12] Alexiev, U.; Mollaaghababa, R.; Scherrer, P.; Khorana, H. G.; Heyn, M. P. *Proceedings of the National Academy of Sciences* **1995**, *92*, 372–376.
- [13] Slevin, C. J.; Unwin, P. R. *Journal of the American Chemical Society* **2000**, *122*, 2597–2602.
- [14] Morgan, H.; Taylor, D.; Jr., O. O. *Chemical Physics Letters* **1988**, *150*, 311–

314.

- [15] Agmon, N. *Chemical Physics Letters* **1995**, *244*, 456–462.
- [16] Medvedev, E. S.; Stuchebrukhov, A. A. *Journal of Physics: Condensed Matter* **2011**, *23*, 234103.
- [17] Cherepanov, D. A.; Feniouk, B. A.; Junge, W.; Mulkidjanian, A. Y. *Biophysical Journal* **2003**, *85*, 1307–1316.
- [18] Cherepanov, D. A.; Junge, W.; Mulkidjanian, A. Y. *Biophysical Journal* **2004**, *86*, 665–680.
- [19] Junge, W.; McLaughlin, S. *Biochimica et Biophysica Acta (BBA) - Bioenergetics* **1987**, *890*, 1–5.
- [20] Springer, A.; Hagen, V.; Cherepanov, D. A.; Antonenko, Y. N.; Pohl, P. *Proceedings of the National Academy of Sciences* **2011**, *108*, 14461–14466.
- [21] Medvedev, E.; Stuchebrukhov, A. *Journal of Mathematical Biology* **2006**, *52*, 209–234.
- [22] Agmon, N. *Chemical Physics* **2010**, *370*, 232–237.
- [23] Wightman, R. M.; Wipf, D. O. In *Electroanalytical Chemistry*; Bard, A. J., Ed.; Marcel Dekker, 1989.
- [24] Davies, C. *Ion Association*; Butterworths, 1962.
- [25] Macpherson, J. V.; Unwin, P. R. *Analytical Chemistry* **1997**, *69*, 2063–2069.
- [26] Unwin, P. R.; Bard, A. J. *The Journal of Physical Chemistry* **1992**, *96*, 5035–5045.
- [27] Borgwarth, K.; Heinze, J. *Journal of The Electrochemical Society* **1999**, *146*, 3285–3289.
- [28] Li, C. *Advanced Drug Delivery Reviews* **2002**, *54*, 695–713.
- [29] Sun, D.; Hu, W.; Ma, W. *Journal of Analytical Chemistry* **2011**, *66*, 310–316.

- [30] Yan, S.; Rao, S.; Zhu, J.; Wang, Z.; Zhang, Y.; Duan, Y.; Chen, X.; Yin, J. *International Journal of Pharmaceutics* **2012**, *427*, 443–451.
- [31] O’Connell, M. A.; de Cuendias, A.; Gayet, F.; Shirley, I. M.; Mackenzie, S. R.; Haddleton, D. M.; Unwin, P. R. *Langmuir* **2012**, *28*, 6902–6910.
- [32] Huang, C.; Mason, J. T. *Proceedings of the National Academy of Sciences* **1978**, *75*, 308–310.

CHAPTER 8

CONCLUSIONS

The aim of this thesis was to further the understanding of two broad classes of biophysicochemical processes, namely (i) the detection of biomolecules and (ii) the transport of molecules at biomembrane interfaces. As discussed in Chapter 1, electrochemistry represents a powerful tool for the detection of biomolecules. In particular, carbon electrodes demonstrate a range of exceptional properties for this task. In Chapter 3, three different forms of carbon electrode were investigated as voltammetric sensors for the neurotransmitter, serotonin. Carbon nanotubes (CNTs) and polycrystalline boron doped diamond (pBDD) are two novel forms of carbon electrode which have gained increasing interest in recent years, and in this chapter, the properties of these materials were compared to the more conventional glassy carbon electrode. From cyclic voltammetry measurements, the sensitivity of each of the electrodes to low concentrations of serotonin was assessed, revealing the enhanced limits of detection of the pBDD and CNTN electrodes compared to GC. Whilst the CNTN electrode exhibited by far the lowest limit of detection, the pBDD electrode was found to be considerably more resistant to fouling from oxidation products, particularly when appropriate potential limits for CV measurements were chosen.

The electrochemical properties of CNTs were explored further in Chapter 4, using high resolution SECCM imaging. Flow-aligned “pristine” single-walled carbon nanotubes were grown by cCVD to allow the electroactivity of isolated regions of individual SWNTs to a range of redox mediators, including serotonin, to be assessed. There has been considerable debate in the literature as to the source of the electroactivity of SWNTs, detailed in Chapter 1, with uncertainty as to whether electron transfer occurs at the nanotube sidewalls. SECCM employs a dual barrel pipet, pulled to a sharp tip, as a mobile electrochemical cell, allowing the electrochemical response of an isolated region of the SWNT to be probed, independent of the rest of the nanotube. Using this technique, high electrochemical activity was observed along the length of the SWNT with different mediators, indicating that, in fact, the sidewall is highly active. Development of a FEM model allowed the HET rate constants to be determined from the observed electrochemical currents, indicating fast kinetics for the oxidation of FcTMA^+ . The work in this chapter provides a platform for a wide range of electrochemical studies of CNTs in the future.

FEM simulations have been shown to be a powerful tool in the determination of substrate kinetics in electrochemical systems. In Chapter 5, FEM simulations were again used to investigate HET at the surface of pBDD. This heterogeneous material is composed of facets with different dopant densities which are shown to exhibit different levels of electroactivity. High resolution IC-SECM measurements were made, which enabled the electrochemical response of each facet to be resolved. Using FEM simulations, the observed electrochemical currents could be attributed to different HET rate constants, to obtain average kinetic rates for the higher and lower doped facets. Local capacitance measurements were made using an

SECCM setup and used to calculate an estimate of the local density of states of the material. Correlating these results with the kinetic rate constants indicated that the local density of states, which is dependent on the local dopant density, appears to have a significant influence on HET kinetics. The analysis of the local density of electronic states on heterogeneous electron transfer is rarely carried out in electrochemistry, and the combination of high resolution electrochemical imaging with other complementary techniques, again provides a platform for future studies of individual facets of electrode materials.

Moving away from electrode materials, and onto biomembranes, Chapters 6 and 7 investigated transport processes at membrane interfaces. In the study of processes occurring at the cell membrane, model membranes are often used, whose composition can be carefully controlled. However, these lipid bilayer membranes can suffer from a number of limitations, restricting their applications. In Chapter 6, a new method for the fabrication of lipid bilayers was presented, which overcomes many of these challenges. Bilayers were formed at the tip of pulled theta capillaries, allowing their geometry to be carefully controlled, and without residual solvent molecules trapped between the two monolayers. Using these bilayers, the permeation of a series of weak acids was investigated, to determine the effect of permeant structure on permeability. Through the use of CLSM and a pH-sensitive fluorophore, the permeation of each weak acid was visualised as it permeated out of the pipet, across the bilayer, creating a fluorescence profile. The FEM model used to match this experimental profile to simulations, allowed the determination of the permeation coefficient for each molecule. This analysis revealed an increase in permeability with lipophilicity, a trend generally in agreement with Overton's rule.

Finally, the lateral diffusion of protons at lipid bilayers was investigated in Chapter 7. Using a similar approach to Chapter 6, the movement of protons generated galvanostatically by a UME positioned close to the membrane, was tracked with a pH-sensitive fluorophore over time using the CLSM. The fluorescence profiles produced were analysed to plot the position of the proton front over time, and this could be compared to simulated data to determine the lateral diffusion coefficient. The interaction of protons with other surfaces was also investigated, allowing effective surface pK_a values to be extracted.

In this thesis, the fundamental activity of different electrode materials has been determined using novel, high-resolution electrochemical imaging techniques, and new methods for the investigation of biological transport have been presented. Throughout this thesis, the coupling of experimental data with finite element simulations has been shown to maximise the amount of information that can be extracted, allowing the quantitative analysis of system properties that would otherwise be only qualitative. The broad scope of this approach has been illustrated through the study of two important areas: electrochemistry and membrane transport. The common approaches described open up new avenues for the study of (bio)physicochemical processes that are of widespread interest.

APPENDIX

Attached to this thesis are the FEM models used in Chapters 4-7.

CHAPTER 4

SECCM_FcTMA.mph - this model simulates the electrochemical current for a range of different k^0 values to determine the standard rate constant corresponding to the observed substrate current for the oxidation of FcTMA^+ at the SWNT surface.

SECCM_RuHex.mph - uses the same method as above to determine the standard rate constant for the reduction of $\text{Ru}(\text{NH}_3)_6^{3+}$ at the SWNT.

CHAPTER 5

ICSECM_FcTMA.mph - this model simulates the observed tip current at a UME in substrate generation tip collection mode for the oxidation of FcTMA^+ at the pBDD surface and subsequent reduction at the UME.

ICSECM_FcTMA.m - corresponding Matlab file allowing a range of k^0 values to be simulated to determine the standard rate constant for the observed electrochemical current.

ICSECM_RuHex - uses the same method as above to determine the standard

rate constant for the reduction of $\text{Ru}(\text{NH}_3)_6^{3+}$ at the pBDD substrate.

ICSECM_RuHex.m - corresponding Matlab file.

CHAPTER 6

Weak_acid_permeation.mph - this model simulates the pH profile as a weak acid permeates across the bilayer formed at the tip of a pipette into the bulk solution. The fluorescence intensity profile of fluorescein in the solution can be calculated for comparison with the experimental data, in order to determine the permeation coefficient of the weak acid.

CHAPTER 7

PLL.mph - this model simulates the pH profile as protons are generated galvanostatically at the UME positioned close to the PLL substrate. An adsorption boundary condition is implemented on the UME glass sheath but the substrate is considered inert.

PGA.mph - this model uses the same parameters for the PLL case with an additional proton adsorption boundary condition implemented on the substrate.

Bilayer.mph - this model uses the same parameters for the PLL case with an adsorption and lateral diffusion boundary condition implemented on the bilayer surface.